Full response to: The potential role of methanesulfonic acid (MSA) in aerosol formation and growth and the associated radiative forcings (Hodshire, et al.)

Contents

Responses to the reviews of Hodshire et al.

We thank the reviewers for their comments on our paper. To guide the review process we have copied the reviewer comments in black text. Our responses are in regular blue font. We have responded to all the referee comments, and we display our alterations to our paper and supporting information **in bold text**.

At the suggestion of reviewer 2, we have read through the text and have made minor grammatical corrections and minor corrections for clarity throughout the manuscript. These changes may be seen in the tracked-changes version of our submission.

Anonymous Referee #2

Interactive comment on "The potential role of methanesulfonic acid (MSA) in aerosol formation and growth and the associated radiative forcings" by Anna L. Hodshire et al.

The manuscript by Hodshire et al uses a global aersol model to quantify the role of MSA in the aerosol-climate system. The role of MSA has not been quantified previously, with the majority of current aerosol and climate models making the simple assumption that MSA does not contribute to aerosol loading. The study presents model sensitivity simulations exploring a range of mechanisms that might allow MSA to contribute to aerosol. In doing so, the authors highlight the sparcity of actual observations and lab measurements of MSA, which could be used to constrain the model simulations. When allowing MSA to condense and nucleate in the model, only modest global radiative effects (up to -40 mWm-2) are demonstrated. Regionally (e.g. in the Southern Ocean), larger differences in radiative effects are shown. The study is subject to large uncertainties arising from the lack of measurements, as well as caveats introduced by the modelling approach. These uncertainties notwithstanding, the manuscript is a valid contribution to the field and should lead to further insights about the role of MSA.

Major comments

Please explain the rationale supporting the use multiple anthropogenic NH3 emissions inventories across different regions. It's not clear why this was done and what impact this may have on the NH3 concentrations and subsequently the MSA sensitivity tests.

We realized that this section is misleading as it is currently written. We have updated the text regarding inventories in general (below). We use ammonia overwrites as we expect these national and/or regional inventories to be more accurate than the older GEIA inventory.

"Anthropogenic emissions except for ammonia, black carbon, and organic aerosol are from the Emissions Database for Global Atmospheric Research (EDGAR; Janssens-Maenhout et al., 2010). In Europe, Canada, the U.S., and Asia, anthropogenic emissions are overwritten by the European Monitoring and Evaluation Programme (Centre on Emissions Inventories and Projections, 2013), the Criteria Air Contaminant Inventory (http://www.ec.gc.ca/air/default.asp? lang=En&n=7C43740B-1), the National Emission Inventory from the U.S. EPA ((http://www.epa.gov/ttnchie1/net/2011inventory.html), and the MIX (Li et al., 2017) inventories, respectively. Black and organic carbon emissions from fossil-fuel and biofuel combustion processes are from Bond et al. (2007). Grid-box gas-phase concentrations of NH_3 are used in determining the volatility regime of MSA in the MSA parameterization (Sect. 2.2): global anthropogenic, biofuel, and natural ammonia

sources are from the Global Emissions InitiAtive (GEIA) (Bouwman et al., 1997). Anthropogenic ammonia emissions are overwritten over Europe, Canada, the U.S., and Asia using the same regional inventories discussed above for these regions. Ammonia emission from biomass burning are from FINNv1 (above).”

The comparison method described in Section 2.5 assumes that the total sulphate will be additive between scenarios (i.e. substracting DEFAULT_NoMSA from the sensitivity simulations leaves the MSA-related contribution). This is an imperfect approach as the additional mass from MSA will grow the aerosol size distribution, and therefore increase rates of dry deposition and nucleation scavenging. This limitation should be noted in the method description. I think the comparison remains useful, however.

We agree with the reviewer that this is an important caveat to point out and have added the following to sect 2.5:

“We compare our sensitivity simulations to the ATom data as follows: we subtract the DEFAULT_NoMSA sulfate mass (that accounts for sulfate and sulfuric acid from DMS/SO_2 oxidation but not MSA) for the months of August (ATom-1) and February (ATom-2) from the sulfate mass for the months of August and February for each sensitivity case that includes MSA for each grid box. The resultant differences in sulfate mass represents the model-predicted contributions of MSA to the total sulfur budget for each case. **This is an imperfect approach, as the additional aerosol mass from the contribution of MSA will change the size distribution, therefore changing rates of wet and dry deposition, and is a limitation of this study.”**

For consistency with the ATom measurements, was the model data used in the comparison also restricted to the sub-micron size range?

This is a reasonable point. We did not use the sub-micron range only; however, an off-line comparison shows that the percent difference between using the entire range (up to 10 μm) and the submicron range is well under 1%. We add the following to the text:

“We then compare the measured and predicted MSA mass by first averaging every ATom data point that falls within a given GC-TOMAS grid box. We then compare each averaged data point to that model grid box. The ATom data used in our analysis lies within 150-180° W (the Pacific ocean basin) and 10-40° W (the Atlantic ocean basin), and thus we use zonal averages of these longitude bands for both the ATom data and the GC-TOMAS output. We note that comparing monthly mean simulated values from 2014 to airborne measurements from a single point in time in 2016 and 2017 contributes to the apparent simulation errors. **We also note that we use the**

full size range (3 nm -10 µm) of sulfate from the model output whereas the ATom data is submicron. However, the model-predicted percent difference in MSA mass between the full range and the submicron mass is well under 1% (not shown)."

Page 11 line 18 refers to 'Table 4', which has not been provided. The data does appear in Figure 8.

Thank you for catching this--table 4 had been removed as it was redundant with the data in Figure 8. We have updated the text and made sure that no other references to Table 4 still exist.

Page 12 line 30 refers to Figure S7, but I think should refer to Figure S6. Please further check labelling of N10 / N80, and for left / right labelling in caption of Figure S6

Thank you for catching these errors, as well. The reference to Fig. S7 has been updated to Fig. S6. The label for Figure S6 has been updated to N80.

Minor comments

There are typographic errors through the manuscript that a thorough read-through should reveal, including some sentences that have redundant words, or fragments from C2 ACPD Interactive comment Printer-friendly version Discussion paper previous iterations. I haven't attempted to highlight them.

We have read throughout the text and corrected what typographical errors we have found.

Page 2 line 29: 'from marine particles' should be 'of marine particles'? Or 'from marine emissions'?

It should be 'of marine particles'--we have updated the text.

Page 3 line 1: VOCs – acronym not defined

Thank you--we have provided the full name along with the acronym.

Page 3 line 5/6: 'are an important source of marine emissions' should be 'are an important contributor to marine aerosol' (or something similar)? 'Aerosol' and 'particles' is being used in the same sense as 'emissions', which is incorrect.
We have updated the text:

"Sulfur-containing organic compounds in the form of dimethylsulfide (DMS; CH_3SCH_3) and organosulfates (Bates et al., 1992, Quinn et al., 2015) are important precursors and contributors to marine aerosol."

Page 3 line 13: please state the relative yields of each product of DMS oxidation

The relative yields of each product from DMS oxidation are uncertain. We do state in the methods that for this study, we assume that we follow the findings of Chin et al. (1996) and use a branching ratio of 75:25 for SO_2:MSA. However, this is a source of uncertainty. For instance, Chang et al. (2011) states: "The sensitivity of model results to uncertainties in DMS chemistry was also untested. In the oxidation of DMS by OH addition, the branching ratio between SO2 and methane sulfonic acid (MSA) is uncertain and, following Chin et al.[1996], we used a value of 75:25. Laboratory studies report percent yields of SO2:MSA of 65:4 [Yin et al.,1990a], 27:6 [Sørensen et al., 1996] and 38:11 [Arsene et al.,2001], for example."
We add the following to the introduction:

"The main products of DMS from oxidation by the hydroxyl radical are sulfur dioxide (SO_2) and methanesulfonic acid ($CH_3S(O)_2OH$, MSA) (Andreae et al., 1985). SO_2 can further oxidize to create sulfuric acid (H_2SO_4). **The relative yields of SO_2 and MSA from DMS oxidation are still uncertain, with reported branching ratios from oxidation of DMS by OH addition of SO_2:MSA varying across 75:25, 65:4, 27:6, and 38:11 (Yin et al., 1990; Chin et al., 1996; Sørensen et al., 1996; Arsene et al., 2001).**"

We also add text in the methods:

"In the standard GEOS-Chem DMS mechanism, DMS reacts with OH through the OH addition pathway to form molar yields of 0.75 SO_2 and 0.25 MSA (Chatfield and Crutzen, 1990; Chin et al., 1996). **As discussed in the introduction, laboratory studies have reported variable yields of SO_2 and MSA from DMS oxidation by OH addition. We do not test the sensitivity of our simulations to other pathways, and this is a source of uncertainty.**"

Arsene, C., Barnes, I., Becker, K. H. and Mocanu, R.: FT-IR product study on the photo-oxidation of dimethyl sulphide in the presence of NOx—Temperature dependence, Atmos. Environ., 35(22), 3769–3780, doi:10.1016/S1352-2310(01)00168-6, 2001.

Chang, R. Y.-W., Sjostedt, S. J. , Pierce, J. R., Papakyriakou, T. N., Scarratt, M. G., Michaud, S., Levasseur, M., Leaitch, W. R., and Abbatt, J. P. D.: Relating atmospheric and oceanic DMS levels to particle nucleation events in the Canadian Arctic, J. Geophys. Res., 116, D00S03, doi:10.1029/2011JD015926, 2011.

Chin, M., Jacob, D. J., Gardner, G. M., Foreman-fowler, M. S., Spiro, P. A. and Savoie, D. L.: A global three-dimensional model of tropospheric sulfate acid, , 101, doi:10.1029/ 96JD01221, 1996.

Sørensen, S., Falbe-Hansen, H., Mangoni, M., Hjorth, J., and. Jensen, N. R: Observation of DMSO and CH3S(O)OH from the gas phase reaction between DMS and OH, J. Atmos. Chem., 24(3), 299–315, doi:10.1007/BF00210288, 1996.

Yin, F., D. Grosjean, R. C. Flagan, and J. H. Seinfeld: Photooxidation of dimethyl sulfide and dimethyl disulfide. II: Mechanism evaluation, J. Atmos. Chem., 11(4), 365–399, doi:10.1007/BF00053781, 1990.

Page 5 line 24: not clear what 'Regional EDGAR overwrites' are

We have updated this section in response to an early comment and refer the reviewer to that response.

Page 6 line 25: for completeness, please clarify whether MSA is assumed to be involved in the binary nucleation process

Thank you, we have added this clarification.

When MSA is assumed to participate in nucleation, it is treated as an extra source of sulfuric acid for the ternary and binary nucleation schemes within the model.

Anonymous referee #3

This manuscript presents a sensitivity study estimating the potential influence of MSA, produced from oceanic DMS emission, on the submicron aerosol population and further on aerosol radiative effects in the global atmosphere. The paper relies on a set of global model simulations that cover the plausible range of parameters anticipated to affect how MSA contributes to the investigated issues. The used model has been evaluated previously in many other applications, so it can be considered appropriate for the purposes of this study. The paper is well organized, and the authors adequately discuss associated uncertainties. The conducted study itself is original and important to the scientific community.

I have a few, rather minor, issues to be considered before accepting this paper for publication.

The last sentence of page 2 (lines 28-31) is strange. Please modify.

We agree and have rewritten this statement as follows:

To improve model estimates of the DRE and AIE, models must account for nucleation and condensational growth of marine particles.

Strictly speaking, primary biological or organic particles should not be called "organic compounds".

We have updated the text:

Biologically productive oceans emit volatile organic compounds (VOCs), primary biological particles, primary organic particles, and halocarbons (Quinn et al., 2015).

Are the latest estimates on the contribution of DMS to biogenic sulfur budget and sulfur precursor emission really as far back in time as from years 1990 and 2006. I also wonder the relative accuracy of the given numbers, i.e. 50% versus 21% (page 3).

We appreciate the reviewer pointing out the outdatedness of these statistics. We have found more appropriate figures and have updated the text and references as follows:

DMS accounts for approximately one-fifth of the global sulfur budget (Fiddes et al., 2017), with DMS flux estimates range from 9 to 35 Tg yr^{-1} of sulfur (Belviso et al., 2004; Elliott, 2009; Woodhouse et al., 2010; Tesdal et al., 2016), although global DMS fluxes remain uncertain (Tesdal et al., 2016; Royer et al., 2015).

Belviso, S., Bopp, L., Moulin, C., Orr, J. C., Anderson, T. R., Aumont, O., Chu, S., Elliott, S., Maltrud, M. E., and Simó, R.: Comparison of global climatological maps of sea surface dimethyl sulfide, Global Biogeochem. Cy., 18, GB3013, https://doi.org/10.1029/2003GB002193, 2004.

Elliott, S.: Dependence of DMS global sea-air flux distribution on transfer velocity and concentration field type, J. Geophys. Res.- Biogeo., 114, 1–18, https://doi.org/10.1029/2008JG000710, 2009.

Royer, S. J., Mahajan, A. S., Galí, M., Saltzman, E., and Simõ, R.: Small-scale variability patterns of DMS and phytoplankton in surface waters of the tropical and subtropical Atlantic, Indian, and Pacific Oceans, Geophys. Res. Lett., 42, 475–483, https://doi.org/10.1002/2014GL062543, 2015.

Sheng, J. X., Weisenstein, D. K., Luo, B. P., Rozanov, E., Stenke, A., Anet, J., Bingemer, H., and Peter, T.: Global atmospheric sulfur budget under volcanically quiescent conditions: Aerosol-chemistry-climate model predictions and validation, J. Geophys. Res.-Atmos., 120, 256–276, https://doi.org/10.1002/2014JD021985, 2015.

Tesdal, J. E., Christian, J. R., Monahan, A. H., and Von Salzen, K.: Evaluation of diverse approaches for estimating sea-surface DMS concentration and air-sea exchange at global scale, Environ. Chem., 13, 390–412, https://doi.org/10.1071/EN14255, 2016.

Woodhouse, M. T., Carslaw, K. S., Mann, G. W., Vallina, S. M., Vogt, M., Halloran, P. R., and Boucher, O.: Low sensitivity of cloud condensation nuclei to changes in the sea-air flux of dimethyl-sulphide, Atmos. Chem. Phys., 10, 7545–7559, https://doi.org/10.5194/acp-10-7545-2010, 2010.

The authors use rather old binary and ternary nucleation schemes in their simulations, together with a fixed tuning factor that may or may not be valid in marine environments that are more interesting than continental regions in this study. The authors investigated the sensitivity of their results on different assumptions on whether MSA participates on nucleation or not, but do not discuss whether these results are sensitive to apparent uncertainties in the nucleation scheme itself. I would like the authors to address this point at least by discussing it shortly.

We have added the following discussion to Sect. 2.6 (Study Caveats):

We do not test the sensitivity of our simulations to the binary and ternary nucleation schemes used in this study, including potential sensitivity to the global tuning factor of 10^{-5} that was developed for continental regions (Jung et al., 2010; Westervelt et al., 2013). This source of uncertainty should be tested in future studies, as well.

The authors should discuss more explicitly what part of aerosol-cloud interactions they are attempting to capture in their simulations. Is it the first indirect effect only or something else as well?

We apologize for the lack of clarity here: the aerosol-cloud interactions should be the cloud-albedo AIE, not just the AIE. We have amended the text to read ‘cloud-albedo AIE’ throughout, and have informed the reader that figure labels of ‘AIE’ refer to the cloud-albedo AIE, as well.

The potential role of methanesulfonic acid (MSA) in aerosol formation and growth and the associated radiative forcings

Anna L. Hodshire[1], Pedro Campuzano-Jost[2,3], John K. Kodros[1], Betty Croft[4], Benjamin A. Nault[2,3], Jason C. Schroder[2,3], Jose L. Jimenez[2,3], Jeffrey R. Pierce[1]

[1]Department of Atmospheric Science, Colorado State University, Fort Collins, CO 80523, USA
[2]Department of Chemistry, University of Colorado, Boulder, CO, USA
[3]Cooperative Institute for Research in Environmental Sciences, University of Colorado, Boulder, CO, USA
[4]Dalhousie University, Department of Physics and Atmospheric Science, Halifax, NS, B3H 4R2, Canada

Correspondence to: Anna L. Hodshire (Anna.Hodshire@colostate.edu)

Abstract. Atmospheric marine aerosol particles impact Earth's albedo and climate. These particles can be primary or secondary and come from a variety of sources, including sea salt, dissolved organic matter, volatile organic compounds, and sulfur-containing compounds. Dimethylsulfide (DMS) marine emissions contribute greatly to the global biogenic sulfur budget, and its oxidation products can contribute to aerosol mass, specifically as sulfuric acid and methanesulfonic acid (MSA). Further, sulfuric acid is a known nucleating compound, and MSA may be able to participate in nucleation when bases are available. As DMS emissions, and thus MSA and sulfuric acid from DMS oxidation, may have changed since pre-industrial times and may change in a warming climate, it is important to characterize and constrain the climate impacts of both species. Currently, global models that simulate aerosol size distributions include contributions of sulfate and sulfuric acid from DMS oxidation, but to our knowledge, global models typically neglect the impact of MSA on size distributions.

In this study, we use the GEOS-Chem-TOMAS (GC-TOMAS) global aerosol microphysics model to determine the impact on aerosol size distributions and subsequent aerosol radiative effects from including MSA in the size-resolved portion of the model. The effective equilibrium vapor pressure of MSA is currently uncertain, and we use the Extended Aerosol Inorganics Model (E-AIM) to build a parameterization for GC-TOMAS of MSA's effective volatility as a function of temperature, relative humidity, and available gas-phase bases, allowing MSA to condense as an ideally nonvolatile or semivolatile species or too volatile to condense. We also present two limiting cases for MSA's volatility, assuming that MSA is always ideally nonvolatile (irreversible condensation) or that MSA is always ideally semivolatile (quasi-equilibrium condensation but still irreversible condensation). We further present simulations in which MSA participates in binary and ternary nucleation with the same efficacy as sulfuric acid whenever MSA is treated as ideally nonvolatile. When using the volatility parameterization described above (both with and without nucleation), including MSA in the model changes the global annual averages at 900 hPa of submicron aerosol mass by 1.2%, N3 (number concentration of particles greater than 3 nm in diameter) by -3.9% (non-nucleating) or 112.5% (nucleating), N80 by 0.8% (non-nucleating) or 2.1% (nucleating), the cloud-albedo aerosol indirect effect (AIE) by -8.6 mW m^{-2} (non-nucleating) or -26 mW m^{-2} (nucleating), and the direct radiative effect (DRE) by -15 mW m^{-2} (non-nucleating) or -14 mW m^{-2} (nucleating). The sulfate and sulfuric acid from DMS oxidation produces 4-6 times more submicron mass than MSA does, leading to ~10 times a stronger cooling effect in the

DRE. But the changes in N80 are comparable between the contributions from MSA and from DMS-derived sulfate/sulfuric acid, leading to comparable changes in the cloud-albedo AIE.

Model-measurement comparisons with the Heintzenberg et al. (2000) dataset over the Southern Ocean indicate that the default model has a missing source or sources of ultrafine particles: the cases in which MSA participates in nucleation (thus increasing ultrafine number) most closely match the Heintzenberg distributions, but we cannot conclude nucleation from MSA is the correct reason for improvement. Model-measurement comparisons with particle-phase MSA observed with a customized Aerodyne high-resolution time-of-flight aerosol mass spectrometer (AMS) from the ATom campaign show that cases with the MSA volatility parameterizations (both with and without nucleation) tend to fit the measurements the best (as this is the first use of MSA measurements from ATom, we provide a detailed description of these measurements and their calibration). However, no one model sensitivity case shows the best model-measurement agreement for both Heintzenberg and the ATom campaigns. As there are uncertainties in both MSA's behavior (nucleation and condensation) and the DMS emissions inventory, further studies on both fronts are needed to better constrain MSA's past, current and future impacts upon the global aerosol size distribution and radiative forcing.

1 Introduction

Atmospheric marine particles contribute significantly to the global aerosol budget and impact the planetary albedo and climate (Quinn et al., 2015; Reddington et al., 2017). The number concentration, size, and chemical composition of these marine particles determine their ability to affect climate, through either absorbing and scattering incoming solar radiation (the direct radiative effect [DRE]; Charlson et al., 1992; Erlick et al., 2001) or indirectly, by modifying cloud properties (the cloud-albedo aerosol indirect effect [AIE]; de Leeuw et al., 2011). For the DRE, the magnitude and relative division between absorbing and scattering will depend on both the particle size and composition (Bond et al., 2006; 2013); peak efficiencies for scattering and absorbing solar radiation are typically reached with particles between 100 nm to 1 µm in diameter (Seinfeld and Pandis, 2006). The cloud-albedo AIE refers to aerosols' ability to alter the reflectivity (albedo) of clouds by changing properties such as the cloud droplet number concentration (CDNC) (Twomey, 1974). Typically, particles act as cloud condensation nuclei (CCN) if they are larger than 40-100 nm; the ability of a particle to act as a CCN is also dependent upon particle hygroscopicity (Petters and Kreidenweis, 2007). The number of particles in these size ranges depend on primary emissions, as well as nucleation, condensation, and coagulation (Pierce and Adams, 2009a). To improve model estimates of the DRE and cloud-albedo AIE, models must account for nucleation and condensational growth of marine particles.

Biologically productive oceans emit volatile organic compounds (VOCs), primary biological particles, primary organic particles, and halocarbons (Quinn et al., 2015). Sources of marine particles often indicate organic species present

Jeffrey Pierce 2/13/2019 8:29 PM
Deleted: cloud properties, including

Anna Lily Hodshire 2/12/2019 10:38 PM
Deleted: from

Anna Lily Hodshire 2/12/2019 11:22 PM
Deleted: , as for a significant portion of the remote atmosphere, marine and stratospheric particles are the main sources of particles (e.g. Huang et al., 2013)

Anna Lily Hodshire 2/12/2019 11:24 PM
Deleted: organic species, compounds, and particles such as

(e.g. Heintzenberg et al., 2001; O'Dowd et al., 2007; Frossard et al., 2014, Wang et al., 2017) that could dominate submicron aerosol mass (O'Dowd et al., 2004; Facchini et al., 2008). Sulfur-containing organic compounds in the form of dimethylsulfide (DMS; CH_3SCH_3) and organosulfates (Bates et al., 1992, Quinn et al., 2015) are important precursors and contributors to marine aerosol. DMS accounts for approximately one-fifth of the global sulfur budget (Fiddes et al., 2017), with DMS flux estimates ranging from 9 to 35 Tg yr^{-1} of sulfur (Belviso et al., 2004; Elliott, 2009; Woodhouse et al., 2010; Tesdal et al., 2016), although global DMS fluxes remain uncertain (Tesdal et al., 2016; Royer et al., 2015). DMS and its oxidation products have been the focus of many studies determining the gas-phase chemistry (e.g. Barnes et al. 2006 and references therein), gas-phase kinetics (e.g. Wilson and Hirst, 1996 and references therein), and possible impact to the aerosol size distribution and radiative budget (e.g. Korhonen et al., 2008; Woodhouse et al., 2013). Much of this research has stemmed from efforts to test the hypothesis that DMS emissions may regulate climate through a temperature-emissions feedback (the CLAW hypothesis, Charlson et al. (1987)).

The main products of DMS from oxidation by the hydroxyl radical are sulfur dioxide (SO_2) and methanesulfonic acid ($CH_3S(O)_2OH$, MSA) (Andreae et al., 1985). SO_2 can further oxidize to create sulfuric acid (H_2SO_4). The relative yields of SO_2 and MSA from DMS oxidation are still uncertain, with reported branching ratios from oxidation of DMS by OH addition of SO_2:MSA varying across 75:25, 65:4, 27:6, and 38:11 (Yin et al., 1990; Chin et al., 1996; Sørensen et al., 1996; Arsene et al., 2001). The effective equilibrium vapor pressure of sulfuric acid in the presence of water in the troposphere is negligible compared to sulfuric acid concentrations under all atmospherically relevant conditions (Marti et al., 1997), allowing sulfuric acid to readily condense onto particles of all sizes and participate in particle nucleation (e.g. Kulmala et al., 2000). Gas-phase concentrations of MSA have been observed to be 10-100% of sulfuric acid concentrations in coastal marine boundary layers (Eisele and Tanner, 1993; Berresheim et al., 2002; Mauldin et al., 2003), and MSA can contribute to the growth of pre-existing marine particles, at times contributing over half as much bulk aerosol mass as non-sea salt sulfate to the total aerosol burden (e.g. Preunkert et al., 2008; Legrand et al., 2017). To our knowledge, the effective equilibrium vapor pressure of MSA, which should depend on temperature, relative humidity, and availability of bases, has not previously been well-quantified for the range of potential atmospheric conditions. Also to our knowledge, MSA has not yet been observed in the field to directly contribute to aerosol nucleation, although Dall'Osto et al. (2018) observed new particle formation events over Greenland that suggest that MSA could be involved in a portion of the events. Bork et al. (2014) determined through the Atmospheric Cluster Dynamics Code kinetic model (McGrath et al., 2012; Olenius et al., 2013) that the presence of MSA could increase the molecular cluster formation rates by as much as one order of magnitude for a MSA-H_2SO_4-DMA (DMA = dimethylamine) system under atmospherically relevant MSA concentrations. This enhancement is predicted to be typically less than 300% at 258 K and less than 15% at 298 K for the case of [DMA] = 10^9 molecules cm^{-3} (Bork et al., 2014). Chen et al. (2015) observed an MSA-H_2O-TMA (TMA = trimethylamine) system to nucleate in the laboratory, but at an efficiency lower than that of the H_2SO_4-H_2O system. Chen and Finlayson-Pitts (2017) further observed nucleation of MSA/H_2O systems with TMA, DMA, MA (MA = methylamine) and ammonia. To our knowledge, global models that simulate aerosol number concentrations (e.g. D'Andrea et al. 2013; Kodros et al., 2018; Ma and Yu, 2015;

Jeffrey Pierce 2/13/2019 8:30 PM
Deleted:

Anna Lily Hodshire 2/12/2019 10:41 PM
Deleted: an

Anna Lily Hodshire 2/12/2019 10:41 PM
Deleted: source of marine emissions

Anna Lily Hodshire 2/13/2019 4:41 PM
Formatted: Superscript

Anna Lily Hodshire 2/12/2019 11:44 PM
Deleted: emissions constitutes approximately 1950% of the global biogenic sulfur emissions budget and almost one-third of total tropospheric sulfate, as currently understood (Sheng et al, 2015)e.g. Andreae, 1990) and approximately 21% of all sulfur precursor gases (Textor et al., 2006).

Anna Lily Hodshire 2/12/2019 10:49 PM
Formatted: Subscript

Anna Lily Hodshire 2/12/2019 10:49 PM
Formatted: Subscript

Anna Lily Hodshire 2/13/2019 8:39 PM
Deleted: as yet

Anna Lily Hodshire 2/13/2019 8:39 PM
Deleted: ;

Regayre et al., 2018; Xausa et al., 2018) only track the effect of sulfuric acid and aqueous sulfate from DMS/SO_2 oxidation on the aerosol size distribution and not MSA. Thus, the potential contribution towards nucleation and/or size-resolved particle growth by MSA and the resulting radiative impacts has not yet been quantified.

The effective volatility (equilibrium vapor pressure above the particle-phase mixture) of MSA will modulate its impact on the aerosol size distribution. Condensational growth of vapors to the particle phase is controlled by both the volatility of the condensing species and the concentration of the species in the gas phase. Riipinen et al. (2011) presented two limiting cases of growth for gas-phase condensable material:

(1) Compounds with low enough saturation vapor concentrations (C*; Donahue et al., 2006) may be considered essentially nonvolatile to condense irreversibly through kinetic, gas-phase-diffusion-limited condensation (Riipinen et al. 2011; Zhang et al., 2012). This type of growth is referred to as "kinetic condensation" by Riipinen et al. (2011) and can be thought of as effectively nonvolatile condensation. The effective volatility required to achieve effectively nonvolatile condensation typically must be less than C*<≈10^{-3} μg m^{-3} (e.g. low and extremely low volatility organic compounds; LVOCs and ELVOCs) (Pierce et al., 2011; Donahue et al., 2011). The contribution to growth from effectively nonvolatile condensation is proportional to the Fuchs-corrected particle surface area (Pandis et al., 1991). We will refer to this type of condensation as "ELVOC-like" condensation in this work.

(2) In contrast, semi-volatile species (e.g. semi-volatile organic compounds; SVOCs) with average C* between 10^0-10^2 μg m^{-3} (Murphy et al., 2014) quickly reach equilibrium between gas and particle phases for all particle sizes. As a result, the contribution to growth is proportional to the aerosol mass distribution (Pierce et al., 2011; Riipinen et al., 2011; Donahue et al., 2011; Zhang et al., 2012), limiting the growth of ultrafine particles. This type of growth is referred to as "thermodynamic condensation" by Riipinen et al. (2011) and "quasi-equilibrium" growth by Zhang et al. (2012); we will refer to this type of condensation as "SVOC-like" condensation in this work.

Important characteristics for growth in these regimes is that under ELVOC-like condensation, particles in the kinetic regime (D_p < ~50 nm) all grow in diameter at the same rate (e.g. nm h^{-1}) regardless of diameter, whereas in the continuum regime (Dp > ~1 μm), particle growth rates are proportional to $1/D_p$. Conversely, SVOC-like condensation growth rates scale with D_p for all particle sizes, favoring the largest particles. Thus, if MSA participates in ELVOC-like condensation, ultrafine particles are able to grow more quickly to climatically relevant sizes (e.g. CCN) as compared to SVOC-like condensation. In reality, MSA's contribution towards growth likely lies between these two limiting cases: as MSA is an acid, its volatility will depend on not only temperature but also relative humidity and gas-phase bases (e.g. Barsanti et al., 2009; Yli-Juuti et al., 2013; Hodshire et al., 2016).

In this study, we use the GEOS-Chem-TOMAS global chemical transport model to estimate the contribution of MSA to the aerosol size distribution and resulting radiative effects. We examine (1) MSA condensation assumptions, testing the limiting cases of growth (ELVOC-like vs SVOC-like) as well as a parameterization of volatility dependent on temperature, water vapor, and gas-phase bases built from a phase-equilibrium model and (2) how the contribution of MSA changes depending on whether or not it is allowed participate in nucleation. We further use global measurements of aerosol

Anna Lily Hodshire 2/13/2019 8:41 PM
Deleted: ; it

Anna Lily Hodshire 2/13/2019 8:41 PM
Deleted: and

Anna Lily Hodshire 2/13/2019 8:41 PM
Deleted: t

size distributions as compiled by Heintzenberg et al. (2000) and MSA mass as observed on the ATom mission to compare the various model assumptions. Our goals are to determine the sensitivity of the aerosol size distribution and radiative impacts implied by the various assumptions, and to see if the assumptions can be constrained by observations. This study is a first look at how MSA might impact the global aerosol size distribution and associated climate effects by considering the sensitivity of its assumed volatility and ability to impact nucleation. Along with our model analyses of MSA, we provide a detailed overview of the calibration applied to an Aerodyne high-resolution time-of-flight aerosol mass spectrometer (AMS) for detecting MSA during the ATom mission in the supplemental information as a general reference for the AMS community.

2 Methods

2.1 Model description

In this work, we use the GEOS-Chem chemical transport model version 10.01 (http://geos-chem.org) coupled to the online TwO-Moment Aerosol Sectional (TOMAS) microphysical module (Adams and Seinfeld, 2002; GEOS-Chem-TOMAS as described in Kodros et al., 2016; 2017) to test the sensitivity of the aerosol size distribution to the addition of a marine secondary organic aerosol (SOA) species, represented in this work by methanesulfonic acid (MSA), of varying effective volatility and nucleation capability. The version of GEOS-Chem-TOMAS (GC-TOMAS) used here has 47 vertical levels, a horizontal resolution of 4°x5° (~400 km at mid latitudes), and GEOS-FP reanalysis (http://gmao.gsfc.nasa.gov) for meteorological inputs. GC-TOMAS uses 15 size sections spanning dry diameters from approximately 3 nm - 10 μm and explicitly tracks total particle number as well as sulfate, sea salt, dust, hydrophilic OA, hydrophobic OA, internally mixed BC, externally mixed BC, and water mass (Lee and Adams, 2012). Biomass burning emissions are simulated using the Fire INventory from NCAR version 1.0 (FINNv1) (Wiedinmyer et al., 2011). Dust emissions follow the parameterization of the DEAD scheme (Zender et al., 2003); sea-salt aerosol emissions follow the parameterization of Jaegle et al. (2011). Anthropogenic emissions except for ammonia, black carbon, and organic aerosol are from the Emissions Database for Global Atmospheric Research (EDGAR; Janssens-Maenhout et al., 2010). In Europe, Canada, the U.S., and Asia, anthropogenic emissions are overwritten by the European Monitoring and Evaluation Programme (Centre on Emissions Inventories and Projections, 2013), the Criteria Air Contaminant Inventory (http://www.ec.gc.ca/air/default.asp?lang=En&n=7C43740B-1), the National Emission Inventory from the U.S. EPA (http://www.epa.gov/ttnchie1/net/2011inventory.html), and the MIX (Li et al., 2017) inventories, respectively. Black and organic carbon emissions from fossil-fuel and biofuel combustion processes are from Bond et al. (2007). Grid-box gas-phase concentrations of NH_3 are used in determining the volatility regime of MSA in the MSA parameterization (Sect. 2.2): global anthropogenic, biofuel, and natural ammonia sources are from the Global Emissions InitiAtive (GEIA) (Bouwman et al., 1997). Anthropogenic ammonia emissions are overwritten over Europe, Canada, the U.S., and Asia using the same regional

Anna Lily Hodshire 2/12/2019 9:25 PM
Deleted: Regional EDGAR overwrites are used as follows: b

Anna Lily Hodshire 2/12/2019 9:25 PM
Deleted: In Europe, Canada, the U.S., and Asia, anthropogenic emissions are overwritten by the European Monitoring and Evaluation Programme (Centre on Emissions Inventories and Projections, 2013), the Criteria Air Contaminant Inventory (http://www.ec.gc.ca/air/default.asp?lang=En&n=7C43740B-1), the National Emission Inventory from the U.S. EPA ((http://www.epa.gov/ttnchie1/net/2011inventory.html), and the MIX (Li et al., 2017) inventories, respectively.

inventories discussed above for these regions. Ammonia emission from biomass burning are from FINNv1 (above). All simulations are run for 2014, with one month of model spinup that is not included in the analysis. All results are presented as annual or monthly averages.

We use the default (at the time of this model version) GEOS-Chem DMS emissions inventory (Kettle et al., 1999; Kettle and Andreae 2000) for this study. We acknowledge that the updated DMS inventory of Lana et al. (2011) includes more up-to-date measurements than the default DMS inventory for GEOS-Chem v10.01. Their work found that the default climatology overpredicted DMS emissions in some latitudes/seasons but underpredicted DMS emissions in other latitudes/seasons. We found, however, that using the Lana emission inventory led to minor differences in MSA impacts spatially but overall, similar magnitudes of changes were observed. The supplement Sect. S2 provides more analysis of the two different emissions inventories.

In the standard GEOS-Chem DMS mechanism, DMS reacts with OH through the OH addition pathway to form molar yields of 0.75 SO_2 and 0.25 MSA (Chatfield and Crutzen, 1990; Chin et al., 1996). As discussed in the introduction, laboratory studies have reported variable yields of SO_2 and MSA from DMS oxidation by OH addition. We do not test the sensitivity of our simulations to other pathways, and this is a source of uncertainty. DMS also reacts with the nitrate radical (NO_3) to form a molar yield of 1 SO_2. SO_2 can then (1) react further in the model with OH to form gas-phase sulfuric acid, (2) undergo aqueous oxidation with H_2O_2 or O_3 to form condensed sulfate, or (3) be lost through dry and wet deposition processes (Pierce et al., 2013). Pierce et al. (2013) found that in GC-TOMAS (v8.02.02), 26% of global SO2 formed sulfate through aqueous chemistry and 13% formed sulfuric acid through gas-phase reaction with OH (the rest was lost through dry and wet deposition). The sulfate formed through aqueous chemistry is added to CCN-sized particles when activated in clouds, whereas the sulfuric acid formed from OH reactions participates in nucleation and irreversible condensation to particles of all sizes. Prior to this work, the DMS/SO_2-oxidized sulfuric acid and sulfate was included in the size-resolved portion of the GC-TOMAS model but MSA was not. In this study, we include MSA in the size-resolved microphysics of the model. The contribution of MSA from DMS towards the sulfate budget and the size distribution as a function of particle size will then depend on both MSA's volatility and ability to participate in nucleation, as discussed below. A discussion of alternative oxidation pathways of DMS and the potential importance of aqueous-phase DMS chemistry (currently not included in GEOS-Chem) is provided in Sect 2.6.

Nucleation is simulated via a ternary nucleation scheme involving water, sulfuric acid, and ammonia (Napari et al., 2002), scaled with a global tuning factor of 10^{-5} (Jung et al., 2010; Westervelt et al., 2013). In ammonia-limited regions (less than 1 pptv), a binary nucleation scheme involving water and sulfuric acid (Vehkamaki et al., 2002) is instead used. When MSA is assumed to participate in nucleation, it is treated as an extra source of sulfuric acid for the ternary and binary nucleation schemes within the model. Growth and loss of nucleated particles between 1 and 3 nm is simulated using the parameterization of Kerminen et al. (2004) (Lee et al. 2013) with growth in this size range controlled by the pseudo-steady-state sulfuric acid (Pierce and Adams, 2009b) and MSA when it participates in nucleation.

Anna Lily Hodshire 2/13/2019 8:46 PM
Deleted: See t

Anna Lily Hodshire 2/13/2019 8:46 PM
Deleted: for

Anna Lily Hodshire 2/12/2019 11:01 PM
Formatted: Subscript

SOA in GC-TOMAS is traditionally formed from terrestrial biogenic sources, with the biogenic source represented by 10% of the monoterpene emissions, totalling to 19 Tg(SOA) yr^{-1}; we further include 100 Tg(SOA) yr^{-1} spatially correlated with CO to represent anthropogenic SOA and anthropogenically-controlled biogenic SOA (Spracklen et al., 2011; D'Andrea et al., 2013). The default GC-TOMAS setting is for SOA to form through effective nonvolatile condensation (ELVOC-like condensation) onto pre-existing particles at the time of emission of the parent compound. However, it is possible to instead have SOA form in GC-TOMAS through quasi-equilibrium condensation (SVOC-like condensation, but still irreversible, e.g. not allowing for re-evaporation, in the model) by distributing the SOA across aerosol sizes proportional to the aerosol mass distribution. In this work, we assuming ELVOC-like SOA condensation as it performed best relative to size-distribution measurements in D'Andrea et al. (2013).

2.2 MSA volatility assumptions, calculations, and parameterization

As the effective volatility of MSA is uncertain, we use the Extended Aerosol Inorganics Model (E-AIM; http://www.aim.env.uea.ac.uk/aim/aim.php, Clegg et al., 1992; Clegg and Seinfeld, 2006a, b; Wexler and Clegg, 2002) to build a parameterization for GC-TOMAS of MSA's potential volatility as a function of temperature, relative humidity, and available gas-phase bases. E-AIM calculates the MSA equilibrium vapor pressure above the particle mixture (C_{eq} in units of µg m^{-3}), and thus we get an MSA volatility parameterization in terms of C_{eq} (Fig. 1). We also consider two ideal assumptions of MSA volatility: (1) MSA condenses as an ELVOC-like species, condensing irreversibly to aerosol of all sizes, with net condensation of MSA proportional to the Fuchs-corrected aerosol surface area. Conversely, (2) MSA condenses as an SVOC-like species, where the net condensation of MSA is proportional to the aerosol mass distribution.

As MSA is a strong acid (pKa=-1.96; Haynes, 2017), we must consider the amount of atmospheric gas-phase base present; ammonia is used in E-AIM as the representative base. Although Chen and Finlayson-Pitts (2017) found in laboratory experiments that MSA had different rates of new particle formation with amines than ammonia, GC-TOMAS currently does not include any amine speciesand thus we do not attempt to account for these variations. Figure S1 and S2 provides global annual and seasonally averaged NH_3 concentrations from GEOS-Chem-TOMAS. The effective volatility of MSA also depends on the ambient temperature (Donahue et al. 2006) and relative humidity (RH) (Chen et al., 2018). We run E-AIM for between 10-100% RH and between 240-310 K. Figure 1 shows the resulting volatility as a function of RH and temperature for conditions with no free ammonia and excess ammonia (3 times as many moles of free ammonia than moles of MSA). At low-base conditions (Fig. 1a), MSA acts essentially as a VOC (will all stay in vapor phase) below 90% RH and condenses as an ideally SVOC-like species above 90% RH for the entire input temperature range. Conversely, for excess-base conditions, we see that MSA transitions between volatilities as a function of both temperature and RH. We parameterize a transition between ELVOC-like behavior and SVOC-like behavior for excess-base conditions along the $C_{eq} = 10^{-2}$ µg m^{-3} line using the dashed line in Fig. 1b, given by:

Anna Lily Hodshire 2/13/2019 8:53 PM
Deleted: (

Anna Lily Hodshire 2/13/2019 8:53 PM
Deleted:)

Anna Lily Hodshire 2/13/2019 8:53 PM
Deleted: d

Anna Lily Hodshire 2/13/2019 8:56 PM
Deleted: ... [1]

Anna Lily Hodshire 2/13/2019 8:57 PM
Deleted: concentrations

$$T_{trans}(RH) = a - b \cdot RH + c \cdot RH^2 - d \cdot RH^3 + e \cdot RH^4 , \quad (1)$$

where RH is the relative humidity, T is the temperature, T_{trans} is the transition temperature, and a, b, c, d, and e are fit coefficients, whose values are listed in Table 1. If $T > T_{trans}$, then MSA is treated as an ideally SVOC-like species that undergoes quasi-equilibrium condensation in GC-TOMAS. If $T < T_{trans}$, then MSA is low to extremely low in volatility and will be treated as an ideally ELVOC-like species that undergoes gas-phase-diffusion-limited condensation in GC-TOMAS. We do not include a volatile region under excess-base conditions: the high-temperature, low-RH regions that this would be applicable to are globally limited and likely only occur over desert regions, where MSA formation is likely negligible. Although E-AIM predicts that MSA's volatility varies smoothly across the volatility space as a function of temperature and RH, for simplicity, we only assume three condensational regimes: SVOC-like condensation, ELVOC-like condensation, and VOC-like (no condensation).

When using this parameterization in GC-TOMAS, we use a gas-phase ammonia mixing ratio of 10 pptv as a cutoff between the no ammonia and excess ammonia cases as this roughly marks the transition from acidic to neutral aerosol (Croft et al., 2016, Supplementary Fig. 4). The gas-phase MSA production rate is explicitly tracked in the model, but not the MSA gas-phase concentrations. At the time of production, the model will then determine whether to treat MSA condensation as an effectively volatile species (no MSA condensing), an SVOC-like species (with all of the MSA produced condensing to the mass distribution), or an ELVOC-like species (with all of the MSA produced condensing to the Fuchs surface area and participating in the nucleation calculation in some simulations), based on the current T, RH, and available ammonia. For both SVOC-like and ELVOC-like condensation, the condensation is irreversible; we do not let MSA partition back to the gas phase once it is condensed as gas-phase MSA is not tracked in the model. Even this simple parameterization is a significant increase in the physical representation of MSA volatility over assuming a fixed volatility.

2.3 Descriptions of simulations

The different GEOS-Chem-TOMAS (GC-TOMAS) simulations in this study are summarized in Table 2. The default (DEFAULT_NoMSA) simulation represents a default GEOS-Chem-TOMAS simulation with only sulfate and sulfuric acid from DMS/SO_2 oxidation included in TOMAS; DEFAULT_NoMSA will be the comparison simulation for all other cases. PARAM_NoNuc uses the volatility parameterization from E-AIM (Sect 2.2), treating MSA as a non-nucleating ELVOC, an SVOC, or a VOC, depending upon the temperature, RH, and amount of ammonia in the gas-phase. ELVOC_NoNuc treats MSA condensation as ELVOC-like condensation. SVOC_NoNuc treats MSA condensation as SVOC-like condensation (but irreversible, Section 2.2). PARAM_Nuc and ELVOC_Nuc are identical to PARAM_NoNuc and ELVOC_NoNuc except that MSA is allowed to participate in nucleation with the properties of sulfuric acid, providing an upper bound on the role of MSA in nucleation. For PARAM_Nuc, MSA only participates in nucleation when MSA is in the ELVOC-like regime; for ELVOC_Nuc, MSA is always able to participate in nucleation. Finally, to determine the

Anna Lily Hodshire 2/13/2019 8:58 PM
Deleted: speces

Anna Lily Hodshire 2/13/2019 9:01 PM
Deleted:

Anna Lily Hodshire 2/13/2019 9:01 PM
Deleted:

Anna Lily Hodshire 2/13/2019 9:03 PM
Deleted: ed

Anna Lily Hodshire 2/13/2019 9:03 PM
Deleted: he

Anna Lily Hodshire 2/13/2019 9:03 PM
Formatted: Font:Italic

Anna Lily Hodshire 2/13/2019 9:03 PM
Deleted: we do not track

Anna Lily Hodshire 2/13/2019 9:04 PM
Deleted: of

contribution of sulfate and sulfuric acid from DMS/SO_2 oxidation alone to the default size distribution, we run a case with DMS emissions turned off (NoDMS_NoMSA).

In the supplementary information, we test the sensitivity of the model to the DMS concentration with two additional DMS inventories: the first is the DMS emissions inventory of Lana et al. (2011) and the second is the default DMS emissions inventory increased globally by a factor of two. As the sulfate and sulfuric acid from DMS/SO_2 oxidation is included in the default case simulation, we run new default simulations with the new DMS inventories (DEFAULT_NoMSA_Lana and DEFAULT_NoMSA_2xDMS). We use the PARAM_NoNuc case settings to determine the change in MSA's impact to the size distribution under the new DMS emissions inventories (PARAM_NoNuc_Lana and PARAM_NoNuc_2xDMS). However, the results for the contribution of MSA to the size distribution do not qualitatively change between the default DMS emissions inventory and the Lana DMS emission inventory. The contribution of MSA towards the submicron aerosol mass and thus the aerosol DRE in the 2xDMS case is roughly double that of the base DMS case (DEFAULT_NoMSA) but N3 and N80 do not significantly change for our tested metrics. Hence, we will not include these model results in the main portion of the paper. See the supplementary information, Sect. S2, Tables S1-S2, and Figs. S3-S5 for a brief analysis of the different inventories.

Anna Lily Hodshire 2/13/2019 9:06 PM
Deleted: S

Anna Lily Hodshire 2/13/2019 9:06 PM
Deleted: I

Anna Lily Hodshire 2/13/2019 9:06 PM
Deleted: 1x

2.4 Analysis of simulated radiative effects

We calculate aerosol DRE and cloud-albedo AIE following Kodros et al., (2016). The all-sky DRE is calculated offline using the monthly mean aerosol mass and number distributions from the GC-TOMAS output. The refractive indices are from GADS (Global Aerosol Dataset; Koepke et al., 1997). Aerosol optical depth (AOD), single-scattering albedo, and the asymmetry parameter are calculated from Mie code (Bohren and Huffman, 1983). Optical properties and the monthly mean albedo and cloud fractions from GEOS5 are used as inputs to the offline version of the Rapid Radiative Transfer Model for Global Climate Models (RRTMG: Iacono et al., 2008) that has been implemented for the standard (non-TOMAS) version of GEOS-Chem (Heald et al., 2014). We assume an internal mixture, spherical particles, non-absorptive OA (brown carbon is not considered in this work) and a core-shell morphology. We note that the mixing state may vary both regionally and temporally, and that using only one mixing state globally for the full year is a limitation of our analysis of the DRE.

The cloud-albedo AIE is calculated as follows: first, the CDNC is found using the activation parameterization of Abdul-Razzak and Ghan (2002) for the monthly mean aerosol mass and number distribution from the GC-TOMAS output. A constant updraft velocity of 0.5 m s^{-1} is assumed. We again assume the aerosol species are internally mixed within each TOMAS size bin to determine κ, the hygroscopicity parameter, as a volume-weighted average of the individual aerosol species (Petters and Kreidenweis, 2007). For the cloud-albedo AIE, we use an effective cloud drop radii of 10 μm as a control and then perturb this value with the ratio of the CDNC of each sensitivity case to the default case to the one-third power, following the methods of Rap et al., (2013), Scott et al., (2014), and Kodros et al., (2016):

$$r_{perturbed} = \left(\frac{CDNC_{base\ case}}{CDNC_{sensitivity\ case}}\right)^{1/3} \cdot 10\mu m\ , \quad (2)$$

RRTMG is again used to determine the changes in the top-of-the-atmosphere radiative flux from the changes in effective cloud drop radii, with monthly mean meteorological data needed as inputs again informed by GEOS5. For more details on the methods used for the DRE and cloud-albedo AIE calculations, refer to Kodros et al. (2016) and references therein.

2.5 Measurement comparisons

Heintzenberg et al. (2000) compiled 30 years (between ~1970-1999) of physical marine aerosol data from both sampling sites and field campaigns to create annual global size distribution parameters, fitting the size distributions to bimodal lognormal distributions for latitudinal bands spaced 15° apart. We compare their fitted size distributions for 30°-45°S, 45°-60°S and 60°-75°S to the annual zonal-mean size distributions for the DEFAULT_NoMSA case and each sensitivity case from the model. (There is no data available from Heintzenberg et al. (2000) for 75°S-90°S.) We note that changes in the aerosol size distributions between the measurement years and our simulated year (2014) are possible, even for these remote latitudes, and may result in apparent simulation errors and/or apparent model to measurement agreement biases.

The first and second Atmospheric Tomography Missions (ATom-1 and ATom-2) (https://espo.nasa.gov/missions/atom/content/ATom) took place from July 28 to August 22 of 2016 and January 26-February 22 of 2017, respectively. Carrying a comprehensive gas and particle chemistry payload, the NASA DC-8 aircraft systematically sampled the remote atmosphere, profiling continuously between 0.2 and 12 km. The data for both missions is publicly available (Wofsy et al, 2018). As a part of the instrumentation on board, a highly customized Aerodyne high-resolution time-of-flight aerosol mass spectrometer (AMS in the following; DeCarlo et al, 2006; Canagaratna et al, 2007) continuously measured the composition of submicron (PM_1), non-refractory aerosol at 1 Hz time resolution. The principle of operation and instrument/aircraft-operation specifics have been described in detail elsewhere (Dunlea et al., 2009; Kimmel et al., 2011; Schroder et al., 2018; Nault et al., 2018) and only the aspects specific to MSA quantification are discussed here.

The instrument flew in the same configuration for all four ATom missions. MSA data from the third and fourth ATom missions, ATom-3 and ATom-4, were not used in this study, but the calibration details discussed in Sect. S5 apply to these missions, as well. Overall sensitivity (as determined daily from the ionization efficiency of nitrate, IE_{NO3}), relative ionization efficiencies and particle transmission (all determined periodically in the field) were stable over all four deployments. Particle phase MSA concentrations for all ATom flights are reported based on the intensity of the highly specific marker ion $CH_3SO_2^+$ (Phinney et al, 2006, Zorn et al, 2008). The quantification of MSA PM_1 concentrations from the signal intensity of the $CH_3SO_2^+$ fragment is described in detail in the SI, Sect. S5. Positive Matrix Factorization (Paatero 1994; Ulbrich et al., 2009) of the ATom-1 organic aerosol (OA) and sulfate data confirmed the specificity of the marker ion for MSA and the consistency of the field mass spectra with those acquired in the MSA calibrations. Importantly, it also confirmed that the AMS response to MSA is independent of the aerosol acidity, which varied significantly over the range of conditions found in ATom. Further details are provided in Sect S5.

For the data presented here, the AMS raw data was processed at 1 minute resolution. Under those conditions, the detection limit of MSA was in the range 1.5-3 ng sm^{-3} (0.3-0.6 pptv), and will decrease with the square root of the number of

Anna Hodshire 2/13/2019 2:59 PM
Deleted: ,

Anna Hodshire 2/13/2019 2:59 PM
Deleted: including the

Anna Hodshire 2/13/2019 2:59 PM
Deleted: whose data was

Anna Hodshire 2/13/2019 2:59 PM
Deleted: for whom

Anna Lily Hodshire 2/13/2019 9:10 PM
Deleted: ,

Anna Lily Hodshire 2/13/2019 9:12 PM
Deleted: concluding in May 2018.

averaged 1-minute data points. The uncertainty in the MSA quantification as detailed in the SI, Sect. S5, is comparable to that of sulfate, hence the overall uncertainty in the quantification is estimated to be +/-35% (2 standard deviations; Bahreini et al., 2009).

We compare our sensitivity simulations to the ATom-1 and ATom-2 data as follows: we subtract the DEFAULT_NoMSA sulfate mass (that accounts for sulfate and sulfuric acid from DMS/SO_2 oxidation but not MSA) for the months of August (ATom-1) and February (ATom-2) from the sulfate mass for the months of August and February for each sensitivity case that includes MSA for each grid box. The resultant differences in sulfate mass represents the model-predicted contributions of MSA to the total sulfur budget for each case. This is an imperfect approach, as the additional aerosol mass from the contribution of MSA will change the size distribution, therefore changing rates of wet and dry deposition, and is a limitation of this study. We then compare the measured and predicted MSA mass by first averaging every ATom data point that falls within a given GC-TOMAS grid box. We then compare each averaged data point to that model grid box. The ATom data used in our analysis lies within 150-180° W (the Pacific ocean basin) and 10-40° W (the Atlantic ocean basin), and thus we use zonal averages of these longitude bands for both the ATom data and the GC-TOMAS output. We note that comparing monthly mean simulated values from 2014 to airborne measurements from a single point in time in 2016 and 2017 contributes to the apparent simulation errors. We also note that we use the full size range (3 nm -10 µm) of sulfate from the model output whereas the ATom data is submicron. However, the model-predicted percent difference in MSA mass between the full range and the submicron mass is well under 1% (not shown).

To evaluate model performance, we calculate the log-mean bias (LMB), the slope of the log-log regression (m), and the coefficient of determination (R^2) between each cosampled GC-TOMAS grid box and averaged measurement point that falls within that GC-TOMAS grid box. The LMB is calculated through:

$$LMB = \frac{\sum_i^N (log_{10}(S_i) - log_{10}(O_i))}{N}, \quad (3)$$

where S_i and O_i are the simulated and observed MSA masses, respectively, for each data point i, and N is the number of data points. A LMB of 1 means that on average, the model overestimates the measurements by a factor of 10^1 (10); a LMB of -1 means that on average, the model underestimates the measurements by a factor of 10^{-1} (0.1); a LMB of 0 indicates no bias between the model and measurements (10^0 = 1.00). LMB, m, and R^2 are summarized in Fig. 8 (discussed in Sect. 3.4). Since MSA is observed only in the particle-phase in the ATom measurements, we do not include the NoDMS_NoMSA (no DMS emissions in the model) sensitivity case in our analysis of the ATom data. We present the aggregated results of the two campaigns, as well as results for each campaign and ocean basin. The ATom-1 mission provided more data points than the ATom-2 missions (1258 vs. 1000) and thus the aggregate results are slightly skewed towards the ATom-1 results.

Anna Hodshire 2/13/2019 3:03 PM
Deleted: (log_{10}

Anna Lily Hodshire 2/12/2019 10:16 PM
Deleted: Table 4

2.6 Study caveats

This study is intended to examine the sensitivity of the aerosol size distribution and radiative impacts implied by the various sensitivity treatments of MSA (Table 2). However, our treatments of DMS and MSA still fall short of what is

currently known about organic condensational behavior. Assuming idealized semivolatile condensation with no re-evaporation due to conditional changes (e.g. change in temperatures, RH) may overestimate the amount of MSA able to condense on particles; but it may also underestimate particle-phase MSA if conditions for condensation switch from unfavorable to favorable after MSA chemical production. Further, relying on E-AIM simulations to construct our volatility parameterization could have hidden biases due to an incomplete understanding of the system. We are also neglecting known as well as gas-phase and aqueous-phase oxidation pathways of DMS that are currently not included in GEOS-Chem. The standard GEOS-Chem model does not include DMS oxidation through the OH or halogen addition pathways to dimethylsulfoxide (DMSO). DMSO chemistry reduces the yield of sulfate formation from DMS/SO_2 oxidation (Breider et al., 2014) by increasing the yields of both gas-phase and aqueous phase MSA as well as aqueous-phase dimethyl sulfone ($DMSO_2$), another stable oxidation product (Hoffmann et al. 2016). To reduce the number of parameters for this study, we do not include the DMSO pathway. We acknowledge that neglecting this pathway will slightly bias our estimates of the contributions to the aerosol size distribution of sulfate and MSA mass high and low, respectively. Further, aqueous-phase production of MSA would condense on CCN-sized particles, similar to aqueous phase sulfate (Sect 2.1), shifting the size distribution to larger sizes. Heterogeneous oxidation may limit the lifetime of MSA in the particle phase (Mungall et al., 2017; Kwong et al., 2018), although the reactive uptake coefficients from these studies are somewhat dissimilar, indicating a need for further study of the system. Regardless, neglecting heterogeneous chemistry could overestimate the estimate of the contribution of MSA to aerosol mass. Finally, if MSA does participate in nucleation, it is unlikely that it will behave exactly like sulfuric acid, as it is treated here. All of the limitations described above are important and require further testing in detailed chemical models and chemical-transport models in order to determine their effects.

Another limitation of this study is our reliance upon the current ammonia inventory in GEOS-Chem as well as our cutoff value of 10 ppt of ammonia between the no ammonia and excess ammonia regimes (Sect. 2.2). Uncertainties in the ammonia inventories over the oceans could change our results, as could a different cutoff value. As this study is focused on MSA sensitivities, we will leave sensitivities of MSA to ammonia for a future study. It is important to note that other bases such as amines could also have an important effect on MSA's effective volatility (e.g. Chen and Finlayson-Pitts, 2017). However, the standard GEOS-Chem currently does not account for gas-phase bases beyond ammonia, and this sensitivity will also be left for a future study.

We do not test the sensitivity of our simulations to the binary and ternary nucleation schemes used in this study, including potential sensitivity to the global tuning factor of 10^{-5} that was developed for continental regions (Jung et al., 2010; Westervelt et al., 2013). This source of uncertainty should be tested in future studies, as well.

3 Results and Discussion

Figure 2 shows the global annual mean percent change (at 900 hPa and zonally) for submicron mass by adding MSA for the PARAM_NoNuc, ELVOC_NoNuc, SVOC_NoNuc, PARAM_Nuc, and ELVOC_Nuc simulations. Figure 3 shows the global annual mean percent change in N3 and N80 due to addition of MSA at 900 hPa and zonally for all model

Anna Lily Hodshire 2/13/2019 9:18 PM
Deleted: We are also neglecting known as well as gas-phase and aqueous-phase oxidation pathways of DMS that are currently not included in GEOS-Chem.

Anna Lily Hodshire 2/13/2019 9:19 PM
Deleted: Regarding chemistry uncertainties, t

Anna Lily Hodshire 2/12/2019 11:27 PM
Formatted: Superscript

levels for each of these cases, and Fig. 4 shows the corresponding global annual cloud-albedo AIE and DRE of MSA. Figure 5 shows the global annual mean percent contribution from DMS/SO_2 oxidation (at 900 hPa and zonally) alone (not including MSA) to submicron mass, N3, N80, AID, and DRE. Figure 6 and Table S3 summarises the results of Figs. 2, 3, 4, and 5. All of the numerical statistics presented in Sects. 3.1-3.4 are for the annual mean, either globally or between 30°-90°S. Each case with MSA is analyzed for the change relative to DEFAULT_NoMSA to determine the impact that MSA has on the size distribution and resulting radiative effects (positive values indicate that the inclusion of MSA increases a given metric). For reference, Figure S6 provides the absolute number concentration for N3 and N80 at 900 hPa and zonally for all model levels for the DEFAULT_NoMSA simulation. We will refer back to these figures in the following sections.

Jeffrey Pierce 2/13/2019 8:41 PM
Comment [1]: leave this for the caption

Jeffrey Pierce 2/13/2019 8:41 PM
Deleted: (denoted by AIE)

Anna Lily Hodshire 2/12/2019 10:22 PM
Deleted: 7

3.1 Volatility-dependent impact of MSA if MSA does not participate in nucleation

The top rows of Figs. 2 and 3 show the global annual mean percent change at 900 hPa and zonally from adding MSA using the volatility parameterization without nucleation (PARAM_NoNuc - DEFAULT_NoMSA) for submicron aerosol mass (Fig. 2) and N3 and N80 (Fig. 3). By adding MSA with these assumptions, we predict at 900 hPa an increase in submicron mass of 0.7% globally and 1.3% between 30°S-90°S; a decrease in N3 of -3.9% globally and -8.5% between 30°S-90°S; and an increase in N80 of 0.8% globally and 1.7% between 30°S-90°S (Fig. 6 and Table S3). These MSA impacts are limited by ammonia availability. Figures S1 and S2 show that many oceanic regions are predicted to have annual and seasonal ammonia mixing ratios of less than 10 ppt. Below 10 pptv of ammonia, MSA condensation as SVOC-like or VOC-like (no condensation) (Fig. 1a) and MSA condensation will only be SVOC-like if the RH > 90%; under these conditions for the majority of the year, MSA will be a VOC-like species over Antarctica (low RH conditions) and often an SVOC-like species over the southern-ocean boundary layer (high RH conditions). Only in the Southern Hemisphere (SH) winter months does ammonia exceed 10 ppt over appreciable regions in the southern oceans (Fig. S2); during this time, MSA condensation is ELVOC-like due to cold temperatures (Fig. 1b). As shown in D'Andrea et al. (2013), ideal-SVOC material largely condenses primarily to accumulation-mode particles, which in turn suppresses N3 through increased coagulation and reduced nucleation and has little impact on N80. In the midlatitudes, the annual and seasonal ammonia concentrations often exceed 10 ppt, and thus MSA condensation will be either ELVOC-like under low-temperature and/or high-RH conditions or SVOC-like under high-temperature and/or low-RH conditions. D'Andrea et al. (2013) showed that adding ELVOC material can increase N80 by increasing growth of ultrafine particles but also can suppress N3 through the same coagulation/nucleation feedbacks. This combination of ammonia-rich and ammonia-poor regions lead to MSA giving an overall weak increase in N80 with a large suppression of N3 in some regions. We note that these results are somewhat sensitive to the simulated ammonia concentrations and may be sensitivity to the ammonia cutoff of 10 ppt in the MSA-volatility parameterization. As there are already uncertainties in many other dimensions, we do not attempt to quantify the sensitivity of MSA towards ammonia in this work.

The idealized volatility cases, ELVOC_NoNuc (Figs. 2 and 3, second row) and SVOC_NoNuc (Figs. 2 and 3, third row) help to highlight and further explain MSA's volatility-dependent contribution towards growth. In both of these cases,

100% of the formed MSA goes to the particle phase, unlike with the MSA volatility parameterization, where MSA may not condense in the absence of base at lower RHs. Hence, the global annual MSA mass is nearly double in these cases compared to when using the parameterization (Table 2; Fig. 2). The addition of MSA in the ELVOC_NoNuc case allows for an increase in condensable material that condenses to the Fuchs-corrected surface area through ELVOC-like condensation, which increases the growth rate of all particle sizes. Conversely, MSA in SVOC_NoNuc allows for an increase of SVOC-like material that will condense preferentially to larger particles through SVOC-like condensation (but still irreversible condensation). In both the ELVOC_NoNuc and SVOC_NoNuc cases, N3 concentrations are reduced due to increased coagulational losses and decreased nucleation rates because of the added MSA mass (D'Andrea et al., 2013). When MSA condensation is treated as ELVOC-like, the smaller particles grow more quickly into the larger sizes, so N80 increases by 9.1% globally and by 22.2% between 30°S-90°S at 900 hPa (Fig. 6 and Table S3). When MSA condensation is instead treated as SVOC-like, the largest particles uptake MSA preferentially to smaller particles, and the N80 are not greatly impacted by the addition of MSA. The slight boost in N80 for SVOC_NoNuc in the tropical upper troposphere (UT) is due to the very low accumulation-mode concentration in this region: the SVOC material condenses to ultrafine particles in this region.

Anna Lily Hodshire 2/13/2019 9:34 PM
Deleted: (

Anna Lily Hodshire 2/13/2019 9:34 PM
Deleted:)

The changes in DRE and cloud-albedo AIE resulting from the addition of MSA for these three no-MSA-nucleation cases (Fig. 4, top three rows) depend roughly on the changes in N80 (the activation diameter for determining CDNC will depend on local particle hygroscopicity and concentrations). The DRE generally scales linearly with aerosol mass (Fig. 2, top three rows). As MSA is assumed to have the same properties as sulfate, which is is assumed to be purely scattering, any increases in MSA mass results in a negative radiative effect. However, the DRE also depends on aerosol size; the scattering efficiency peaks between ~300-900 nm, depending upon the aerosol composition and shape (Seinfeld and Pandis, 2016, their Fig. 15.8). The change in DRE when MSA is included using the volatility parameterization (PARAM_NoNuc) is less negative than that of ELVOC_NoNuc and SVOC_NoNuc at -15 mW m^{-2} globally (-26 mW m^{-2} between 30°S-90°S), because the parameterization yielded a smaller mass increase than the ideal volatility simulations. ELVOC_NoNuc and SVOC_NoNuc have almost identical changes in submicron aerosol mass (Fig. 6; Table S3) but the DRE is -25 mW m^{-2} globally (-44 mW m^{-2} between 30°S-90°S) for SVOC_NoNuc and -0.02 W m^{-2} globally (-34 mW m^{-2} between 30°S-90°S) for ELVOC_NoNuc (Fig. 6; Table S3). MSA will preferentially condense to larger aerosol when its condensation is SVOC-like, and so even though ELVOC_NoNuc shows a larger increase in N80, SVOC_NoNuc increases the fraction of particulate mass in the peak scattering efficiency regime.

The cloud-albedo AIE instead scales the with aerosol number concentration of particles large enough to act as CCN: PARAM_NoNuc's cloud-albedo AIE (-8.6 mW m^{-2} globally, -17 mW m^{-2} between 30°S-90°S) reflects the small increase in N80 (0.8% globally and 1.7% between 30°S-90°S at 900 hPa) (Fig. 6; Table S3). The larger increase in N80 for ELVOC_NoNuc results in the larger cooling tendency in the cloud-albedo AIE, at -0.075 W m^{-2} globally (-150 mW m^{-2} between 30°S-90°S), and the slight decrease in N80 for SVOC_NoNuc results in the slight warming tendency in cloud-albedo AIE at 7.5 mW m^{-2} globally (11 mW m^{-2} between 30°S-90°S) (Fig. 6; Table S3).

These annual results show in Fig. 6 and Table S3 that if MSA does not take part in nucleation, the submicron aerosol mass will increase, causing a cooling tendency in the DRE, and N3 will decrease regardless of the volatility assumed. However, the changes in N80 are sensitive to the volatility assumption and will only increase if MSA condensation is ELVOC-like at least over some spatial and temporal scales, thereby causing a further cooling tendency in the cloud-albedo AIE.

3.2 Volatility-dependent impact of MSA if MSA does participate in nucleation

To test the potential influence on aerosol size distributions if MSA contributes to nucleation, we allow MSA to participate in binary and ternary nucleation with the same efficacy as sulfuric acid. This provides an upper bound in the potential contribution of MSA towards nucleation (at least for the nucleation schemes tested here). Figures 2, 3, and 4 (fourth rows) show the global annual mean percent changes between DEFAULT_NoMSA and PARAM_Nuc. MSA will have the same effective volatility as discussed for PARAM_NoNuc (Sect. 3.1) but will now participate in nucleation under ELVOC-like regimes. For PARAM_Nuc, we can clearly see that when the ammonia concentrations reach above 10 ppt in the SH winter months over the Southern Ocean (Fig. S4), MSA acts as an ELVOC-like species and contributes strongly to nucleation in these sulfuric-acid poor regions. The addition of MSA in ELVOC_Nuc has the largest impact on N3, N80, and the cloud-albedo AIE of any of our cases with an increase in N3 of 153.4% globally (397.7% between 30°S-90°S), an increase in N80 of 23.8% globally (56.3% between 30°S-90°S), and a decrease for the cloud-albedo AIE of -0.18 W m^{-2} globally (-0.39 W m^{-2} between 30°S-90°S). MSA in PARAM_Nuc also has a large increase in N3 (112.5% globally and 309.9% between 30°-90° Sat 900 hPa) but only increase N80 by 2.1% globally (4.4% between 30°-90° S), again indicating that MSA often undergoes SVOC-like or ELVOC-like condensation within the volatility parameterization.

The increase in N80 from MSA in PARAM_Nuc is about double that of the increase from MSA in PARAM_NoNuc, and the change in cloud-albedo AIE is similarly slightly double for PARAM_Nuc. The global annual changes in submicron mass and the DRE is quite similar between the two PARAM cases. However, N80 increases more over the northern hemisphere (NH) high latitude ocean regions for PARAM_Nuc than for PARAM_NoNuc, and as a result, the northern oceans experience a stronger regional negative cloud-albedo AIE when MSA is allowed to participate in nucleation. As noted in Sect. 3.1, there are uncertainties from the ammonia concentrations and cutoff point of 10 ppt for PARAM_Nuc, but we will not attempt to quantify them here.

These results indicate that if MSA does participate in nucleation, the largest climate-relevant change is anticipated to be an increased cooling tendency for the cloud-albedo AIE as compared to if MSA does not participate in nucleation. The change in DRE will be similar though, as MSA mass is not predicted to significantly change between non-nucleating and nucleating cases. This study provides an upper bound on the contribution of MSA to nucleation: if MSA is less efficient at nucleating than sulfuric acid, it is present in relatively sulfuric-acid poor regions and would still be able to increase N3 concentrations (although possible by less than predicted here). Microphysical feedbacks (increased condensation and

Anna Lily Hodshire 2/13/2019 9:36 PM
Deleted: model

Anna Lily Hodshire 2/13/2019 9:36 PM
Deleted: the

Anna Lily Hodshire 2/12/2019 11:36 PM
Formatted: Font color: Auto

Anna Lily Hodshire 2/12/2019 11:36 PM
Formatted: Font color: Auto

coagulation sinks from increased N80) will then limit the effect that small changes in N3 can have on N80 and radiative effects.

3.3 Comparison of MSA impacts to the contribution from SO_2 formed in DMS oxidation

By removing DMS from the simulation entirely (NoDMS_NoMSA case; Figs. 5 and 6 and Table S3), we determine the baseline contribution of the simulated sulfuric acid and sulfate from DMS/SO_2 oxidation to the aerosol size distribution in GEOS-Chem-TOMAS at 900 hPa. The sulfate and sulfuric acid from DMS/SO_2 oxidation provides larger changes in submicron mass and N80 than MSA does in any of our sensitivity cases. The contribution of SO_2 from DMS to submicron mass is 4-6 times that of the MSA contribution. However, about ⅔ of this mass increase from DMS/SO_2 comes through aqueous oxidation of SO_2 to sulfate, which adds mass (but not number) to already-CCN-sized particles (Pierce et al., 2013) suppressing nucleation and growth. The remaining ~⅓ of the mass comes from gas-phase formation of sulfuric acid, which nucleates particles and condenses irreversibly to the Fuchs-corrected surface area, potentially increasing the number of CCN-sized particles. Overall, N3 and N80 increase due to the inclusion of the DMS/SO_2 pathway (N3 by 7.3% and N80 by 12.2% globally and N3 by 19.5% and N80 by 24.3% between 30°S-90°S at 900 hPa). The increases in both N3 and N80 are strongly damped by the formation of aqueous sulfate. The changes in N3 at 900 hPa indicate the relative importance of the sulfuric acid produced by DMS/SO_2 oxidation for nucleation compared to other sources of sulfuric acid. N3 generally increases in remote regions where sulfuric acid from DMS/SO_2 oxidation would be the main source of sulfuric acid. There are also regions of decrease in N3 in remote regions: the condensation and coagulation sinks increase from aqueous sulfate formation, and in some regions this competition effectively scavenges N3 faster than sulfuric acid from DMS/SO_2 oxidation forms new particles. Because of the large increase in submicron mass from the sulfuric acid and sulfate from DMS/SO_2 oxidation, the DRE from DMS/SO2 is -120 mW m^{-2} globally (-173 mW m^{-2} between 30°S-90°S), about 5 times larger than MSA for any of our assumptions. On the other hand, the cloud-albedo AIE cooling tendency of -46 mW m^{-2} globally and -38 mW m^{-2} between 30°S-90°S, was within the range of cloud-albedo AIEs from MSA that we predicted, which is due to the N80 damping of DMS/SO_2 due to aqueous sulfate formation. Thus, overall we predict the DRE from MSA to be at least 5 times weaker than from DMS/SO_2, but the cloud-albedo AIE may be of similar magnitude depending on the properties of MSA.

Anna Lily Hodshire 2/13/2019 9:40 PM
Deleted: H_2SO_4 $_{DMS}$

Anna Lily Hodshire 2/13/2019 9:40 PM
Formatted: Not Superscript/ Subscript

Anna Lily Hodshire 2/13/2019 9:40 PM
Formatted: Not Superscript/ Subscript

3.4 Analysis of model-measurement comparisons

Figure 7 shows the comparison between the annual zonal-mean particle number size distributions compiled in Heintzenberg et al. (2000; hereon referred to as Heintzenberg) and the GC-TOMAS simulated annual-mean particle number size distributions within the boundary layer for the latitude bands of 30°S-45°S, 45°S-60°S, and 60°S-75°S (no data was provided in Heintzenberg between 75°S-90°S). We focus this comparison to the southern oceans region as this region has the strongest influence from DMS and its oxidation products. It is also less likely to be influenced by changing anthropogenic emissions that may have occurred between the time of the measurements compiled in Heintzenberg (between ~1970-1999)

and 2014 (the year of the model run) than higher latitudes (e.g. Pierce and Adams, et al., 2009a; Gordon et al., 2017). We see that all model simulations underpredict both the Aitken and accumulation modes of Heintzenberg, but that the simulations that allow MSA to participate in nucleation (ELVOC_Nuc and PARAM_Nuc) give the best model-to-measurement agreements for the Aitken mode for each latitude band, with ELVOC_Nuc performing the best across the model cases. Further, ELVOC_Nuc shows the highest number of particles in the accumulation mode, particularly between 60°-75° S. These results point to the necessity of another source of ultrafine particles over the southern oceans than is being currently accounted for in the model. These particles may be produced locally from ultrafine sea spray (Pierce and Adams, 2006), local nucleation (not necessarily through MSA), or entrainment of ultrafine particles from the free troposphere (Clarke et al., 2002).

For the ATom mission, Figure 8 provides 1:1 plots for each sensitivity case's predicted MSA mass versus the observed MSA mass from the aggregated ATom-1 and ATom-2 campaigns. Each subplot provides the LMB, m, and R^2 statistics for the given sensitivity case. LMB, m, and R^2 statistics are also provided for each campaign and ocean basin in Figs. S7-S10; Figures S11-S14 show the zonally averaged simulated MSA concentrations for each basin and campaign with the corresponding particle-phase MSA measurements overlaid. Figure 8 indicates that for the aggregated campaigns, the model cases in which MSA always condenses to the particle phase (the SVOC_NoNuc, ELVOC_NoNuc, and ELVOC_Nuc cases) overpredict MSA mass, with positive LMBs between 0.27 and 0.3 (overpredictions of a factor of 1.9-2). The PARAM_NoNuc and PARAM_Nuc cases do not allow MSA to condense to the particle phase under low-base/high-temperature/low-RH conditions (Fig.1). As a result, the PARAM cases instead slightly underpredict MSA mass, with LMBs of -0.1 and -0.08 (underpredictions by a factor of 0.79 and 0.83). Overall, when the parameterization is not used, too much MSA mass is allowed to condense relative to the observations. Given the large improvement in LMB through the use of the parameterization (with roughly similar R^2 and m values), we feel that these results support the use of the volatility parameterization of MSA.

The R^2 values are quite low across cases, with the parameterization cases giving the highest R^2 values, at 0.09. The m values are similarly low, with the SVOC_NoNuc, ELVOC_NoNuc, and ELVOC_Nuc cases giving the highest m values, at 0.33-0.34. However, we are comparing monthly grid-box mean model predictions to individually grid-box averaged measurements taken during a different year than the simulation year. Further, using monthly mean model predictions on the y-axis (Fig. 8) decreases variability, which reduces the slope. These considerations contribute to lower values of R^2 and m.

Anna Lily Hodshire 2/13/2019 9:42 PM
Deleted: cases with the

The Heintzenberg and ATom model-measurement comparisons disagree on which MSA assumptions lead to the best performance in GC-TOMAS. However, the Heintzenberg analysis considers number size distribution whereas the ATom analysis considers total particle-phase MSA mass. The model-measurement improvement for the Heintzenberg study is most strongly seen within the Aitken mode (the smallest reported particle sizes). Aitken-mode-sized particles contribute little to total mass compared to larger particles. Further, it is not possible to determine from this study whether the source of ultrafine particles that could explain the size of the Aitken modes in Heintzenberg comes from MSA another primary or

secondary source. On the other hand, the ATom comparison suggests that using the MSA volatility parameterization helps predict the MSA mass concentrations more accurately.

4 Conclusions

We used the GEOS-Chem chemical transport model coupled to the TOMAS aerosol microphysics module to test the sensitivity of the aerosol size distribution and resulting changes in the direct and indirect effects to the condensational and nucleating behavior of methanesulfonic acid (MSA), an oxidation product of dimethylsulfide (DMS). GEOS-Chem-TOMAS (GC-TOMAS) normally simulates sulfuric acid and sulfate from DMS/SO_2 oxidation but does not include MSA within the size-resolved portion of the model; we used this setup as our default model case (DEFAULT_NoMSA). We considered both the global annual mean size distributions and the annual mean in the southern oceans regions (30S°-90°S) at 900 hPa for each sensitivity case compared to DEFAULT_NoMSA. We further evaluated the model output against two different measurement sets: zonal-mean number size distributions compiled from ship-based measurements taken in the southern oceans and particle-phase MSA mass concentrations obtained from aircraft data over the Atlantic and Pacific ocean basins for the months of August and February.

As the effective volatility of MSA is uncertain, we used the Extended Aerosol Inorganics Model (E-AIM) to build a parameterization for GC-TOMAS of MSA's potential volatility as a function of temperature, relative humidity, and available gas-phase base. For simplicity, we only allowed MSA to condense as ideally nonvolatile or semivolatile, or to be volatile and not condense at all under the parameterization. If MSA was ideally nonvolatile, it contributed to the size distribution through condensation proportional to the Fuchs-corrected aerosol surface area distribution (effectively nonvolatile or ELVOC-like condensation). If MSA was instead ideally semivolatile, it contributed to the size distribution through condensation proportional to the aerosol mass distribution (quasi-equilibrium or SVOC-like condensation). Regardless of the volatility treatment, condensed MSA was not allowed to evaporate back to the gas-phase, as gas-phase MSA was not explicitly tracked in the model. Along with the parameterization, we tested limiting volatility cases, allowing MSA to only be ELVOC-like or SVOC-like. We also performed separate simulations in which MSA could participate in nucleation, using both the MSA volatility parameterization and the ELVOC-like and SVOC-like MSA assumptions. (MSA participated in nucleation only when it was under ELVOC-like conditions in the parameterization; it always participated in nucleation in the ELVOC simulation). When using the volatility parameterization, including MSA in the model changed the global annual averages of submicron aerosol mass by 1.2%, N3 by -3.9% (non-nucleating) or 112.5% (nucleating), N80 by 0.8% (non-nucleating) or 2.1% (nucleating), the aerosol indirect effect by -8.6 mW m^{-2} (non-nucleating) or -26 mW m^{-2} (nucleating), and the direct radiative effect by -15 mW m^{-2} (non-nucleating) or -14 mW m^{-2} (nucleating). Across all simulations, including MSA in the model changed the global annual averages of submicron aerosol mass by 0.7% to 1.2%, N3 by -3.9% to 153.4%, N80 by -0.2% to 23.8%, the aerosol indirect effect by -0.18 W m^{-2} to 0.0075 W m-2, and the direct radiative effect by -25 mW m^{-2} to -13 mW m^{-2}, depending on the assumed volatility and nucleating ability of MSA.

The contribution from the sulfuric acid and sulfate from DMS/SO_2 oxidation to the submicron aerosol mass is 4-6 times that of the contribution from DMS/MSA, leading to a global cooling from the DRE 5-10 times that of MSA, at -120 mW m^{-2}. However, because much of the aerosol mass from DMS/SO2 is added through aqueous sulfate formation, which suppresses nucleation and growth, the changes in N3, N80, and the cloud-albedo AIE from DMS/SO_2 oxidation products are smaller and on the order of changes in these metrics from including MSA in the model.

The model-measurement annual zonal number size distribution comparisons to the ship-based measurements compiled in Heintzenberg et al. (2000) of the southern-ocean region (Fig. 11) show an underprediction of the Aitken mode across cases, with the best agreement in the Aitken mode coming from the cases that allow MSA to act as a nucleating nonvolatile compound (ELVOC_Nuc and PARAM_Nuc). These results indicate the necessity of another source of ultrafine particles over the southern oceans that is currently not being accounted for in the model. However, it is not possible to conclude based on this study where the source of extra ultrafines is coming from. More studies over the oceans detailing the chemical compositions of the smallest particle sizes are needed in order to help determine the origins of nucleating material in these remote regions.

The model-measurement comparisons of total particle-phase MSA mass from the aircraft data taken during the ATom-1 and ATom-2 campaigns compared to the predicted mean MSA mass indicate that PARAM_Nuc and PARAM_NoNuc cases perform the best, and that the cases in which MSA is always allowed to condense to the particle phase overpredict MSA mass. As the Heintzenberg and the ATom model-measurement comparisons are based on dissimilar metrics (number size distribution versus particle-phase MSA mass) over dissimilar spatial extents (surface-based ground and ship measurements versus aircraft measurements continuously profiling between 0.2 and ~13 km), we cannot definitively state that any one sensitivity case appears to best-fit both the Heintzenberg and ATom measurements. Along with these model-measurement comparisons, we provided a detailed description of the calibration for detecting MSA applied to the Aerodyne high-resolution time-of-flight aerosol mass spectrometer (AMS) present during the ATom campaigns in the supplement as a reference for the AMS community.

As there are uncertainties in both MSA's behavior (nucleation and condensation) and the DMS emissions inventory, further modelling and measurement studies on both fronts are needed to better constrain MSA's current and future impact upon the global aerosol size distribution and radiative effect. Under the simulation tested in this work, MSA tends to have small (< -0.1 W m^{-2}) global annual radiative effects (DRE and cloud-albedo AIE); in general, the forcings are predicted to be cooling effects. The contributions to the size distribution and radiative effects increase in magnitude in the southern oceans, where MSA concentrations are highest and more-pristine conditions exist. Although small, the radiative effects from MSA and the associated size distribution dependencies should be well-characterized to more-fully understand the role of changing DMS emissions in a changing climate. This study provides a first look at some of these potential dependencies and indicates possible directions for future modelling and measurement studies.

Jeffrey Pierce 2/13/2019 8:43 PM
Deleted: al

Data availability

Data for the ATom campaigns is posted publicly at https://doi.org/10.3334/ORNLDAAC/1581. The GEOS-Chem model is available at http://wiki.seas.harvard.edu/geos-chem/.

Jeffrey Pierce 2/13/2019 8:43 PM
Deleted: / will be

Author contributions

ALH, JRP, and BC defined the scientific questions and scope of this work. ALH and BC performed all GEOS-Chem model simulations and off-line calculations with help from JKK, BC, and JRP. JRP performed the E-AIM calculations. PCJ, BAN, JCS, and JLJ carried out the primary measurements and data processing for the ATom field campaign, as well as campaign supervision and design. ALH prepared the primary text with substantial contributions from JRP, JKK, BC, PCJ, and JLJ. PCJ provided the detailed description provided in the supplement of the calibration method used for detecting MSA during the ATom field campaign, with additional contributions from JLJ.

Jeffrey Pierce 2/13/2019 8:45 PM
Deleted: J

Jeffrey Pierce 2/13/2019 8:45 PM
Deleted: J

Competing interests

The authors declare that they have no competing interests.

Acknowledgements

This research was supported by the US Department of Energy's Atmospheric System Research, an Office of Science, Office of Biological and Environmental Research program, under Grant No. DE-SC0011780 and by the U.S National Oceanic and Atmospheric Administration, an Office of Science, Office of Atmospheric Chemistry, Carbon Cycle, and Climate Program, under the cooperative agreement awards #NA17OAR430001. B.C. was supported under the Climate Change and Atmospheric Research programme at 1164 NSERC, as part of the NETCARE project. The CU-Boulder group was supported by NASA NNX15AH33A and NNX15AJ23G.

References

Abdul-Razzak, H. and Ghan, S. J.:A parameterization of aerosol activation 3. Sectional representation, J. Geophys. Res., 107, 4026, doi:10.1029/2001JD000483, 2002.

Adams, P. J. and Seinfeld, J. H.: Predicting global aerosol size distributions in general circulation models, J. Geophys. Res., 107(D19), 4370, doi:10.1029/2001JD001010, 2002.

Andreae, M. O., Ferek, R. J., Bermond, F., Byrd, K. P., Engstrom, R. T., Hardin, S., Houmere, P. D., LeMarrec, F., Raemdonck, H. and Chatfield, R. B.: Dimethyl sulfide in the marine atmosphere, J. Geophys. Res., 90(D7), 12891, doi:10.1029/JD090iD07p12891, 1985.

Andreae, M. O., R. J. Ferek, F. Bermond, K. P. Byrd, R. T. Engstrom, S. Hardin, P. D. Houmere, F. LeMarrec, H. Raemdonck, and R. B. Chatfield: Dimethyl sulfide in the marine atmosphere, *J. Geophys. Res.*, 90(D7), 12891–12900, doi:10.1029/JD090iD07p12891, 1985.

Andreae, M. O.: Ocean-atmosphere interactions in the global biogeochemical sulfur cycle, Mar. Chem., 30, 1–29, doi:https://doi.org/10.1016/0304-4203(90)90059-L, 1990.

Arsene, C., Barnes, I., Becker, K. H. and Mocanu, R.: FT□IR product study on the photo□oxidation of dimethyl sulphide in the presence of NOx—Temperature dependence, Atmos. Environ., 35(22), 3769–3780, doi:10.1016/S1352-2310(01)00168-6, 2001.

Bahreini, R., Ervens, B., Middlebrook, A. M., Warneke, C., De Gouw, J. A., DeCarlo, P. F., Jimenez, J. L., Brock, C. A., Neuman, J. A., Ryerson, T. B., Stark, H., Atlas, E., Brioude, J., Fried, A., Holloway, J. S., Peischl, J., Richter, D., Walega, J., Weibring, P., Wollny, a. G., and Fehsenfeld, F. C.: Organic aerosol formation in urban and industrial plumes near Houston and Dallas, Texas, J. Geophys. Res., 114(16), D00F16, doi:10.1029/2008JD011493, 2009.

Barnes, I., Hjorth, J. and Mihalapoulos, N.: Dimethyl sulfide and dimethyl sulfoxide and their oxidation in the atmosphere, Chem. Rev., 106(3), 940–975, doi:10.1021/cr020529+, 2006.

Barsanti, K. C., McMurry, P. H., and Smith, J. N.: The potential contribution of organic salts to new particle growth, Atmos. Chem. Phys., 9, 2949–2957, doi:10.5194/acp-9-2949-2009, 2009.

Bates, T., Lamb, B., Guenther, A., Dignon, J. and E. Stoiber, R.: Sulfur Emissions to the Atmosphere from Natural Sources., 1992.

Belviso, S., Bopp, L., Moulin, C., Orr, J. C., Anderson, T. R., Aumont, O., Chu, S., Elliott, S., Maltrud, M. E., and Simó, R.: Comparison of global climatological maps of sea surface dimethyl sulfide, Global Biogeochem. Cy., 18, GB3013, https://doi.org/10.1029/2003GB002193, 2004.

Berresheim, H., Elste, T., Tremmel, H. G., Allen, A. G., Hansson, H.□C., Rosman, K., Dal Maso, M., Mäkelä, J. M., Kulmala, M., and O'Dowd, C. D.,: Gas□aerosol relationships of H2SO4, MSA, and OH: Observations in the coastal marine boundary layer at Mace Head, Ireland, *J. Geophys. Res.*, 107 (D19), 8100, doi:10.1029/2000JD000229, 2002.

Bohren, C. F. and Huffman, D. R.: Absorption and scattering of light by small particles,Wiley Interscience, New York, USA, 1983.

Bond, T. C., Habib, G., and Bergstrom, R. W.: Limitations in the enhancement of visible light absorption due to mixing state, J. Geophys. Res., 111, D20211, doi:10.1029/2006JD007315, 2006.

Bond, T. C., Bhardwaj, E., Dong, R., Jogani, R., Jung, S., Ro- den, C., Streets, D. G., and Trautmann, N. M.: Historical emissions of black and organic carbon aerosol from energy-related combustion, 1850–2000, Global Biogeochem. Cy., 21, GB2018, doi:10.1029/2006GB002840, 2007.

Bond, T. C., Doherty, S. J., Fahey, D. W., Forster, P. M., Berntsen, T., DeAngelo, B. J., Flanner, M. G., Ghan, S., Kärcher, B., Koch, D., Kinne, S., Kondo, Y., Quinn, P. K., Sarofim, M. C., Schultz, M. G., Schulz, M., Venkataraman, C., Zhang, H., Zhang, S., Bellouin, N., Guttikunda, S. K., Hopke, P. K., Jacobson, M. Z., Kaiser, J. W., Klimont, Z., Lohmann, U., Schwarz, J. P., Shindell, D., Storelvmo, T., Warren, S. G., and Zender, C. S.: Bounding the role of black carbon in the climate system: A scientific assessment, J. Geophys. Res. Atmos., 118, 5380–5552, doi:10.1002/jgrd.50171, 2013.

Bork, N., Elm, J., Olenius, T. and Vehkamäki, H.: Methane sulfonic acid-enhanced formation of molecular clusters of sulfuric acid and dimethylamine, Atmos. Chem. Phys., 14(22), 12023–12030, doi:10.5194/acp-14-12023-2014, 2014.

Bouwman, A. F., Lee, D. S., Asman, W. A. H., Dentener, F. J., Van Der Hoek, K. W., and Olivier, J. G. J.: A global high-resolution emission inventory for ammonia, Global Biogeochem. Cycles, 11(4), 561–587, 1997.

Breider, T. J., Mickley, L. J., Jacob, D. J., Wang, Q., Fisher, J. A., Chang, R. Y.-W., and Alexander, B.: Annual distributions and sources of Arctic aerosol components, aerosol optical depth, and aerosol absorption, J. Geophys. Res. Atmos., 119, 4107–4124, doi:10.1002/2013JD020996, 2014

Canagaratna, M. R., Jayne, J. T. J. T., Jimenez, J. L., Allan, J. D., Alfarra, M. R., Zhang, Q. Q., Onasch, T. B., Drewnick, F., Coe, H., Middlebrook, A. M., Delia, A., Williams, L. R., Trimborn, A. M., Northway, M. J., DeCarlo, P. F., Kolb, C. E., Davidovits, P. and Worsnop, D. R.: Chemical and microphysical characterization of ambient aerosols with the Aerodyne Aerosol Mass Spectrometer, Mass Spectrom. Rev., 26(2), 185–222, doi:10.1002/mas, 2007.

Dall´Osto, M., Simo, R., Harrison, R. M., Beddows, D. C. S., Saiz-Lopez, A., Lange, R., Skov, H., Nøjgaard, J. K., Nielsen, I. E. and Massling, A.: Abiotic and biotic sources influencing spring new particle formation in North East Greenland, Atmos. Environ., 190(July), 126–134, doi:10.1016/j.atmosenv.2018.07.019, 2018.

DeCarlo, P. F., Kimmel, J. R., Trimborn, A., Northway, M. J., Jayne, J. T., Aiken, A. C., Gonin, M., Fuhrer, K., Horvath, T., Docherty, K. S., Worsnop, D. R. and Jimenez, J. L.: Field-Deployable, High-Resolution, Time-of-Flight Aerosol Mass Spectrometer, Anal. Chem., 78(24), 8281–8289, doi:10.1021/ac061249n, 2006.

Centre on Emission Inventories and Projections (2013), EMEP emissions, Austrian Environment Agency. [Available at http://www.ceip.at/.]

Charlson, R. J., Lovelock, J. E., Andreae, M. O. and Warren, S. G.: Oceanic phytoplankton, atmospheric sulphur, cloud albedo and climate, Nature, 326, 655 [online] Available from: http://dx.doi.org/10.1038/326655a0, 1987.

Charlson, R. J., Schwartz, S. E., Hales, J. M., Cess, R. D., Coakley, J. A., Hansen, J. E., and Hofmann, D. J.: Climate forcing by anthropogenic aerosols, Science, 255, 423–430, 1992.

Chatfield, R. B. and Crutzen, P. J.: Are There Interactions of Iodine and Sulfur Species in Marine Air Photochemistry, J. Geophys. Res., 95(D13), 22319–22341, doi:10.1029/JD095iD13p22319, 1990.

Chen, H., Ezell, M. J., Arquero, K. D., Varner, M. E., Dawson, M. L., Gerber, R. B. and Finlayson-Pitts, B. J.: New particle formation and growth from methanesulfonic acid, trimethylamine and water, Phys. Chem. Chem. Phys. Phys. Chem. Chem. Phys, 17(17), 13699–13709, doi:10.1039/c5cp00838g, 2015.

Chen, H. and Finlayson-Pitts, B. J.: New Particle Formation from Methanesulfonic Acid and Amines/ Ammonia as a Function of Temperature, Environmental Science & Technology 2017 51 (1), 243-252, doi: 10.1021/acs.est.6b04173, 2017.

Chen, H., Hodshire, A. L., Ortega, J., Greenberg, J., Mcmurry, P. H., Carlton, A. G., Pierce, J. R., Hanson, D. R. and Smith, J. N.: Vertically resolved concentration and liquid water content of atmospheric nanoparticles at the US DOE Southern Great Plains site, Atmos. Chem. Phys, 185194, 311–326, doi:10.5194/acp-18-311-2018, 2018.

Chin, M., Jacob, D. J., Gardner, G. M., Foreman-fowler, M. S., Spiro, P. A. and Savoie, D. L.: A global three-dimensional model of tropospheric sulfate acid, , 101, doi:10.1029/ 96JD01221, 1996.

Clarke, A. D. and Kapustin, V. N.: A Pacific Aerosol Survey. Part I: A Decade of Data on Particle Production, Transport, Evolution, and Mixing in the Troposphere, J. Atmos. Sci., 59(3), 363–382, doi:10.1175/1520-0469(2002)059<0363:APASPI>2.0.CO;2, 2002.

Clegg, S. L., Brimblecombe, P., and Wexler, A. S.: Extended AIM Aerosol Thermodynamics model, available at: http://www.aim. env.uea.ac.uk/aim/aim.php, last access: March 2018.

Clegg, S. L., Pitzer, K. S., and Brimblecombe, P.: Thermodynamics of Multicomponent, Miscible, Ionic Solutions. 2. Mixtures Including Unsymmetrical Electrolytes, J. Phys. Chem., 96, 9470– 9479, doi:10.1021/j100202a074, 1992.
Clegg, S. L. and Seinfeld, J. H.: Thermodynamic models of aqueous solutions containing inorganic electrolytes and dicarboxylic acids at 298.15 K. 1. The acids as non-dissociating components, J. Phys. Chem. A, 110, 5692–5717, 2006a.

Clegg, S. L. and Seinfeld, J. H.: Thermodynamic models of aqueous solutions containing inorganic electrolytes and dicarboxylic acids at 298.15 K. 2. Systems including dissociation equilibria, J. Phys. Chem. A, 110, 5718–5734, 2006b.

Croft, B., Wentworth, G. R., Martin, R. V, Leaitch, W. R., Murphy, J. G., Murphy, B. N., Kodros, J. K., Abbatt, J. P. D. and Pierce, J. R.: Contribution of Arctic seabird-colony ammonia to atmospheric particles and cloud-albedo radiative effect, Nat. Commun., 7, 13444 [online] Available from: http://dx.doi.org/10.1038/ncomms13444, 2016.

D'Andrea, S. D., Häkkinen, S. A. K.,Westervelt, D. M., Kuang, C., Levin, E. J. T., Kanawade, V. P., Leaitch,W. R., Spracklen, D. V., Riipinen, I., and Pierce, J. R.: Understanding global secondary organic aerosol amount and size-resolved condensational behavior, Atmos. Chem. Phys., 13, 11519–11534, doi:10.5194/acp-13- 11519-2013, 2013.

D'Andrea, S. D., Acosta Navarro, J. C., Farina, S. C., Scott, C. E., Rap, A., Farmer, D. K., Spracklen, D. V., Riipinen, I., and Pierce, J. R.: Aerosol size distribution and radiative forcing response to anthropogenically driven historical changes in biogenic secondary organic aerosol formation, Atmos. Chem. Phys., 15, 2247–2268, doi:10.5194/acp-15-2247-2015, 2015.

de Leeuw, G., Andreas, E. L., Anguelova, M. D., Fairall, C. W., Lewis, E. R., O'Dowd, C., Schulz, M. and Schwartz, S. E.: Production flux of sea spray aerosol, Rev. Geophys., 49(2), n/a-n/a, doi:10.1029/2010RG000349, 2011.

Donahue, N. M., Robinson, A. L., Stanier, C. O. and Pandis, S. N.: Coupled Partitioning, Dilution, and Chemical Aging of Semivolatile Organics, Environ. Sci. Technol., 40(8), 2635–2643, doi:10.1021/es052297c, 2006.

Donahue, N. M., Trump, E. R., Pierce, J. R. and Riipinen, I.: Theoretical constraints on pure vapor-pressure driven condensation of organics to ultrafine particles, Geophys. Res. Lett., 38(16), n/a-n/a, doi:10.1029/2011GL048115, 2011.

Dunlea, E. J., DeCarlo, P. F., Aiken, A. C., Kimmel, J. R., Peltier, R. E., Weber, R. J., Tomlinson, J., Collins, D. R., Shinozuka, Y., McNaughton, C. S., Howell, S. G., Clarke, A. D., Emmons, L. K., Apel, E. C., Pfister, G. G., van Donkelaar, A., Martin, R. V., Millet, D. B., Heald, C. L., and Jimenez, J. L.: Evolution of Asian aerosols during transpacific transport in INTEX-B, Atmos. Chem. Phys., 9, 7257-7287, https://doi.org/10.5194/acp-9-7257-2009, 2009.

Eisele, F. L., and D. J. Tanner: Measurement of the gas phase concentration of H2SO4 and methane sulfonic acid and estimates of H2SO4 production and loss in the atmosphere, *J. Geophys. Res.*, 98(D5), 9001–9010, doi:10.1029/93JD00031, 1993.

Elliott, S.: Dependence of DMS global sea-air flux distribution on transfer velocity and concentration field type, J. Geophys. Res.- Biogeo., 114, 1–18, https://doi.org/10.1029/2008JG000710, 2009.

Erlick, C., Russell, L. M. and Ramaswamy, V.: A microphysics-based investigation of the radiative effects of aerosol-cloud interactions for two MAST Experiment case studies, J. Geophys. Res., 106(D1), 1249–1269, doi:10.1029/2000JD900567, 2001.

Facchini, M. C., Rinaldi, M., Decesari, S., Carbone, C., Finessi, E., Mircea, M., Fuzzi, S., Ceburnis, D., Flanagan, R., Nilsson, E. D., de Leeuw, G., Martino, M., Woeltjen, J., and O'Dowd, C. D.: Primary submicron marine aerosol dominated by insoluble organic colloids and aggregates, Geophys. Res. Lett., 35, L17814, https://doi.org/10.1029/2008GL034210, 2008.

Frossard, A. A., Russell, L. M., Burrows, S. M., Elliott, S. M., Bates, T. S. and Quinn, P. K.: Journal of Geophysical Research : Atmospheres mass in marine aerosol particles, , (Table 2), doi:10.1002/2014JD021913.Received, 2014.

Gordon, H., Kirkby, J., Baltensperger, U., Bianchi, F., Breitenlechner, M., Curtius, J., Dias, A., Dommen, J., Donahue, N. M., Dunne, E. M., Duplissy, J., Ehrhart, S., Flagan, R. C., Frege, C., Fuchs, C., Hansel, A., Hoyle, C. R., Kulmala, M., Kürten, A., Lehtipalo, K., Makhmutov, V., Molteni, U., Rissanen, M. P., Stozkhov, Y., Tröstl, J., Tsagkogeorgas, G., Wagner, R., Williamson, C., Wimmer, D., Winkler, P. M., Yan, C. and Carslaw, K. S.: Causes and importance of new particle formation in the present-day and preindustrial atmospheres, J. Geophys. Res. Atmos., 122(16), 8739–8760, doi:10.1002/2017JD026844, 2017.

Anna Lily Hodshire 2/13/2019 4:50 PM
Formatted: Left

Anna Lily Hodshire 2/13/2019 4:50 PM
Formatted: Font:(Default) Arial, 11 pt, Font color: Black

Haynes, W.: CRC Handbook of Chemistry and Physics, 98th Edition., CRC Press, Boca Raton, 2017.

Seinfeld, J. H. and Pandis, S. N.: Atmospheric Chemistry and Physics, 2nd ed., John Wiley and Sons, New York, 2006.

Heald, C. L., Ridley, D. A., Kroll, J. H., Barrett, S. R. H., Cady- Pereira, K. E., Alvarado, M. J., and Holmes, C. D.: Contrasting the direct radiative effect and direct radiative forcing of aerosols, Atmos. Chem. Phys., 14, 5513–5527, doi:10.5194/acp-14-5513- 2014, 2014.

Heintzenberg, J., Covert, D. C. and Van Dingenen, R.: Size distribution and chemical composition of marine aerosols: a compilation and review, Tellus, 52, 1104–1122, doi:10.1034/j.1600-0889.2000.00136.x, 2000.

Hodshire, A. L., Lawler, M. J., Zhao, J., Ortega, J., Jen, C., Yli-Juuti, T., Brewer, J. F., Kodros, J. K., Barsanti, K. C., Hanson, D. R., McMurry, P. H., Smith, J. N. and Pierce, J. R.: Analysis of multiple new-particle growth pathways observed at the US DOE Southern Great Plains field site, Atmos. Chem. Phys. Discuss., (March), 1–49, doi:10.5194/acp-2016-157, 2016.

Hoffmann, E. H., Tilgner, A., Schrödner, R., Bräuer, P., Wolke, R. and Herrmann, H.: An advanced modeling study on the impacts and atmospheric implications of multiphase dimethyl sulfide chemistry, Proc. Natl. Acad. Sci., 113(42), 11776–11781, doi:10.1073/pnas.1606320113, 2016.

Huang, L., Jiang, J. H., Tackett, J. L., Su, H. and Fu, R. .: Seasonal and diurnal variations of aerosol extinction profile and type distribution from CALIPSO 5□year observations, J. Geophys. Res. Atmos., 118(10), 4572–4596, doi:10.1002/jgrd.50407, 2013.

Iacono, M. J., Delamere, J. S., Mlawer, E. J., Shephard, M. W., Clough, S. A., and Collins, W. D.: Radiative forcing by long-lived greenhouse gases: Calculations with the AER radiative transfer models, J. Geophys. Res., 113, D13103, doi:10.1029/2008JD009944, 2008.

Jaeglé, L., Quinn, P. K., Bates, T. S., Alexander, B., and Lin, J.-T.: Global distribution of sea salt aerosols: new constraints from in situ and remote sensing observations, Atmos. Chem. Phys., 11, 3137–3157, doi:10.5194/acp-11-3137-2011, 2011.

Janssens-Maenhout, A., Petrescu, A., Muntean, M., and Blujdea,V.: Verifying Greenhouse Gas Emissions: Methods to Support International Climate Agreements, The National Academies Press, Washington, DC, available at: http://www.nap.edu/openbook. php?record_id=12883 (last access: 17 March 2014), 2010.

Jung, J., Fountoukis, C., Adams, P. J., and Pandis, S. N.: Simulation of in situ ultrafine particle formation in the eastern United States using PMCAMx-UF, J. Geophys. Res., 115, D03203, doi:10.1029/2009JD012313, 2010.

Kerminen, V. M., Anttila, T., Lehtinen, K. E. J., and Kulmala, M.: Parameterization for atmospheric new-particle formation: Application to a system involving sulfuric acid and condensable water soluble organic vapors, Aerosol Sci. Technol., 38, 1001–1008, 2004.

Kettle, A. J., Amouroux, D., Andreae, T. W., Bates, T. S., Berresheim, H., Bingemer, H., Boniforti, R., Helas, G., Leck, C., Maspero, M., Matrai, P., McTaggart, A. R., Mihalopoulos, N., Nguyen, B. C., Novo, A., Putaud, J. P., Rapsomanikis, S., Roberts, G., Schebeske, G., Sharma, S., Simó, R., Staubes, R., Turner, S. and Uher, G.: A global database of sea surface dimethyl sulfide (DMS) measurements and a simple model to predict sea surface DMS as a function of latitude, longitude, and month, Glob. Biogeochem. Cycles, 13(2), 399–444, 1999.

Kettle, A. J., and Andreae, M. O.: Flux of dimethylsulfide from the oceans: A comparison of updated data sets and flux models, *J. Geophys. Res.*, 105(D22), 26793–26808, doi:10.1029/2000JD900252, 2000.

Kimmel, J. R., Farmer, D. K., Cubison, M. J., Sueper, D., Tanner, C., Nemitz, E., Worsnop, D. R., Gonin, M. and Jimenez, J. L.: Real-time aerosol mass spectrometry with millisecond resolution, Int. J. Mass Spectrom., 303(1), 15–26, doi:10.1016/j.ijms.2010.12.004, 2011.

Kodros, J. K., Cucinotta, R., Ridley, D. A., Wiedinmyer, C. and Pierce, J. R.: The aerosol radiative effects of uncontrolled combustion of domestic waste, Atmos. Chem. Phys, 16, 6771–6784, doi:10.5194/acp-16-6771-2016, 2016.

Kodros, J. K. and Pierce, J. R.: Important global and regional differences in aerosol cloud-albedo effect estimates between simulations with and without prognostic aerosol microphysics, J. Geophys. Res. Atmos., 122(7), 4003–4018, doi:10.1002/2016JD025886, 2017.

Kodros, J. K., Hanna, S., Bertram, A., Leaitch, W. R., Schulz, H., Herber, A., Zanatta, M., Burkart, J., Willis, M., Abbatt, J. P. D., and Pierce, J. R.: Size-resolved mixing state of black carbon in the Canadian high Arctic and implications for simulated direct radiative effect, Atmos. Chem. Phys., https://doi.org/10.5194/acp-18-11345-2018, 2018.

Koepke, P., Hess, M., Schult, I., and Shettle, E.: Global aerosol data set, MPI Meteorol. Hamburg Rep. 243, 44 pp., Max-Planck-Institut für Meteorologie, Hamburg, Germany, 1997.

Korhonen, H., Carslaw, K. S., Spracklen, D. V, Mann, G. W. and Woodhouse, M. T.: Influence of oceanic dimethyl sulfide emissions on cloud condensation nuclei concentrations and seasonality over the remote Southern Hemisphere oceans: A global model study, J. Geophys. Res. Atmos., 113(D15), n/a-n/a, doi:10.1029/2007JD009718, 2008.

Kulmala, M., Pirjola, L. and Makela, J. M.: Stable sulphate clusters as a source of new atmospheric particles, Nature, 404(6773), 66–69, doi:10.1038/35003550, 2000.

Kwong, K. C., Chim, M. M., Hoffmann, E. H., Tilgner, A., Herrmann, H., Davies, J., Wilson, K. R. and Chan, M.: Chemical Transformation of Methanesulfonic Acid and Sodium Methanesulfonate through Heterogeneous OH Oxidation, ACS Earth Sp. Chem., doi:10.1021/acsearthspacechem.8b00072, 2018.

Lana, A., Bell, T. G., Simó, R., Vallina, S. M., Ballabrera-Poy, J., Kettle, A. J., Dachs, J., Bopp, L., Saltzman, E. S., Stefels, J., Johnson, J. E. and Liss, P. S.: An updated climatology of surface dimethlysulfide concentrations and emission fluxes in the global ocean, Global Biogeochem. Cycles, 25(1), 1–17, doi:10.1029/2010GB003850, 2011.

Lee, Y. H. and Adams, P. J.: A Fast and Efficient Version of the TwO-Moment Aerosol Sectional (TOMAS) Global Aerosol Microphysics Model, Aerosol Sci. Technol., 46(6), 678–689, doi:10.1080/02786826.2011.643259, 2012.

Lee, Y.H., Pierce, J.R., Adams, P.J.: Representation of nucleation mode microphysics in global aerosol microphysics models, Geosci. Model Dev., 6, 1221-1232, doi:10.5194/gmd-6-1221-2013, 2013.

Legrand, M., Preunkert, S., Weller, R., Zipf, L., Elsässer, C., Merchel, S., Rugel, G., and Wagenbach, D.: Year-round record of bulk and size-segregated aerosol composition in central Antarctica (Concordia site) – Part 2: Biogenic sulfur (sulfate and methanesulfonate) aerosol, Atmos. Chem. Phys., 17, 14055-14073, https://doi.org/10.5194/acp-17-14055-2017, 2017.

Li, M., Zhang, Q., Kurokawa, J.-I., Woo, J.-H., He, K., Lu, Z., Ohara, T., Song, Y., Streets, D. G., Carmichael, G. R., Cheng, Y., Hong, C., Huo, H., Jiang, X., Kang, S., Liu, F., Su, H., and Zheng, B.: MIX: a mosaic Asian anthropogenic emission inventory under the international collaboration framework of the MICS-Asia and HTAP, Atmos. Chem. Phys., 17, 935-963, https://doi.org/10.5194/acp-17-935-2017, 2017.

Ma, X. and Yu, F.: Seasonal and spatial variations of global aerosol optical depth: multi-year modelling with GEOS-Chem-APM and comparisons with multiple platform observations, Tellus B: Chem. Phys. Met., 67:1, 25115, DOI: 10.3402/tellusb.v67.2511, 2015.

Maudlin, R. L. III, Cantrell, C. A., Zondlo, M., Kosciuch, E., Eisele, F. L., Chen, G., Davis, D., Weber, R., Crawford, J., Blake, D., Bandy, A., and Thornton, D. : Highlights of OH, H2SO4, and methane sulfonic acid measurements made aboard the NASA P□3B during Transport and Chemical Evolution over the Pacific, J. Geophys. Res. Atmos., 108(D20), doi:10.1029/2003JD003410, 2003.

Marti, J. J., Jefferson, A., Cai, X. P., Richert, C., McMurry, P. H.,
and Eisele, F.: H2SO4 vapor pressure of sulfuric acid and ammonium sulfate solutions, J. Geophys. Res.-Atmos., 102, 3725–3735, doi:10.1029/96JD03064, 1997.

McGrath, M. J., Olenius, T., Ortega, I. K., Loukonen, V., Paasonen, P., Kurtén, T., Kulmala, M., and Vehkamäki, H.: Atmospheric Cluster Dynamics Code: a flexible method for solution of the birth-death equations, Atmos. Chem. Phys., 12, 2345–2355, doi:10.5194/acp-12-2345-2012, 2012.

Mungall, E. L., Wong, J. P. S. and Abbatt, J. P. D.: Heterogeneous Oxidation of Particulate Methanesulfonic Acid by the Hydroxyl Radical: Kinetics and Atmospheric Implications, ACS Earth Sp. Chem., 2, 1, 48-55, doi:10.1021/acsearthspacechem.7b00114, 2017.

Murphy, B. N., Donahue, N. M., Robinson, A. L. and Pandis, S. N.: A naming convention for atmospheric organic aerosol, Atmos. Chem. Phys., 14(11), 5825–5839, doi:10.5194/acp-14-5825-2014, 2014.

Napari, I., Noppel, M., Vehkamäki, H., and Kulmala, M.:
Parametrization of ternary nucleation rates for H2SO4-NH3-H2O vapors, J. Geophys. Res.-Atmos., 107,AAC 6–1–AAC 6–6, doi:10.1029/2002JD002132, 2002.l

Nault, B. A., Campuzano-Jost, P., Day, D. A., Schroder, J. C., Anderson, B., Beyersdorf, A. J., Blake, D. R., Brune, W. H., Choi, Y., Corr, C. A., de Gouw, J. A., Dibb, J., DiGangi, J. P., Diskin, G. S., Fried, A., Huey, L. G., Kim, M. J., Knote, C. J., Lamb, K. D., Lee, T., Park, T., Pusede, S. E., Scheuer, E., Thornhill, K. L., Woo, J.-H., and Jimenez, J. L.: Secondary Organic Aerosol Production from Local Emissions Dominates the Organic Aerosol Budget over Seoul, South Korea, during KORUS-AQ, Atmos. Chem. Phys. Discuss., https://doi.org/10.5194/acp-2018-838, in review, 2018.

O'Dowd, C. D., Facchini, M. C., Cavalli, F., Ceburnis, D., Mircea, M., Decesari, S., Fuzzi, S., Yoon, Y. J. and Putaud, J.-P.: Biogenically driven organic contribution to marine aerosol, Nature, 431(7009), 676–680, doi:10.1038/nature02959, 2004.

Anna Lily Hodshire 2/12/2019 11:39 PM
Deleted: -

O'Dowd, C. D. and de Leeuw, G.: Marine aerosol production: a review of the current knowledge., Philos. Trans. A. Math. Phys. Eng. Sci., 365(1856), 1753–74, doi:10.1098/rsta.2007.2043, 2007.

Olenius, T., Kupiainen-Määttä, O., Ortega, I., Kurtén, T., and Vehkamäki, H.: Free energy barrier in the growth of sulfuric acid–ammonia and sulfuric acid–dimethylamine clusters, J. Chem. Phys., 139, 084312, doi10.1063/1.4819024, 2013.

Paatero, P. and Tapper, U.: Positive Matrix Factorization - A Nonnegative Factor Model With Optimal Utilization of Error-Estimates of Data Values, Environmetrics, 5(2), 111–126, 1994.

Pandis, S. N., Baltensperger, U., Wolfenbarger, J. K. and Seinfeld, J. H.: Inversion of aerosol data from the epiphaniometer, J. Aerosol Sci., 22(4), 417–428, doi:https://doi.org/10.1016/0021-8502(91)90002-Y, 1991.

Petters, M. D. and Kreidenweis, S. M.: A single parameter representation of hygroscopic growth and cloud condensation nucleus activity, Atmos. Chem. Phys., 7, 1961–1971, doi:10.5194/acp-7- 1961-2007, 2007.

Pierce, J. R. and Adams, P. J.: Uncertainty in global CCN concentrations from uncertain aerosol nucleation and primary emission rates, Atmos. Chem. Phys., 9, 1339–1356, doi:10.5194/acp-9- 1339-2009, 2009a.

Pierce, J.R., Adams, P.J., A computationally efficient aerosol nucleation/condensation method: Pseudo-steady-state sulfuric acid, Aerosol Science and Technology, 43, 216-226, 2009b.

Pierce, J. R., Riipinen, I., Kulmala, M., Ehn, M., Petäjä, T., Junninen, H., Worsnop, D. R. and Donahue, N. M.: Quantification of the volatility of secondary organic compounds in ultrafine particles during nucleation events, Atmos. Chem. Phys., 11(17), 9019–9036, doi:10.5194/acp-11-9019-2011, 2011.

Pierce, J. R., Evans, M. J., Scott, C. E., D'Andrea, S. D., Farmer, D. K., Swietlicki, E., and Spracklen, D. V.: Weak global sensitivity of cloud condensation nuclei and the aerosol indirect effect to Criegee + SO2 chemistry, Atmos. Chem. Phys., 13, 3163-3176, https://doi.org/10.5194/acp-13-3163-2013, 2013.

Phinney, L., Richard Leaitch, W., Lohmann, U., Boudries, H., Worsnop, D. R., Jayne, J. T., Toom-Sauntry, D., Wadleigh, M., Sharma, S., Shantz, N., Leaitch, W. R., Lohmann, U., Boudries, H., Worsnop, D. R., Jayne, J. T., Toom-Sauntry, D., Wadleigh, M., Sharma, S., Shantz, N., Richard Leaitch, W., Lohmann, U., Boudries, H., Worsnop, D. R., Jayne, J. T., Toom-Sauntry, D., Wadleigh, M., Sharma, S., Shantz, N., Leaitch, W. R., Lohmann, U., Boudries, H., Worsnop, D. R., Jayne, J. T., Toom-Sauntry, D., Wadleigh, M., Sharma, S. and Shantz, N.: Characterization of the aerosol over the sub-arctic north east

Pacific Ocean, Deep. Res. II-Topical Stud. Oceanogr., 53(20–22), 2410–2433, doi:10.1016/j.dsr2.2006.05.044|ISSN 0967-0645, 2006.

Preunkert, S., Jourdain, B., Legrand, M., Udisti, R., Becagli, S., and Cerri, O.: Seasonality of sulfur species (dimethyl sulfide, sulfate, and methanesulfonate) in Antarctica: Inland versus coastal regions, J. Geophys. Res., 113, D15302, https://doi.org/10.1029/2008JD009937, 2008.

Quinn, P. K., Collins, D. B., Grassian, V. H., Prather, K. A. and Bates, T. S.: Chemistry and Related Properties of Freshly Emitted Sea Spray Aerosol, Chem. Rev., 115(10), 4383–4399, doi:10.1021/cr500713g, 2015.

Rap, A., Scott, C. E., Spracklen, D. V., Bellouin, N., Forster, P. M., Carslaw, K. S., Schmidt, A., and Mann, G.: Natural aerosol direct and indirect radiative effects, Geophys. Res. Lett., 40, 3297– 3301, doi:10.1002/grl.50441, 2013.

Reddington, C. L., Carslaw, K. S., Stier, P., Schutgens, N., Coe, H., Liu, D., Allan, J., Browse, J., Pringle, K. J., Lee, L. A., Yoshioka, M., Johnson, J. S., Regayre, L. A., Spracklen, D. V., Mann, G. W., Clarke, A., Hermann, M., Henning, S., Wex, H., Kristensen, T. B., Leaitch, W. R., Pöschl, U., Rose, D., Andreae, M. O., Schmale, J., Kondo, Y., Oshima, N., Schwarz, J. P., Nenes, A., Anderson, B., Roberts, G. C., Snider, J. R., Leck, C., Quinn, P. K., Chi, X., Ding, A., Jimenez, J. L. and Zhang, Q.: The global aerosol synthesis and science project (GASSP): Measurements and modeling to reduce uncertainty, Bull. Am. Meteorol. Soc., 98(9), 1857–1877, doi:10.1175/BAMS-D-15-00317.1, 2017.

Regayre, L. A., Johnson, J. S., Yoshioka, M., Pringle, K. J., Sexton, D. M. H., Booth, B. B. B., Lee, L. A., Bellouin, N., and Carslaw, K. S.: Aerosol and physical atmosphere model parameters are both important sources of uncertainty in aerosol ERF, Atmos. Chem. Phys., 18, 9975-10006, https://doi.org/10.5194/acp-18-9975-2018, 2018.

Riipinen, I., Pierce, J. R., Yli-Juuti, T., Nieminen, T., Häkkinen, S., Ehn, M., Junninen, H., Lehtipalo, K., Petäjä, T., Slowik, J., Chang, R., Shantz, N. C., Abbatt, J., Leaitch, W. R., Kerminen, V.-M., Worsnop, D. R., Pandis, S. N., Donahue, N. M. and Kulmala, M.: Organic condensation: a vital link connecting aerosol formation to cloud condensation nuclei (CCN) concentrations, Atmos. Chem. Phys., 11(8), 3865–3878, doi:10.5194/acp-11-3865-2011, 2011.

Royer, S. J., Mahajan, A. S., Galí, M., Saltzman, E., and Simõ, R.: Small-scale variability patterns of DMS and phytoplankton in surface waters of the tropical and subtropical Atlantic, Indian, and Pacific Oceans, Geophys. Res. Lett., 42, 475–483, https://doi.org/10.1002/2014GL062543, 2015.

Anna Lily Hodshire 2/13/2019 4:51 PM
Formatted: Font color: Blue

Anna Lily Hodshire 2/13/2019 4:51 PM
Formatted: Left

Schroder, J. C., Campuzano□Jost, P., Day, D. A., Shah, V., Larson, K., Sommers, J. M., Sullivan, A. P. Campos, T. Reeves, J. M. Hills, A., Hornbrook, R. S., Blake, N. J., Scheuer, E., Guo, H., Fibiger, D. L. McDuffie, E. E., Hayes, P. L., Weber, R. J., Dibb, J. E. Apel, E. C., Jaeglé, L. Brown, S. S. Thornton, J. A. and Jimenez, J. L. Sources and secondary production of organic aerosols in the northeastern United States during WINTER. Journal of Geophysical Research: Atmospheres, 123, 7771–7796. doi: 10.1029/2018JD028475, 2018

Scott, C. E., Rap, A., Spracklen, D. V., Forster, P. M., Carslaw, K. S., Mann, G. W., Pringle, K. J., Kivekäs, N., Kulmala, M., Lihavainen, H., and Tunved, P.: The direct and indirect radiative effects of biogenic secondary organic aerosol, Atmos. Chem. Phys., 14, 447–470, doi:10.5194/acp-14-447-2014, 2014.

Seinfeld, J. H. and Pandis, S. N.: Atmospheric Chemistry and Physics, 2nd ed., John Wiley and Sons, New York, 2006.

Sheng, J. X., Weisenstein, D. K., Luo, B. P., Rozanov, E., Stenke, A., Anet, J., Bingemer, H., and Peter, T.: Global atmospheric sulfur budget under volcanically quiescent conditions: Aerosol-chemistry-climate model predictions and validation, J. Geophys. Res.-Atmos., 120, 256–276, https://doi.org/10.1002/2014JD021985, 2015.

Sørensen, S., Falbe□Hansen, H., Mangoni, M., Hjorth, J., and. Jensen, N. R: Observation of DMSO and CH3S(O)OH from the gas phase reaction between DMS and OH, J. Atmos. Chem., 24(3), 299–315, doi:10.1007/BF00210288, 1996.

Spracklen, D. V., Carslaw, K. S., Pöschl, U., Rap, A., and Forster, P. M.: Global cloud condensation nuclei influenced by carbonaceous combustion aerosol, Atmos. Chem. Phys., 11, 9067–9087, doi:10.5194/acp-11-9067-2011, 2011.

Streets, D. G., Bond., T. C., Carmichael., G. R., Fernandes, S. D., Fu, Q., He, D., Klimont, Z., Nelson, S. M., Tsai, N. Y., Wang, M. Q., Woo, J.-H., Yarber, K. F.: An inventory of gaseous and primary aerosol emissions in Asia in the year 2000, J. Geophys. Res., 108(D21), 8809, doi:10.1029/2002JD003093, 2003.

Tesdal, J. E., Christian, J. R., Monahan, A. H., and Von Salzen, K.: Evaluation of diverse approaches for estimating sea-surface DMS concentration and air-sea exchange at global scale, Environ. Chem., 13, 390–412, https://doi.org/10.1071/EN14255, 2016.

Textor, C., Schulz, M., Guibert, S., Kinne, S., Balkanski, Y., Bauer, S., Berntsen, T., Berglen, T., Boucher, O., Chin, M., Dentener, F., Diehl, T., Easter, R., Feichter, H., Fillmore, D., Ghan, S., Ginoux, P., Gong, S., Grini, A., Hendricks, J., Horowitz, L., Huang, P., Isaksen, I., Iversen, I., Kloster, S., Koch, D., Kirkevåg, A., Kristjansson, J. E., Krol, M., Lauer, A., Lamarque, J. F., Liu, X., Montanaro, V., Myhre, G., Penner, J., Pitari, G., Reddy, S., Seland, Ø., Stier, P., Takemura, T., and

Tie, X.: Analysis and quantification of the diversities of aerosol life cycles within AeroCom, Atmos. Chem. Phys., 6, 1777-1813, https://doi.org/10.5194/acp-6-1777-2006, 2006.

Twomey, S.: Pollution and the planetary albedo, Atmos. Environ., 8, 1251–1256, 1974.

Ulbrich, I. M., Canagaratna, M. R., Zhang, Q., Worsnop, D. R. and Jimenez, J. L.: Interpretation of organic components from Positive Matrix Factorization of aerosol mass spectrometric data, Atmos. Chem. Phys., 9(9), 2891–2918, doi:10.5194/acp-9-2891-2009, 2009.

Vehkamäki, H.: An improved parameterization for sulfuric acid– water nucleation rates for tropospheric and stratospheric conditions, J. Geophys. Res., 107, 4622, doi:10.1029/2002JD002184, 2002.

Wang, X., Deane, G. B., Moore, K. A., Ryder, O. S., Stokes, M. D., Beall, C. M., Collins, D. B., Santander, M. V, Burrows, S. M., Sultana, C. M. and Prather, K. A.: The role of jet and film drops in controlling the mixing state of submicron sea spray aerosol particles, Proc. Natl. Acad. Sci., 114(27), 6978 LP-6983 [online] Available from: http://www.pnas.org/content/114/27/6978.abstract, 2017.

Westervelt, D. M., Pierce, J. R., Riipinen, I., Trivitayanurak, W., Hamed, A., Kulmala, M., Laaksonen, A., Decesari, S., and Adams, P. J.: Formation and growth of nucleated particles into cloud condensation nuclei: model-measurement comparison, Atmos. Chem. Phys., 13, 7645–7663, doi:10.5194/acp-13-7645- 2013, 2013.

Wexler, A. S. and Clegg, S. L.: Atmospheric aerosol models for
systems including the ions H+, NH4+, Na+, SO42−, NO3−, Cl−, Br−, and H2O, J. Geophys. Res.-Atmos., 107, ACH-14-1–ACH-14-14, doi:10.1029/2001JD000451, 2002.

Wiedinmyer, C., Akagi, S. K., Yokelson, R. J., Emmons, L. K., Al-Saadi, J. A., Orlando, J. J., and Soja, A. J.: The Fire INventory from NCAR (FINN): a high resolution global model to estimate the emissions from open burning, Geosci. Model Dev., 4, 625-641, https://doi.org/10.5194/gmd-4-625-2011, 2011.

Wilson, C. and Hirst, D. M.: Kinetics of gas phase oxidation of reduced sulfur compounds, Prog. React. Kinet., 21(2–3), 69–132, 1996.

Woodhouse, M. T., Carslaw, K. S., Mann, G. W., Vallina, S. M., Vogt, M., Halloran, P. R., and Boucher, O.: Low sensitivity of cloud condensation nuclei to changes in the sea-air flux of dimethyl-sulphide, Atmos. Chem. Phys., 10, 7545–7559, https://doi.org/10.5194/acp-10-7545-2010, 2010.

Woodhouse, M. T., Mann, G. W., Carslaw, K. S., and Boucher, O.: Sensitivity of cloud condensation nuclei to regional changes in dimethyl-sulphide emissions, Atmos. Chem. Phys., 13, 2723-2733, https://doi.org/10.5194/acp-13-2723-2013, 2013.

Wofsy, S.C., S. Afshar, H.M. Allen, E. Apel, E.C. Asher, B. Barletta, J. Bent, H. Bian, B.C. Biggs, D.R. Blake, N. Blake, I. Bourgeois, C.A. Brock, W.H. Brune, J.W. Budney, T.P. Bui, A. Butler, P. Campuzano-Jost, C.S. Chang, M. Chin, R. Commane, G. Correa, J.D. Crounse, P. D. Cullis, B.C. Daube, D.A. Day, J.M. Dean-Day, J.E. Dibb, J.P. DiGangi, G.S. Diskin, M. Dollner, J.W. Elkins, F. Erdesz, A.M. Fiore, C.M. Flynn, K. Froyd, D.W. Gesler, S.R. Hall, T.F. Hanisco, R.A. Hannun, A.J. Hills, E.J. Hintsa, A. Hoffman, R.S. Hornbrook, L.G. Huey, S. Hughes, J.L. Jimenez, B.J. Johnson, J.M. Katich, R. Keeling, M.J. Kim, A. Kupc, L.R. Lait, J.-F. Lamarque, J. Liu, K. McKain, R.J. Mclaughlin, S. Meinardi, D.O. Miller, S.A. Montzka, F.L. Moore, E.J. Morgan, D.M. Murphy, L.T. Murray, B.A. Nault, J.A. Neuman, P.A. Newman, J.M. Nicely, X. Pan, W. Paplawsky, J. Peischl, M.J. Prather, D.J. Price, E. Ray, J.M. Reeves, M. Richardson, A.W. Rollins, K.H. Rosenlof, T.B. Ryerson, E. Scheuer, G.P. Schill, J.C. Schroder, J.P. Schwarz, J.M. St.Clair, S.D. Steenrod, B.B. Stephens, S.A. Strode, C. Sweeney, D. Tanner, A.P. Teng, A.B. Thames, C.R. Thompson, K. Ullmann, P.R. Veres, N. Vieznor, N.L. Wagner, A. Watt, R. Weber, B. Weinzierl, P. Wennberg, C.J. Williamson, J.C. Wilson, G.M. Wolfe, C.T. Woods, and L.H. Zeng. 2018. ATom: Merged Atmospheric Chemistry, Trace Gases, and Aerosols. ORNL DAAC, Oak Ridge, Tennessee, USA. https://doi.org/10.3334/ORNLDAAC/1581

Xausa, F., Paasonen, P., Makkonen, R., Arshinov, M., Ding, A., Denier Van Der Gon, H., Kerminen, V.-M., and Kulmala, M.: Advancing global aerosol simulations with size-segregated anthropogenic particle number emissions, Atmos. Chem. Phys., 18, 10039-10054, https://doi.org/10.5194/acp-18-10039-2018, 2018.

Yli-Juuti, T., Barsanti, K., Hildebrandt Ruiz, L., Kieloaho, A.-J., Makkonen, U., Petäjä, T., Ruuskanen, T., Kulmala, M. and Riipinen, I.: Model for acid-base chemistry in nanoparticle growth (MABNAG), Atmos. Chem. Phys., 13(24), 12507–12524, doi:10.5194/acp-13-12507-2013, 2013.

Yin, F., Grosjean, D., Flagan, R.C., and Seinfeld, J. H.: Photooxidation of dimethyl sulfide and dimethyl disulfide. II: Mechanism evaluation, J. Atmos. Chem., 11(4), 365–399, doi:10.1007/BF00053781, 1990.

Zender, C. S.: Mineral Dust Entrainment and Deposition (DEAD) model: Description and 1990s dust climatology, J. Geophys. Res., 108, 4416, doi:10.1029/2002JD002775, 2003.

Zhang, X., Pandis, S. N. and Seinfeld, J. H.: Diffusion-Limited Versus Quasi-Equilibrium Aerosol Growth, Aerosol Sci. Technol., 46(8), 874–885, doi:10.1080/02786826.2012.679344, 2012.

Zorn, S. R., Drewnick, F., Schott, M., Hoffmann, T. and Borrmann, S.: Characterization of the South Atlantic marine boundary layer aerosol using an aerodyne aerosol mass spectrometer, Atmos. Chem. Phys., 8(16), 4711–4728, doi:10.5194/acp-8-4711-2008, 2008.

Tables

Table 1. Fit coefficients for the MSA volatility parameterization equation.

Variable	Value
a	2.52×10^{2}
b	6.19×10^{-1}
c	3.49×10^{-2}
d	5.6×10^{-4}
e	3.32×10^{-6}

Table 2. Description of simulations.

Simulation	Description
DEFAULT_NoMSA	Default model simulation: MSA does not contribute to the particle size distribution in GEOS-Chem-TOMAS (GC-TOMAS). The default GC-TOMAS v10.01 DMS emissions are used, and SO_2, sulfate, and sulfuric acid from DMS does influence the particle size distribution.
PARAM_NoNuc (NoNuc = does not nucleate particles)	Parameterization for MSA from E-AIM simulations: volatility is based on NH_3, T and RH. MSA can act as non-volatile and non-nucleating, semivolatile, or volatile (no condensation).
ELVOC_NoNuc	MSA is assumed to be non-volatile and condenses proportionally to the surface area distribution.
SVOC_NoNuc	MSA is assumed to be semivolatile and condenses proportional to the mass distribution.
ELVOC_Nuc	Like ELVOC_NoNuc, but MSA acts like sulfuric acid in nucleation.

NoDMS_NoMSA	All DMS emissions are turned off in the model; all other parameters are the same as the DEFAULT_NoMSA case.
DEFAULT_NoMSA_Lana	Default case using the Lana et al. (2010) DMS emissions inventory.
DEFAULT_NoMSA_2xDMS	Default case with global DMS emissions increased by a factor of two.
PARAM_NoNuc_Lana	Use the settings of PARAM_NoNuc with the Lana et al. (2010) DMS emissions inventory.
PARAM_NoNuc_2xDMS	Increase DMS emissions by a factor of two, using the settings of PARAM_NoNuc

Figures

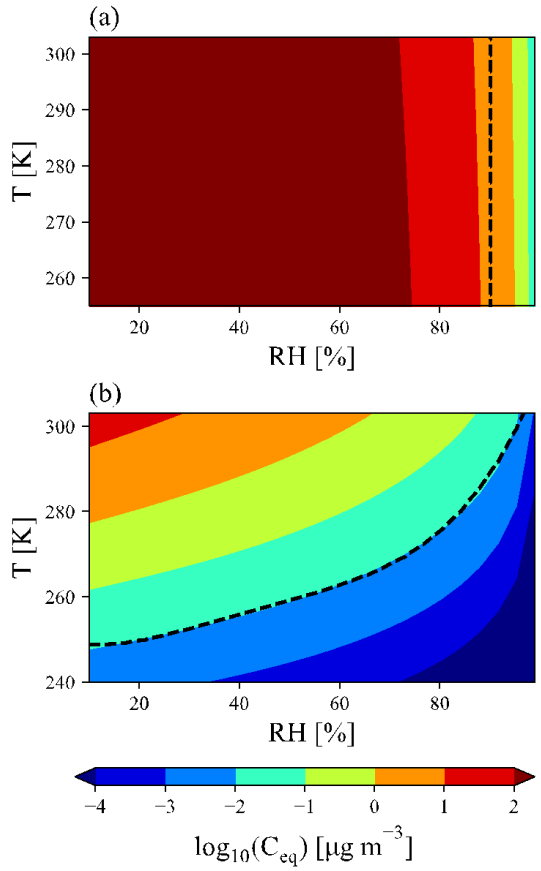

Figure 1. E-AIM prediction of MSA equilibrium vapor pressure above the particle mixture (C_{eq}) under conditions with (a) no free ammonia and (b) high free ammonia (3 times as many moles of ammonia as MSA). (a) The dashed line at 90% RH indicates the cut-off for representing MSA as a VOC-like (left of the line) or an SVOC-like (right of the line) species. (b) The dashed line is described by Eq. 1 in the text. Above the dashed line, MSA is treated as an SVOC-like species; below the dashed line, MSA is treated as an ELVOC-like species.

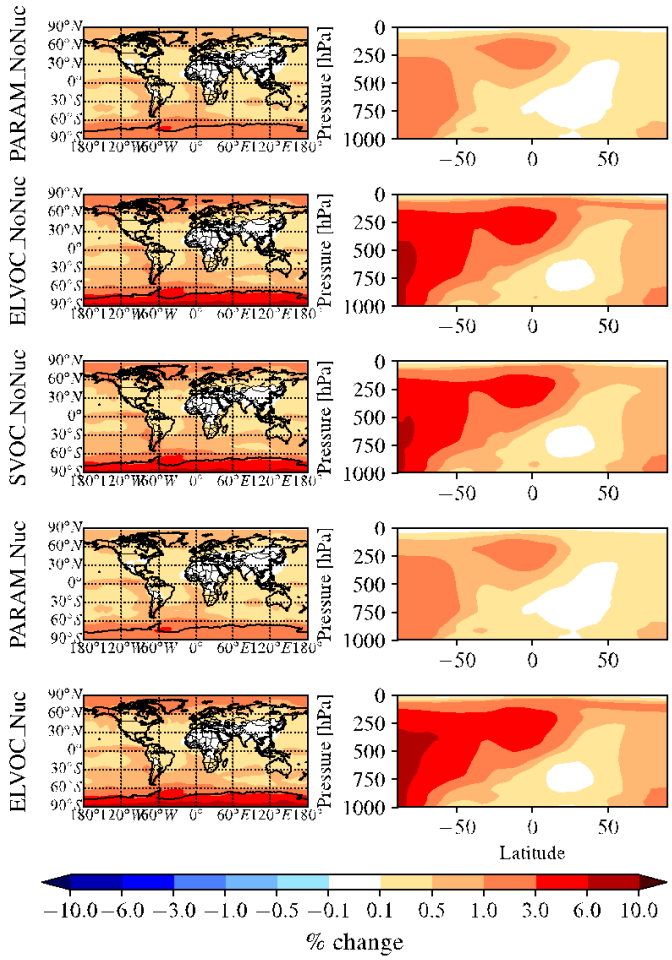

Figure 2. Global annual mean percent change in submicron aerosol mass due to the addition of MSA at 900 hPa (first column) and global zonal annual mean percent change (second column) between DEFAULT_NoMSA and PARAM_NoNuc (first row), ELVOC_NoNuc (second row), SVOC_Nuc (third row), PARAM_Nuc (fourth row), and ELVOC_Nuc (fifth row) (warm colors indicate an increase in submicron mass as compared to DEFAULT_NoMSA).

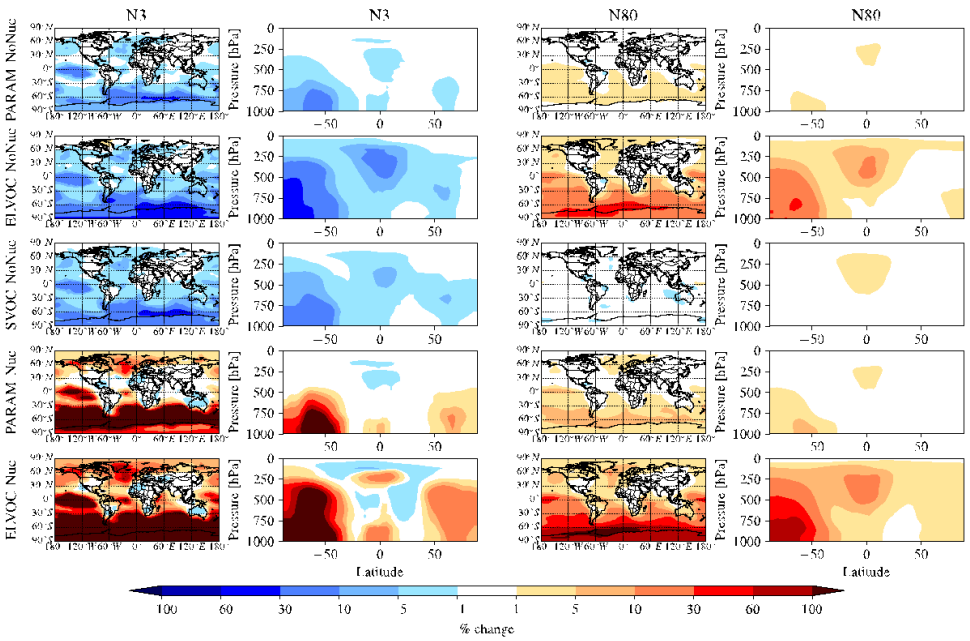

Figure 3. Global annual mean percent change in N3 and N80 at 900 hPa (first and third columns) and global zonal annual mean percent change (second and fourth columns) between DEFAULT_NoMSA and PARAM_NoNuc (first row), ELVOC_NoNuc (second row), SVOC_Nuc (third row), PARAM_Nuc (fourth row), and ELVOC_Nuc (fifth row) (warm colors indicate an increase in N3/N80 as compared to DEFAULT_NoMSA). First and second column: N3 (the number concentration of particles with diameters larger than 3 nm). Third and fourth column: N80.

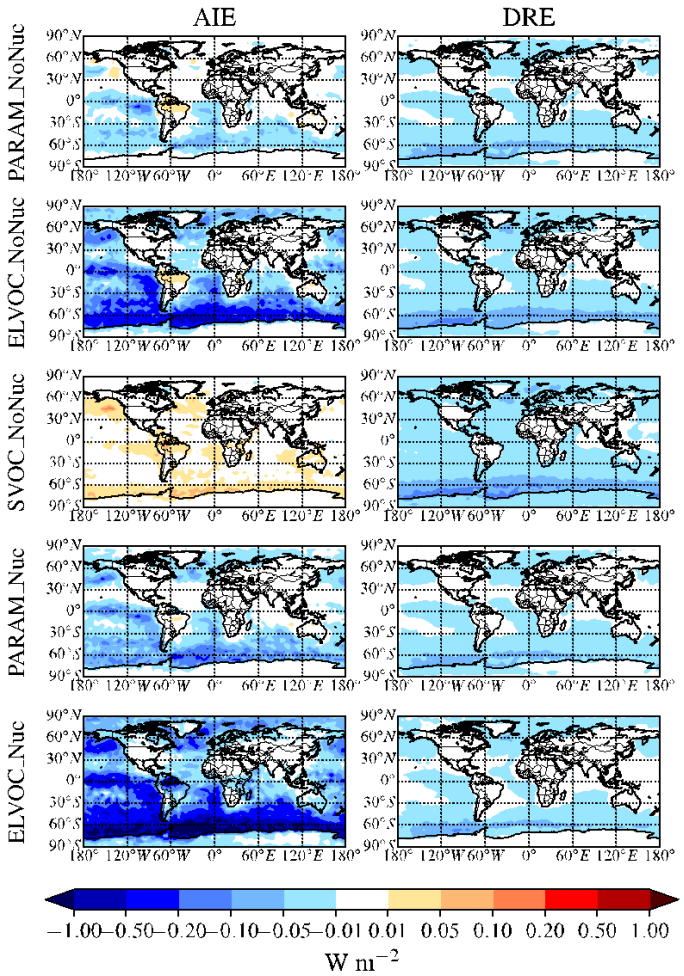

Figure 4. Global annual mean change in W m^{-2} for the aerosol indirect effect (cloud-albedo AIE, denoted as 'AIE'; first column) and the direct radiative effect (DRE; second column) between DEFAULT_NoMSA and PARAM_NoNuc (first row), ELVOC_NoNuc (second row), SVOC_Nuc (third row), PARAM_Nuc (fourth row), and ELVOC_Nuc (fifth row) (warm colors indicate an increase in the AIE/DRE as compared to DEFAULT_NoMSA).

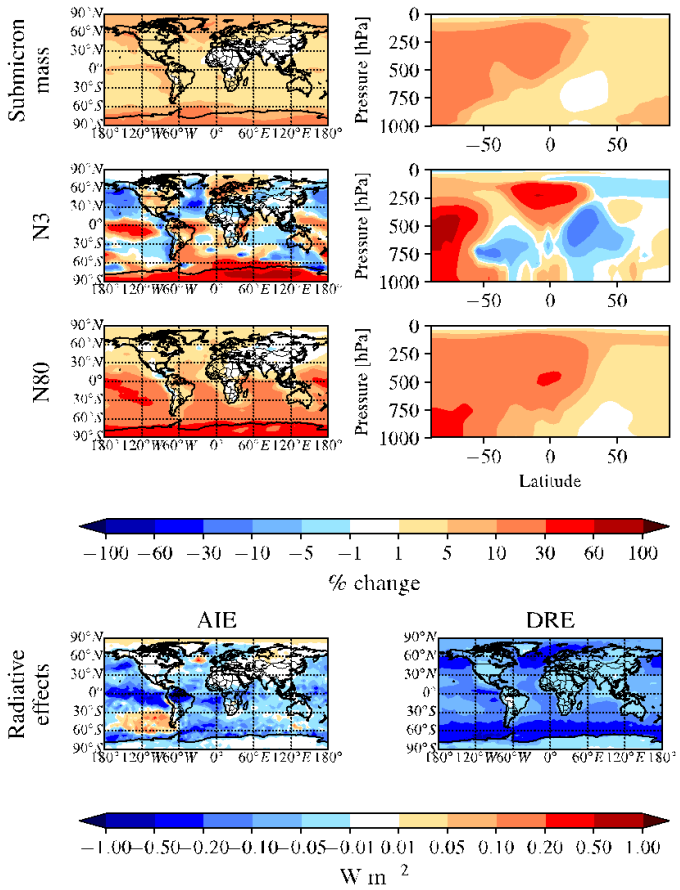

Figure 5. Global annual mean changes between the NoDMS_NoMSA and DEFAULT_NoMSA simulation. First row: percent change in submicron aerosol mass at 900 hPa (left) and zonally (right). Second row: percent change in N3 at 900 hPa (left) and zonally (right). Third row: percent change in N80 at 900 hPa (left) and zonally (right). Fourth row: change in W m^{-2} in the radiative effects. This figures gives the contribution from sulfate and sulfuric acid produced from DMS/SO_2 oxidation to the aerosol mass, number, and radiative effects. Warm colors indicate that sulfate and sulfuric acid produced from DMS/SO_2 oxidation increase the metric.

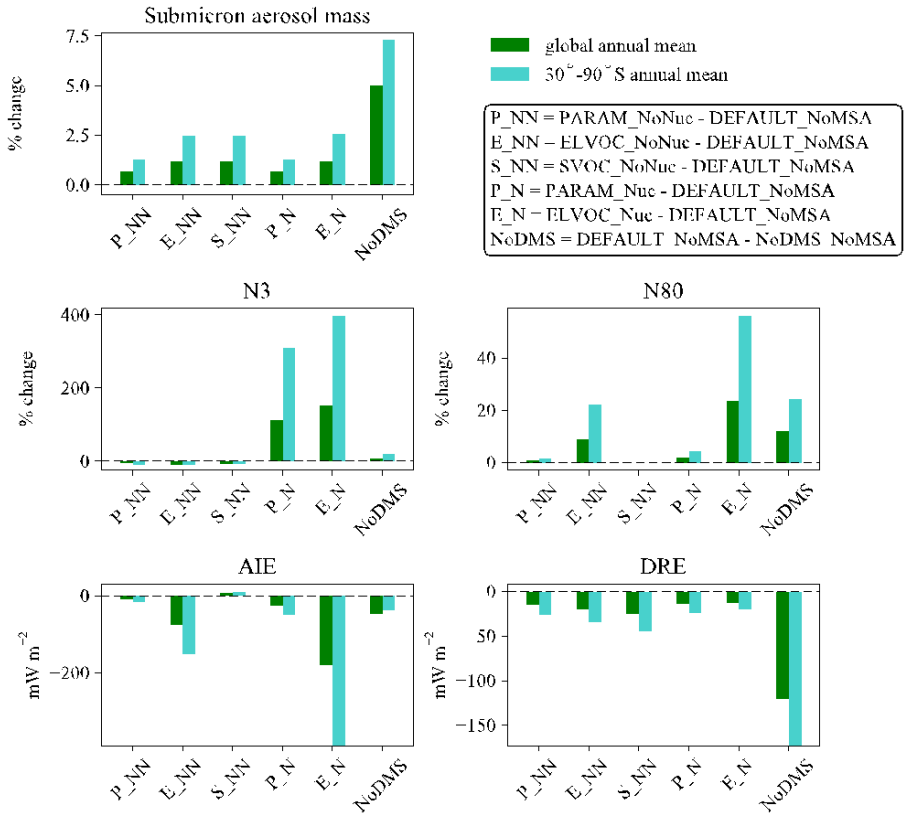

Figure 6. Annual mean changes due to MSA at 900 hPa for each MSA simulation relative to the DEFAULT_NoMSA simulation for submicron aerosol mass, N3, N80, all expressed as percent changes, and radiative forcing changes in cloud-albedo AIE (denoted as 'AIE') and DRE, both expressed as changes in W m^{-2}. Positive values for any metric for PARAM_NoNuc (P_NN), ELVOC_NoNuc (E_NN), SVOC_NoNuc (S_NN), PARAM_Nuc (P_N), and ELVOC_Nuc (E_N) all indicate that the addition of MSA increases that metric relative to the DEFAULT_NoMSA simulation. The DEFAULT_NoMSA-NoDMS_NoMSA (NoDMS) columns shows the contribution of the sulfate and sulfuric acid from DMS/SO_2 oxidation present in the DEFAULT_NoMSA simulation; positive values of a metric indicate that the sulfate and

sulfuric acid increases that metric compared to a simulation with no DMS emissions. Numerical values for each bar are provided in Table S3.

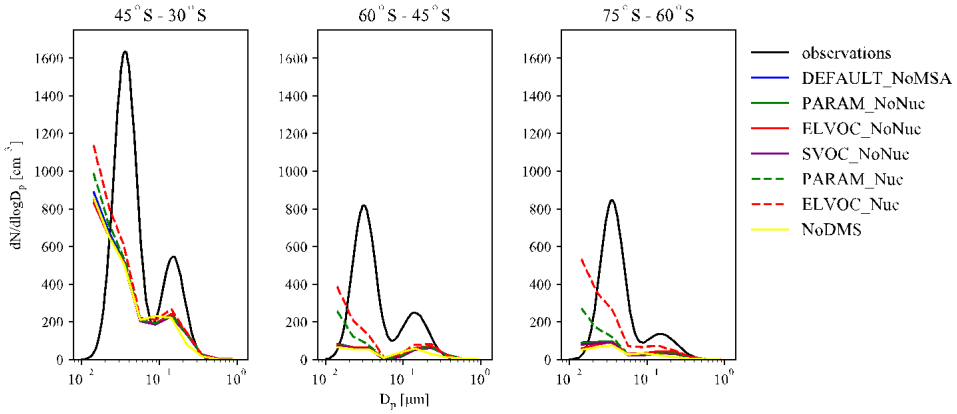

Figure 7. Comparison of simulated annual mean particle number size distributions to the annual zonal particle number size distributions compiled in Heintzenberg et al. (2000) (black lines) for the southern oceans. No data was available in Heintzenberg et al. (2000) for 75-90° S. We match the grid boxes sampled in their study to the GEOS-Chem-TOMAS grid boxes; due to sparseness of data, we do not attempt to discuss seasonal variabilities in this comparison.

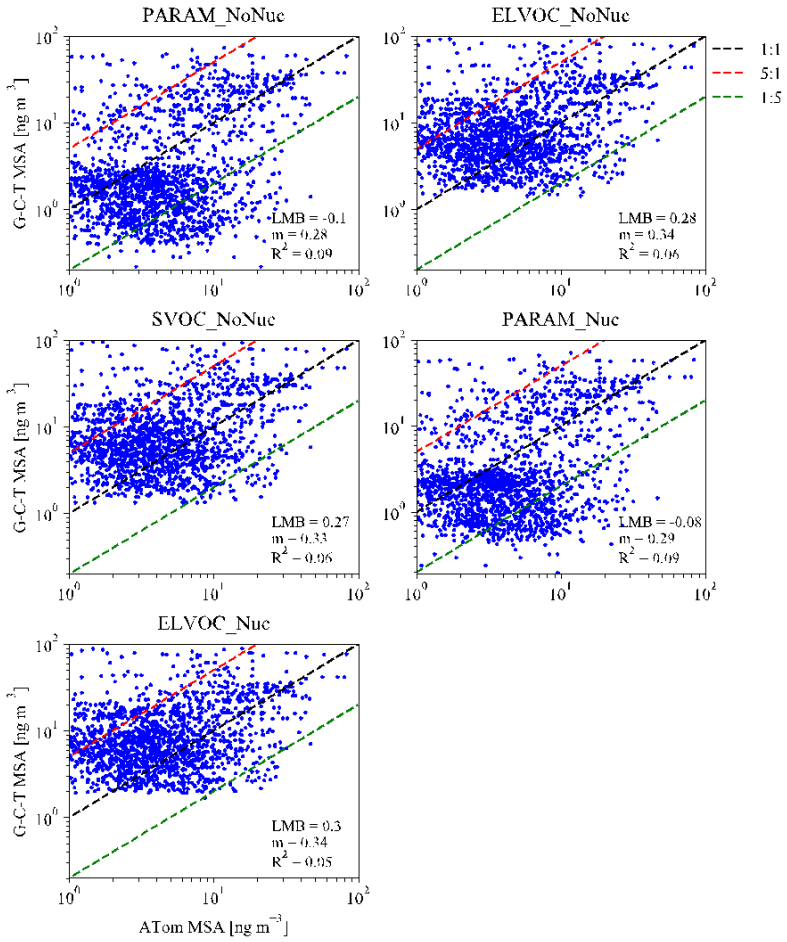

Figure 8. 1:1 (black dashed line) plots for the simulated mean MSA mass for the months of August/February and measured MSA mass during the ATom-1/Atom-2 campaigns (July 28-August 22 2016 / January 26-February 22 2017). Each subpanel gives the calculated log-mean bias (LMB), slope (m), and coefficient of determination (R^2) between the ATom data and the sensitivity simulation. The red and green dashed lines indicate 5:1 and 1:5 lines. Simulated MSA mass is calculated by subtracting the total sulfate mass for the base case from each sensitivity case.

Supplemental information to:
The potential role of methanesulfonic acid (MSA) in aerosol formation and growth and the associated radiative forcings

Anna L. Hodshire[1], Pedro Campuzano-Jost[2,3], John K. Kodros[1], Betty Croft[4], Benjamin A. Nault[2,3], Jason C. Schroder[2,3], Jose L. Jimenez[2,3], Jeffrey R. Pierce[1]

[1]Department of Atmospheric Science, Colorado State University, Fort Collins, CO 80523, USA
[2]Department of Chemistry, University of Colorado, Boulder, CO, USA
[3]Cooperative Institute for Research in Environmental Sciences, University of Colorado, Boulder, CO, USA
[4]Dalhousie University, Department of Physics and Atmospheric Science, Halifax, NS, B3H 4R2, Canada

Correspondence to: Anna L. Hodshire (Anna.Hodshire@colostate.edu)

S1. Simulated ammonia concentrations

Annually (Fig. S1) and seasonally (Fig. S2) averaged simulated concentrations of ammonia from the GEOS-Chem-TOMAS model. Each map is made from the reported ammonia concentrations for the DEFAULT_NoMSA model.

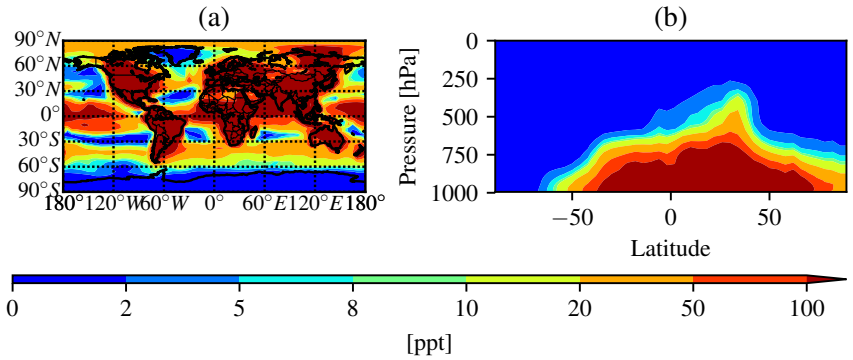

Figure S1. Global annual average predicted NH_3 concentrations at (a) the surface and (b) zonally. For the PARAM_NoNuc and PARAM_Nuc cases, it's assumed that if $[NH_3] <$ 10 ppt (blue colors), then the model is under low-base (no free ammonia) conditions (Figure 1a).

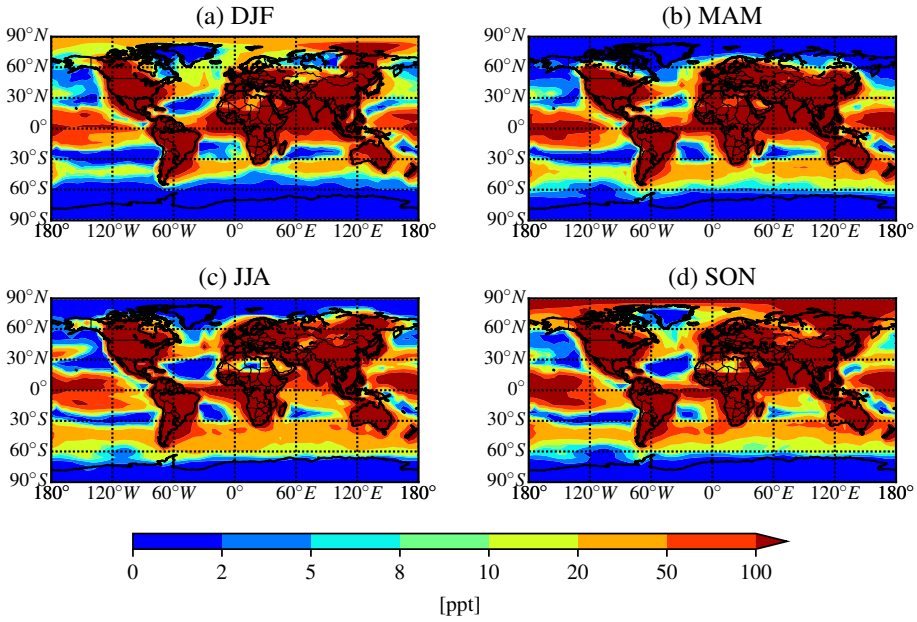

Figure S2. Global seasonal average predicted NH_3 concentrations at the surface for: (a) December, January, February; (b) March, April, May; (c) June, July, August; and (d) September, October, November. For the PARAM_NoNuc and PARAM_Nuc cases, it's assumed that if $[NH_3] < 10$ ppt (blue colors), then the model is under low-base (no free ammonia) conditions (Figure 1a).

S2. Comparison of different DMS emission inventories in GEOS-Chem-TOMAS.

We test the sensitivity of the size distribution towards the DMS emissions in two ways: (1) we replace the default DMS emissions inventory for GEOS-Chem v10.01 (Kettle et al., 1999; Kettle and Andreae, 2000) with the updated emissions inventory by Lana et al., (2010) and (2) we increase the default DMS emissions inventory globally by a factor of two. We hereon refer to each inventory as the default DMS inventory, the Lana DMS inventory, and the 2xDMS inventory. The results of these tests are shown in Tables S1-S2 and Figs. S3-S5. Table S1 and Fig. S3 shows the comparisons between each DEFAULT_NoMSA simulation (DEFAULT_NoMSA, DEFAULT_NoMSA_Lana, and DEFAULT_NoMSA_2xDMS) and the NoDMS simulation. This indicates the contribution from sulfate and sulfuric acid produced by DMS/SO_2 oxidation for each DMS emissions inventory. Table S2 and Fig. S4-S5 shows the comparisons between each PARAM_NoNuc case and each DEFAULT_NoMSA case for submicron aerosol mass (only in Table S2), N3 and N80 (Fig. S5) and the AIE and DRE (Fig. S6). It is seen that for the Lana DMS inventory, both the NoDMS (Fig. S3) and PARAM_NoNuc_Lana (Figs. S4-S5) case comparisons have only small spatial differences and similar magnitude of effects as compared to the default DMS inventory. Thus, if DMS emissions are better simulated by the Lana DMS inventory, our general conclusions would not be changed about the effects of MSA towards the size distribution.

The 2xDMS inventory shows some non-trivial changes in N80 for some regions and levels as compared to the default DMS inventory for the NoDMS comparison (Table S1; Fig. S3), primarily with increases in N80 over the Antarctic between 800-500 hPa and over ~20°S -20° N between 500-100 hPa, and decreases in N80 over 50°-90° N between 1000-750 hPa. The increase in sulfuric acid from DMS/SO_2 oxidation will boost particle formation and growth rates in relatively clean regions, such as the Antarctic. There will also be a boost from condensed sulfate from aqueous oxidation of DMS, further increasing the sizes but not necessarily number concentration of larger particles. However, the PARAM_NoNuc_2xDMS case is very similar to the PARAM_NoNuc case (Table S2; Figs. S4 and S5) and again, we conclude that even if DMS emissions are globally increased by up to a factor of two, our general conclusions would not be changed about the effects of MSA towards the size distribution.

Table S1. Annual mean % changes at 900 hPa for the contribution of the sulfate and sulfuric acid from DMS/SO_2 oxidation for submicron aerosol mass, N3, N80, and radiative forcing changes in AIE and DRE for each DEFAULT_NoMSA emissions inventory. Positive values of a metric indicate that the sulfate and sulfuric acid increases that metric compared to a simulation with no DMS emissions.

Case	Submicron aerosol mass global (30-90 S) % change	N3 global (30-90 S) % change	N80 global (30-90 S) % change	AIE global (30-90 S) change in mW m^{-2}	DRE global (30-90 S) change in mW m^{-2}
DEFAULT_NoMSA - NoDMS_NoMSA	5.0 % (7.3 %)	7.3 % (19.5 %)	12.2 % (24.3 %)	-46 (-38)	-120 (-170)
DEFAULT_NoMSA_Lana - NoDMS	5.0 % (7.6 %)	7.0 % (19.4 %)	12.6 % (24.8 %)	-51 (-39)	-130 (-200)
DEFAULT_NoMSA_2xDMS - NoDMS	8.0 % (12.6 %)	7.5 % (22.9 %)	16.3% (35.4 %)	-92 (-130)	-220 (-330)

Table S2. Annual mean % changes at 900 hPa for the MSA for submicron aerosol mass, N3, N80, and radiative forcing changes in AIE and DRE for the PARAM_NoNuc simulations using each DEFAULT_NoMSA emissions inventory. Positive values of a metric indicate that MSA increases that metric compared to the DEFAULT_NoMSA case per emissions inventory.

Case	Submicron aerosol mass global (30-90 S) % change	N3 global (30-90 S) % change	N80 global (30-90 S) % change	AIE global (30-90 S) change in mW m^{-2}	DRE global (30-90 S) change in mW m^{-2}
PARAM_NoNuc - DEFAULT_NoMSA	0.7 % (1.3 %)	-3.9 % (-8.5 %)	0.8 % (1.7 %)	-8.6 (-17)	-15 (-26)
PARAM_NoNuc_Lana - DEFAULT_NoMSA_Lana	0.7 % (1.3%)	-3.5 % (-7.1 %)	0.8 % (1.7 %)	-7.8 (-14)	-16 (-28)
PARAM_NoNuc_2xDMS - DEFAULT_NoMSA_2xDMS	1.2 % (2.3 %)	-4.3 % (-7.7 %)	0.3 % (0.6 %)	-6 (-3.1)	-28 (-46)

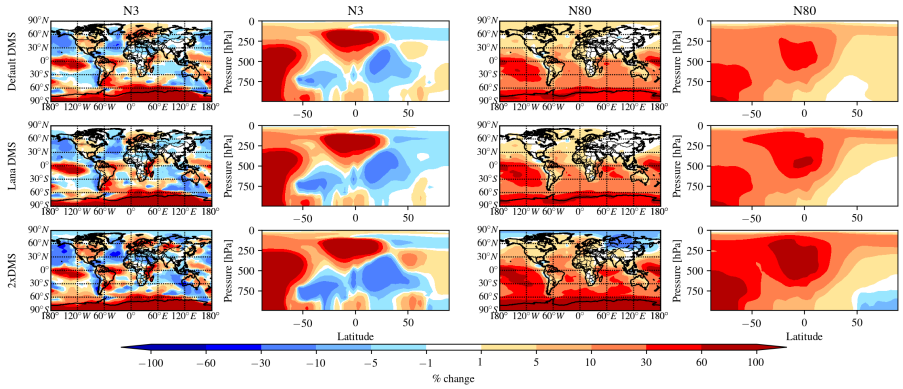

Figure S3. Global annual mean percent change at 900 hPa (first and third column) and global zonal annual mean percent change (second and fourth column) between NoDMS_NoMSA and the DEFAULT_NoMSA case (first row), the DEFAULT_NoMSA_Lana case (second row), and the DEFAULT_NoMSA_2xDMS case (third row). First and second column: N3 (the number concentration of particles with diameters larger than 3 nm). Third and fourth column: N80. Warm colors indicate that the inclusion of DMS/SO_2 oxidation products in the model increases N3/N80.

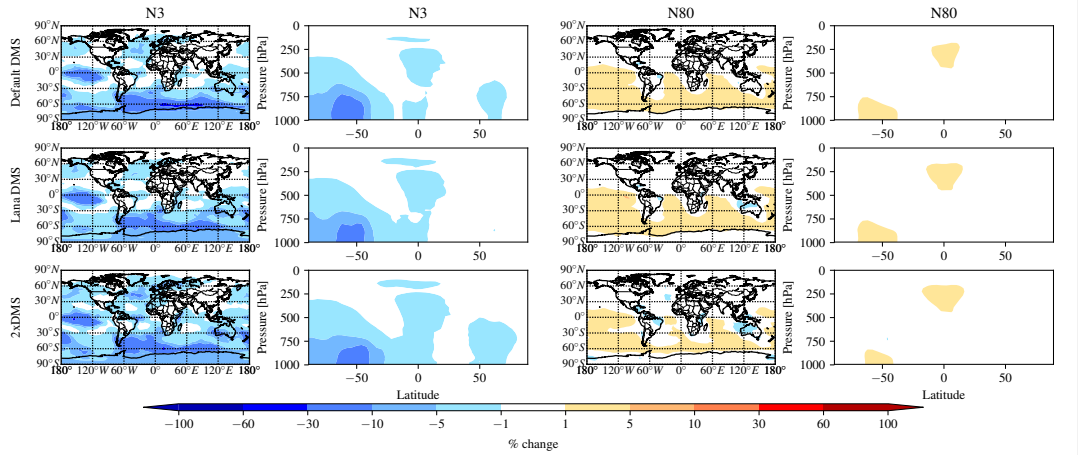

Figure S4. Global annual mean percent change at 900 hPa (first and third column) and global zonal annual mean percent change (second and fourth column) between the DEFAULT_NoMSA case and PARAM_NoNuc case (first row), the DEFAULT_NoMSA_Lana case and PARAM_NoNuc_Lana case (second row), and the DEFAULT_NoMSA_2xDMS case and PARAM_NoNuc_2xDMS case (third row). First and second column: N3 (the number concentration of particles with diameters larger than 3 nm). Third and fourth column: N80.

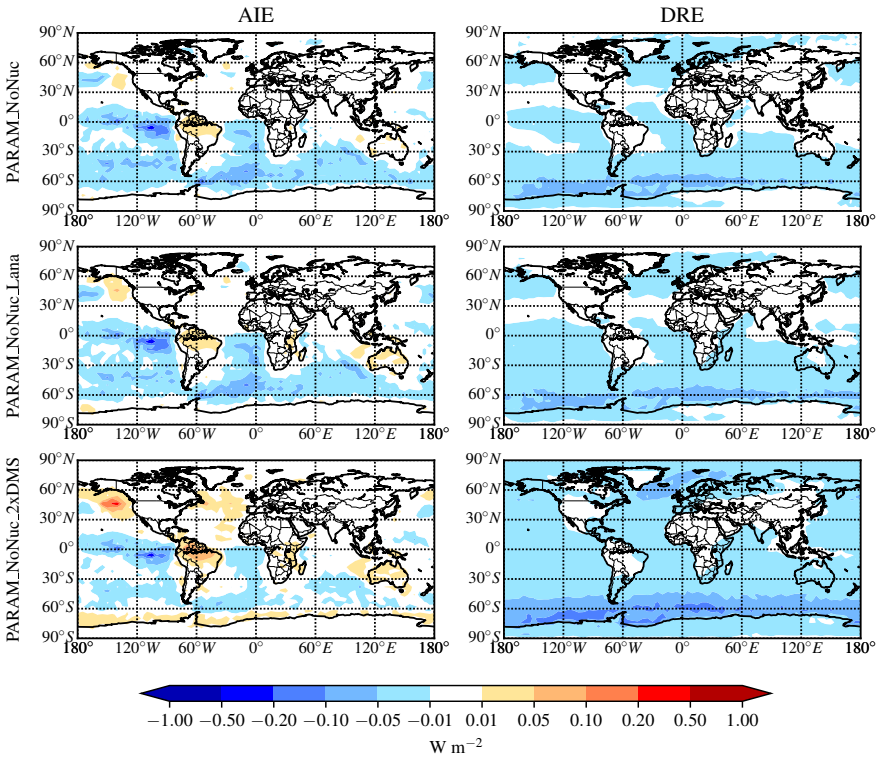

Figure S5. Global annual mean percent change for the AIE (first column) and DRE (second column) between the DEFAULT_NoMSA case and PARAM_NoNuc case (first row), the DEFAULT_NoMSA_Lana case and PARAM_NoNuc_Lana case (second row), and the DEFAULT_NoMSA_2xDMS case and PARAM_NoNuc_2xDMS case (third row).

S3. Global annual mean number concentrations for the DEFAULT_NoMSA case; additional results

Figure S6 provides the number concentrations (N3 and N80) at 900 hPa and zonally for the base case (DEFAULT_NoMSA). Table S3 provides the quantitative values for Fig. 6 (main text).

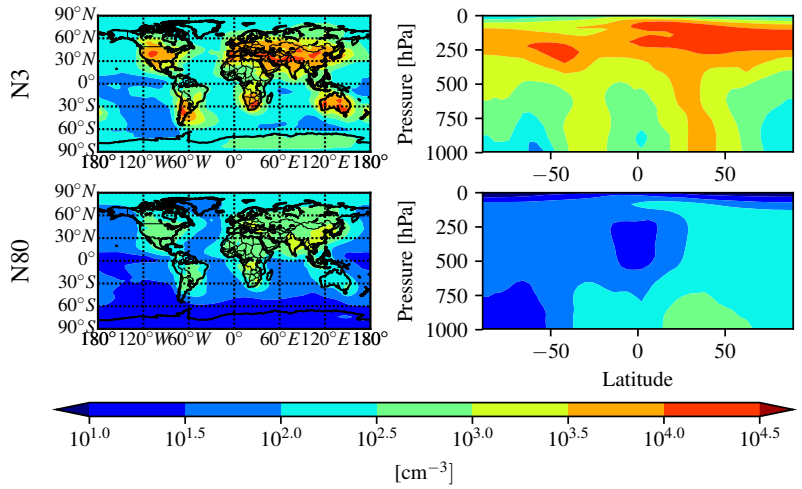

Figure S6. The number concentration (cm^{-3}) normalized to STP for the BASE case. Top row: N3 at cloud level (900 hPa; right) and zonally (left). Bottom row: N80 for cloud level (900 hPa; right) and zonally (left).

Anna Hodshire 2/12/2019 3:36 PM

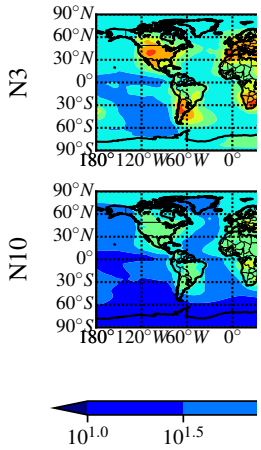

Deleted:

Table S3. Annual mean % changes due to MSA at 900 hPa for each MSA simulation relative to the DEFAULT_NoMSA simulation for submicron aerosol mass, N3, N80, and radiative forcing changes in AIE and DRE. Positive values for any metric for PARAM_NoNuc, ELVOC_NoNuc, SVOC_NoNuc, PARAM_Nuc, and ELVOC_Nuc all indicate that the addition of MSA increases that metric relative to the DEFAULT_NoMSA simulation. The DEFAULT_NoMSA-NoDMS_NoMSA row shows the contribution of the sulfate and sulfuric acid from DMS/SO_2 oxidation present in the DEFAULT_NoMSA simulation; positive values of a metric indicate that the sulfate and sulfuric acid increases that metric compared to a simulation with no DMS emissions.

Case	Submicron aerosol mass global (30-90 S) % change	N3 global (30-90 S) % change	N80 global (30-90 S) % change	AIE global (30-90 S) change in mW m^{-2}	DRE global (30-90 S) change in mW m^{-2}
PARAM_NoNuc - DEFAULT_NoMSA	0.7 % (1.3 %)	-3.9 % (-8.5 %)	0.8 % (1.7 %)	-8.6 (-17)	-15 (-26.0)
ELVOC_NoNuc - DEFAULT_NoMSA	1.2 % (2.5%)	-8.9 % (-20.8 %)	9.1 % (22.2 %)	-75 (-150)	-20 (-34)
SVOC_NoNuc - DEFAULT_NoMSA	1.2 % (2.5 %)	-6.0 % (-12.6 %)	-0.2 % (-0.12 %)	7.5 (11)	-25 (-44)
PARAM_Nuc - DEFAULT_NoMSA	0.7 % (1.3 %)	112.5 % (309.9 %)	2.1 % (4.4 %)	-26 (-48)	-14 (-24)
ELVOC_Nuc - DEFAULT_NoMSA	1.2% (2.6%)	153.4 % (397.7 %)	23.8 % (56.3 %)	-180 (-390)	-13 (-20)
DEFAULT_NoMSA - NoDMS_NoMSA (indicates contribution from DMS/SO_2 oxidation)	5.0 % (7.3 %)	7.3 % (19.5 %)	12.2 % (24.3 %)	-46 (-38)	-120 (-170)

S4. ATom-1 and ATom-2 plots

The ATom-1 and ATom-2 campaigns took place during July 28-August 22, 2016, and January 26-February 22, 2017, respectively. Both campaigns took measurements from the Pacific and Atlantic Basin. Figures S7-S10 provide the 1:1 plots for each separate campaign and each separate ocean basin for the main MSA sensitivity cases in this study, PARAM_NoNuc, ELVOC_NoNuc, SVOC_NoNuc, PARAM_Nuc, and ELVOC_Nuc. Also shown are the 5:1 and 1:5 lines. Each subplot indicates the log mean bias (LMB), slope (m), and coefficient of determination (R^2) for each sensitivity case as compared to the measurements. Figures S11-S14 show the zonally averaged simulated MSA concentrations for each model level for each basin and campaign with the corresponding particle-phase MSA measurements overlaid. (The up and down patterns represent the flight tracks of the NASA DC-8 aircraft.)

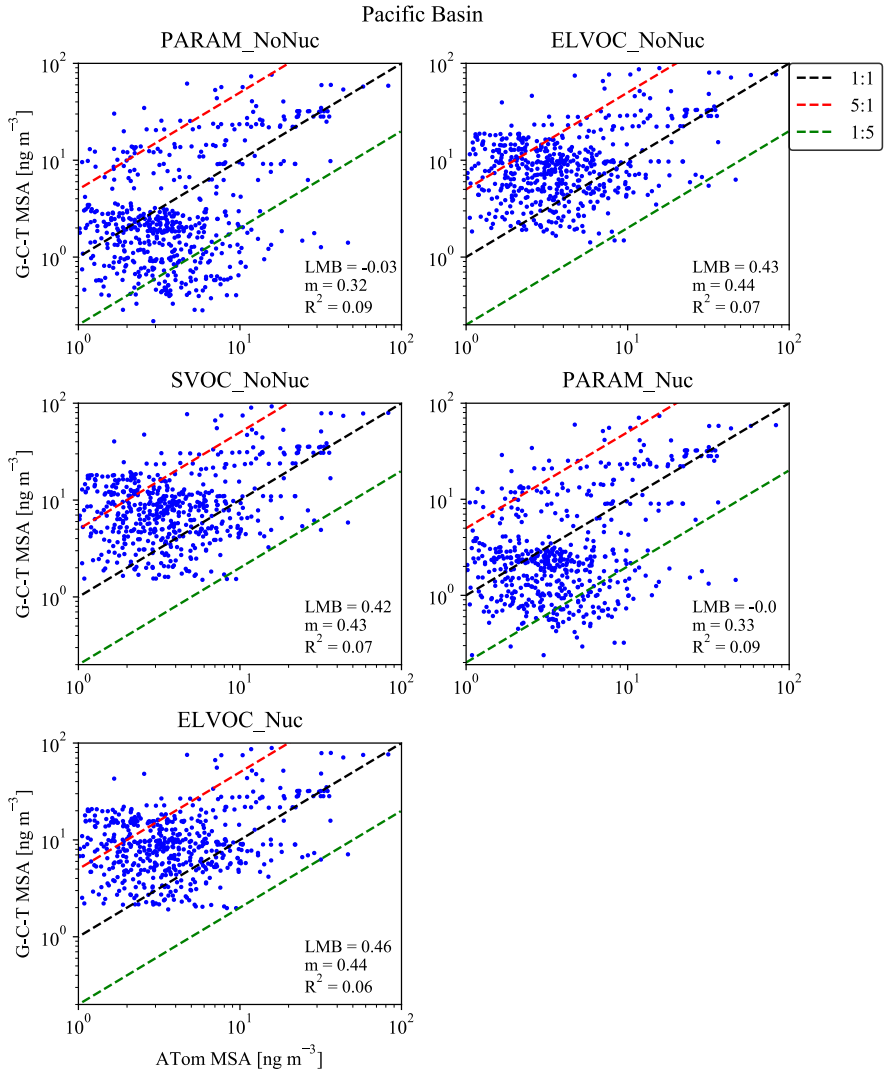

Figure S7. 1:1 (black dashed line) plots for the simulated mean MSA mass for the month of August and measured MSA mass during the ATom-1 campaign (July 28-August 22 2016) for the Pacific basin flight tracks, calculated log-mean bias (LMB), slope (*m*), and coefficient of determination (R^2). The red and green dashed lines indicate 5:1 and 1:5 lines. Simulated MSA mass is calculated by subtracting the total sulfate mass for the base case from each sensitivity case.

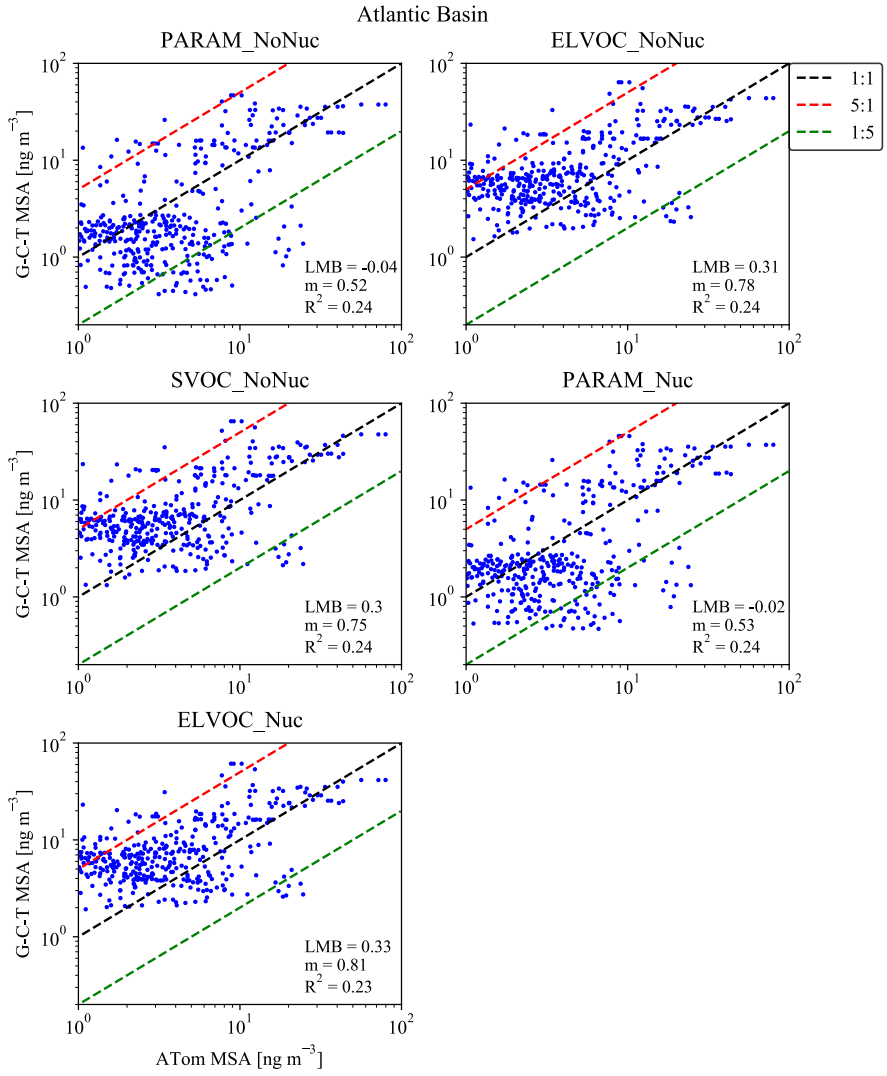

Figure S8. 1:1 (black dashed line) plots for the simulated mean MSA mass for the month of August and measured MSA mass during the ATom-1 campaign (July 28-August 22 2016) for the Atlantic basin flight tracks, calculated log-mean bias (LMB), slope (*m*), and coefficient of determination (R^2). The red and green dashed lines indicate 5:1 and 1:5 lines. Simulated MSA mass is calculated by subtracting the total sulfate mass for the base case from each sensitivity case.

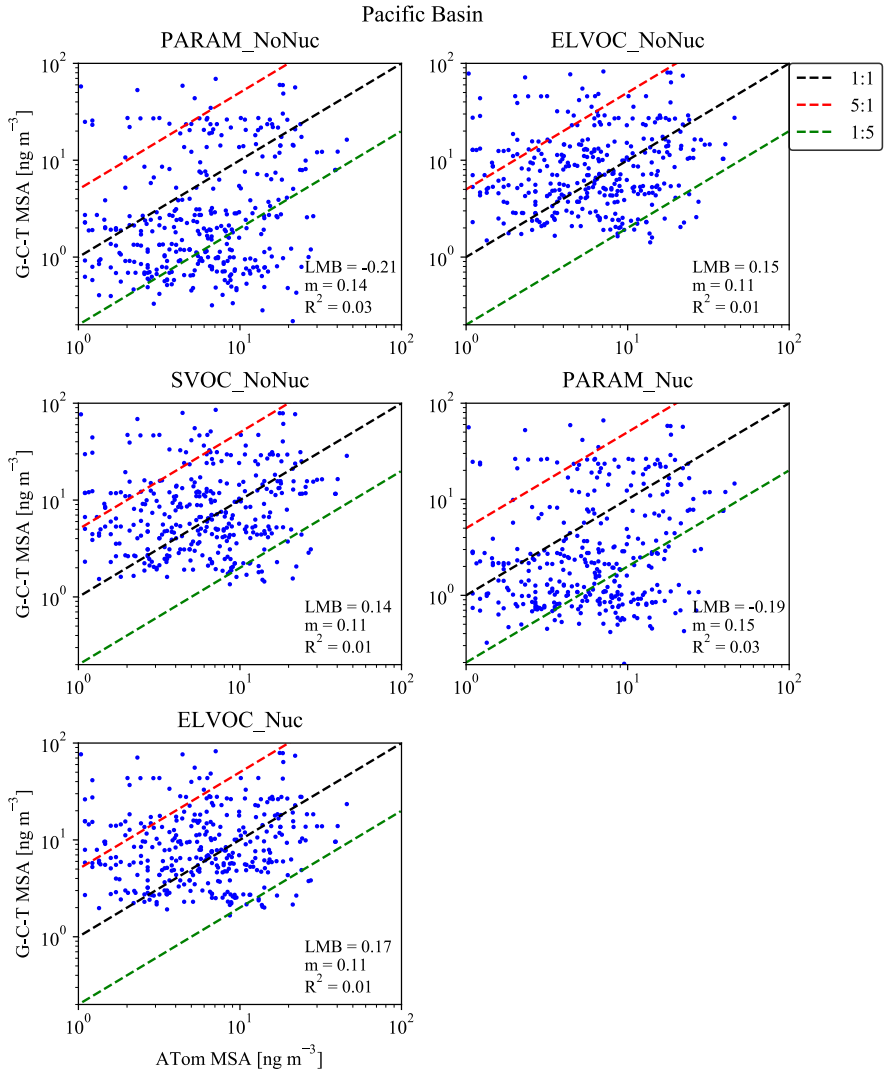

Figure S9. 1:1 (black dashed line) plots for the simulated mean MSA mass for the month of February and measured MSA mass during the ATom-2 campaign (January 26-February 22 2017) for the Pacific basin flight tracks, calculated log-mean bias (LMB), slope (*m*), and coefficient of determination (R^2). The red and green dashed lines indicate 5:1 and 1:5 lines. Simulated MSA mass is calculated by subtracting the total sulfate mass for the base case from each sensitivity case.

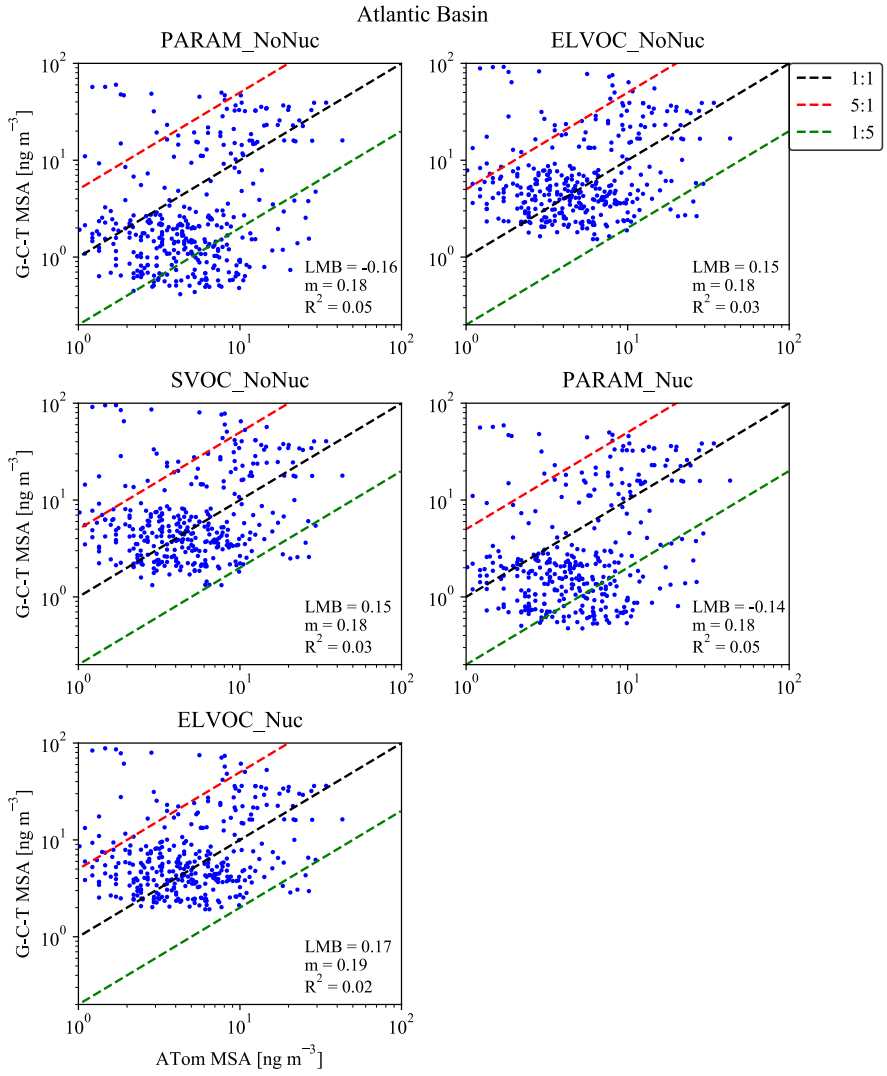

Figure S10. 1:1 (black dashed line) plots for the simulated mean MSA mass for the month of February and measured MSA mass during the ATom-2 campaign (January 26-February 22 2017) for the Atlantic basin flight tracks, calculated log-mean bias (LMB), slope (*m*), and coefficient of determination (R^2). The red and green dashed lines indicate 5:1 and 1:5 lines. Simulated MSA mass is calculated by subtracting the total sulfate mass for the base case from each sensitivity case.

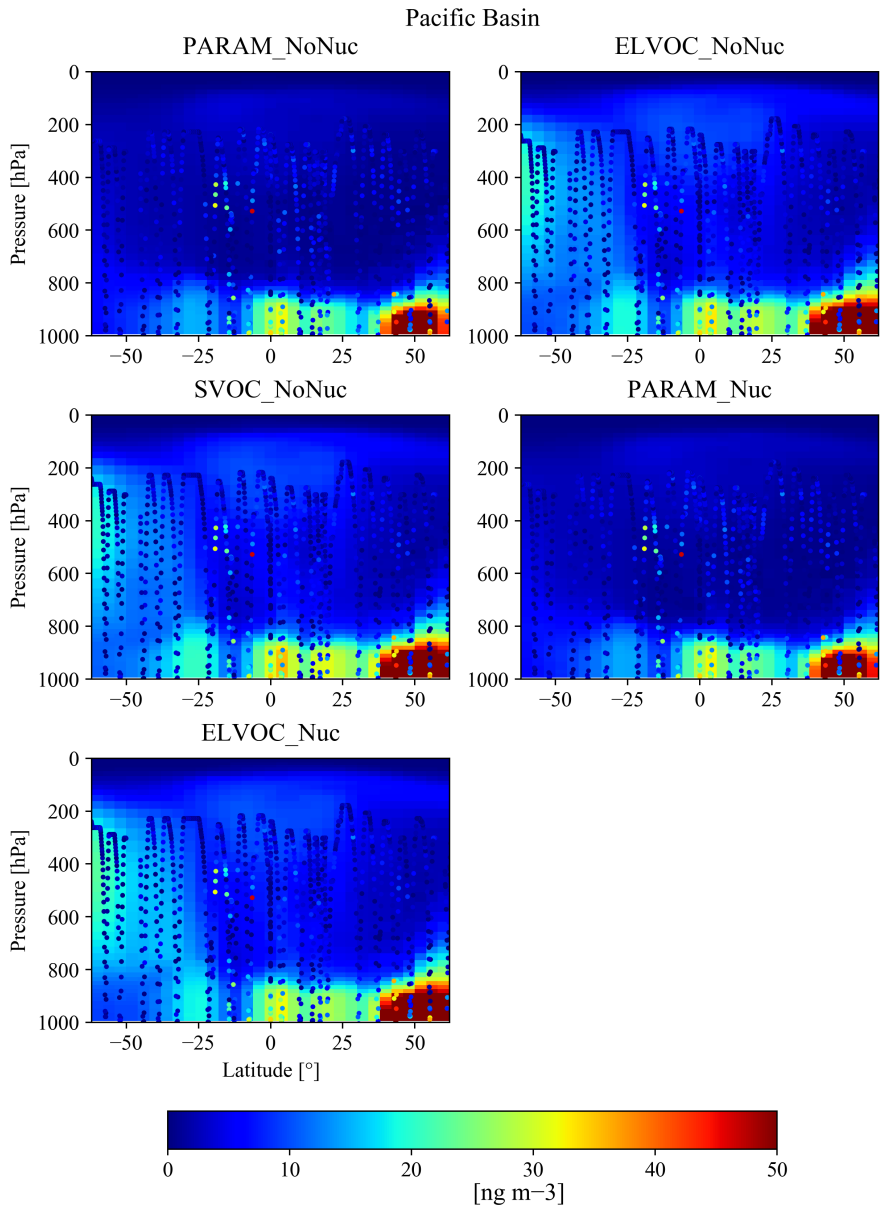

Figure S11. Comparison of simulated mean MSA mass for the month of August to measured MSA mass (circles) during the ATom-1 campaign (July 28-August 22 2016) for the Pacific basin flight tracks. Simulated MSA mass is calculated by subtracting the total sulfate mass for the base case from each sensitivity case.

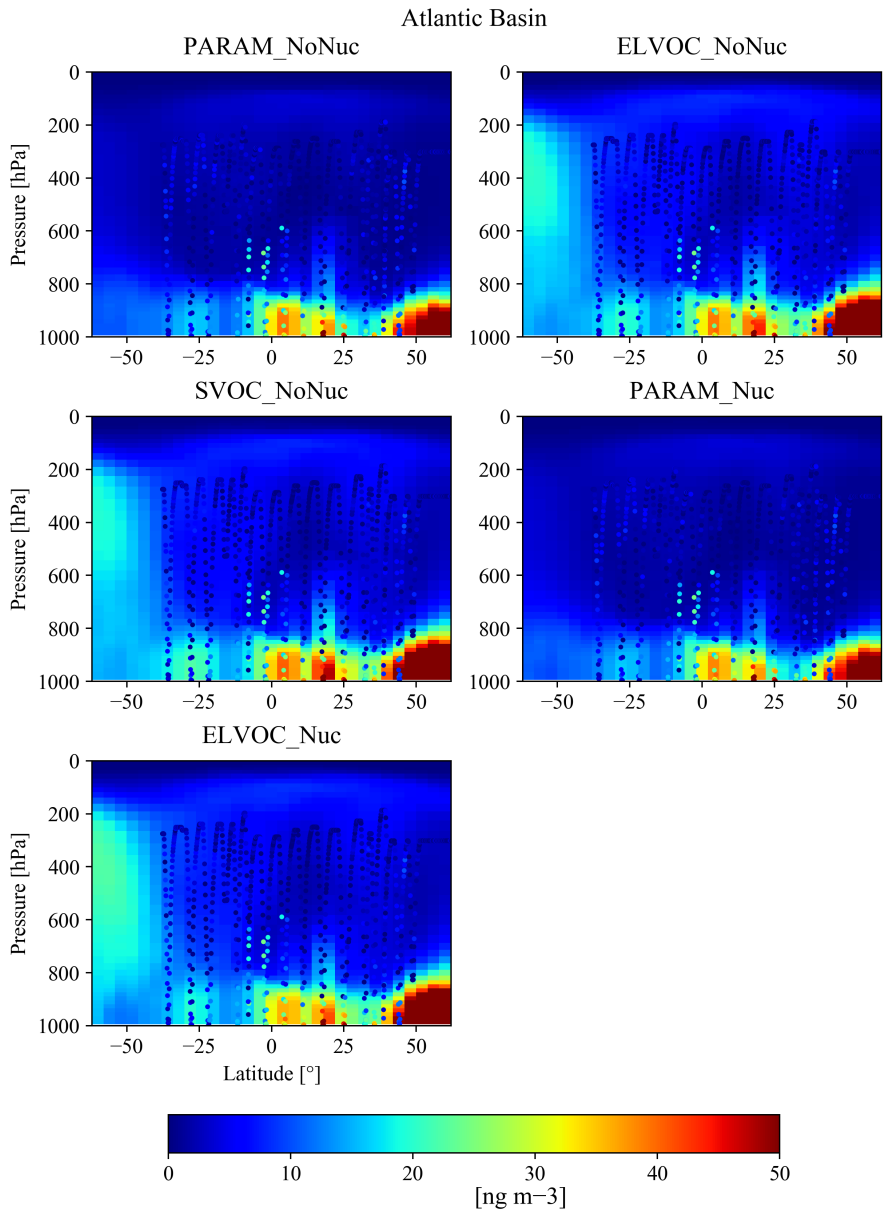

Figure S12. Comparison of simulated mean MSA mass for the month of August to measured MSA mass (circles) during the ATom-1 campaign (July 28-August 22 2016) for the Atlantic basin flight tracks. Simulated MSA mass is calculated by subtracting the total sulfate mass for the base case from each sensitivity case.

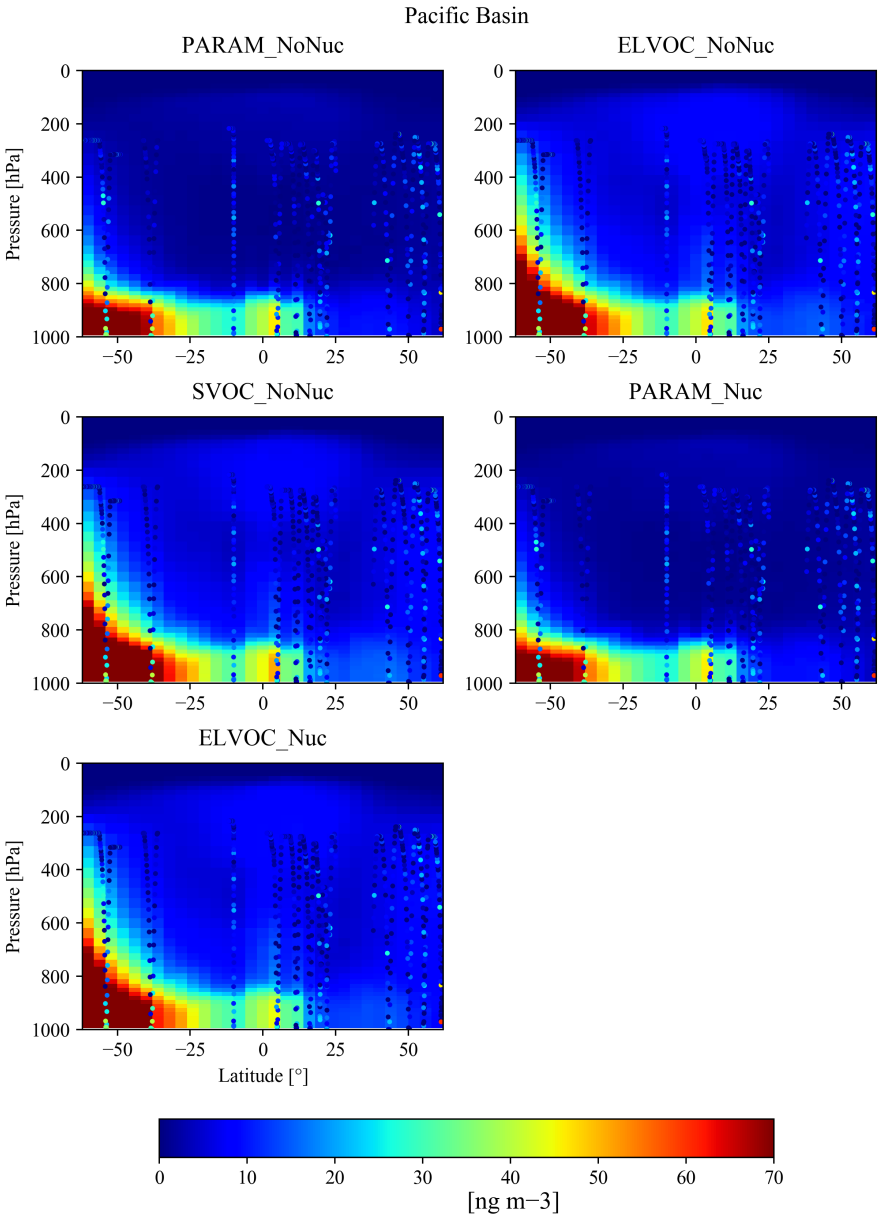

Figure S13. Comparison of simulated mean MSA mass for the month of February to measured MSA mass (circles) during the ATom-2 campaign (January 26-February 22 2017) for the Pacific basin flight tracks. Simulated MSA mass is calculated by subtracting the total sulfate mass for the base case from each sensitivity case.

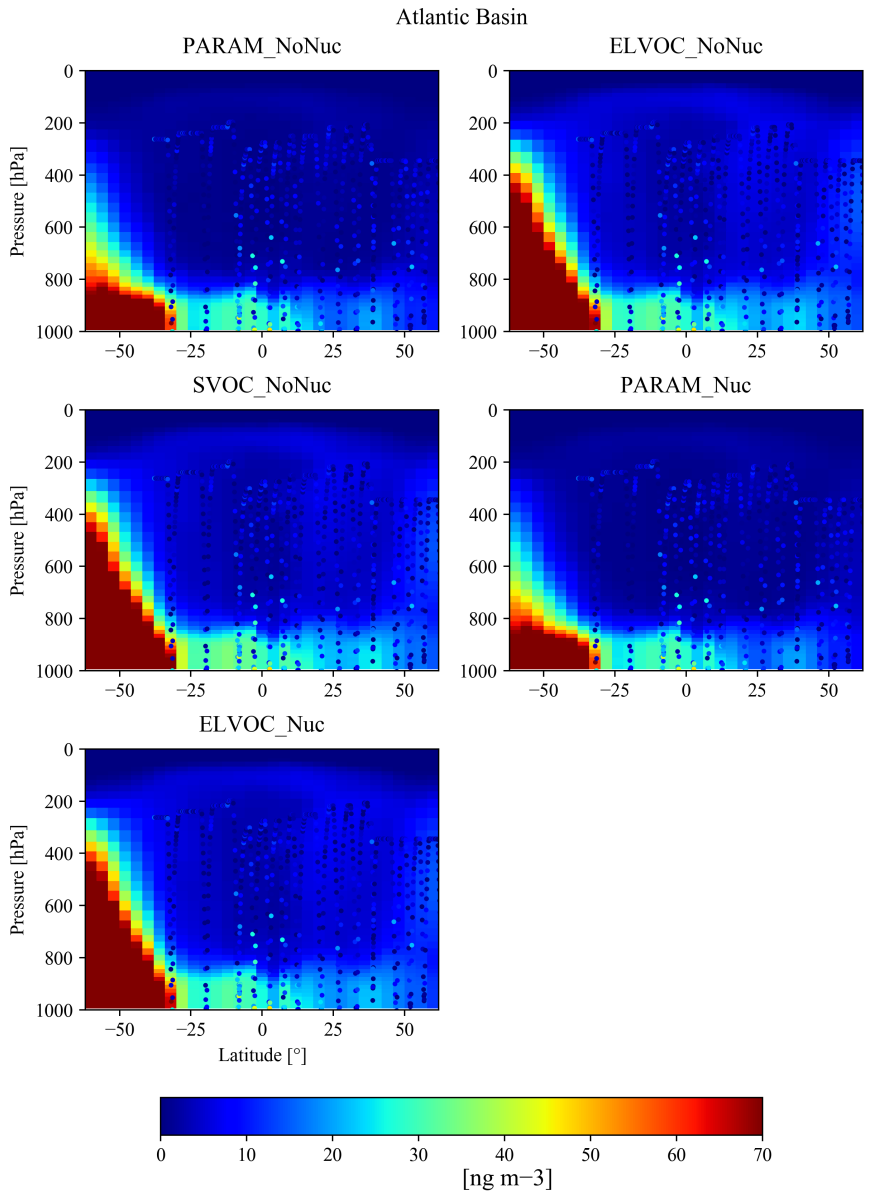

Figure S14. Comparison of simulated mean MSA mass for the month of February to measured MSA mass (circles) during the ATom-2 campaign (January 26-February 22 2017) for the Atlantic basin flight tracks. Simulated MSA mass is calculated by subtracting the total sulfate mass for the base case from each sensitivity case.

S5. MSA Calibration Details for the Aerosol Mass Spectrometer

S5.1. General Approach

As shown first by Phinney et al. (2006), $CH_3SO_2^+$ is a highly specific ion for the identification of MSA in AMS spectra. A number of groups have since used this ion as a calibrated marker for quantification of MSA. Other quantification approaches have also been used but they have often have proven less robust as discussed in Huang et al. (2017).

This quantification procedure requires the determination of two MSA specific quantities (Zorn et al., 2008, Huang et al., 2015, Willis et al., 2016, Huang et al., 2017):

- The ratio of the $CH_3SO_2^+$ ion to the total AMS signal from MSA, $f(CH_3SO_2)$, and
- The relative ionization efficiency of the total AMS response (ion current) from MSA relative to nitrate (the primary AMS calibrant), RIE_{MSA}. Once those quantities are known, the MSA concentration can be determined as follows (based on the general expression for calculating species concentrations in the AMS; Canagaratna et al., 2007):

$$[MSA] = \frac{C}{CE}\frac{MW_{MSA}}{IE_{MSA}}\sum I_{MSA} = \frac{C}{CE}\frac{MW_{NO3}}{RIE_{MSA}IE_{NO3}}\frac{I_{CH3SO2}}{f(CH_3SO_2)} \quad (Eq.S1)$$

In this equation I_{CH3SO2} refers to the signal of the marker ion (in ion counts, our measured variable), IE_{NO3} is the ionization efficiency of the instrument for nitrate, CE is the collection efficiency, MW_{MSA} and MW_{NO3} are the molar masses of MSA and nitrate, respectively, and C is a proportionality constant that includes the MS duty cycle, flow calibration, and unit conversions.

Both of these quantities were determined over a series of both laboratory and in-field calibrations (starting at the end of the ATom-1 deployment) by atomizing either pure dilute MSA solutions (Aldrich, >99.9% purity), or dilute solutions that were previously neutralized with excess aqueous ammonia (Aldrich, ACS reagent). The nebulizer output for the neutralized solutions (effectively $NH_4CH_3SO_3$, referred to as AMSA in the following) was size-selected with an SMPS (TSI 3936) and the aerosol number concentration was recorded with a collocated CPC (TSI 3010). Due to the high amounts of ammonium (from the daily ammonium nitrate calibrations) present in our in-field calibration system, the nebulized pure MSA aerosol was introduced directly into the AMS to avoid neutralization in the SMPS. Hence, for acidic MSA, only the fragmentation pattern was investigated.

S5.2. Estimation of minor ion contributions

In order to account properly for the total ion signal of MSA, the contribution of some ions that had a high background was estimated by indirect means:

- The contribution of both water ions (O_2 HO^+, and H_2O^+, "familyHO" in AMS parlance) and CO_2^+ were obtained from unconstrained linear regressions, so they could be separated from the gas phase contributions. Since the AMS flying on ATom uses a cryopump for background reduction, the water background is low enough for this method to work (typically H_2O:N_2 ~ 0.1 for the background signals).
- The contribution of the sulfur ion (S^+) to the AMS signal was estimated based on the abundance of the (independently fitted) $^{34}S^+$ isotope at low MSA concentrations, and fitted directly at high concentrations (> 1 mg sm^{-3})

- The contribution of CO^+ to the AMS signal was estimated from fitting $C^{18}O^+$, but was found to be negligible at all times (<1%)

Figure S15a shows a typical regression of the different ion species for an AMSA calibration, while Fig. S15b shows the contributions of the water, sulfur and CO_2^+ ions to the total signal for all calibrations. On average, the contribution of these ions to the total MSA signal are small (about 5% in total), in contrast to sulfate (discussed in S5.5).

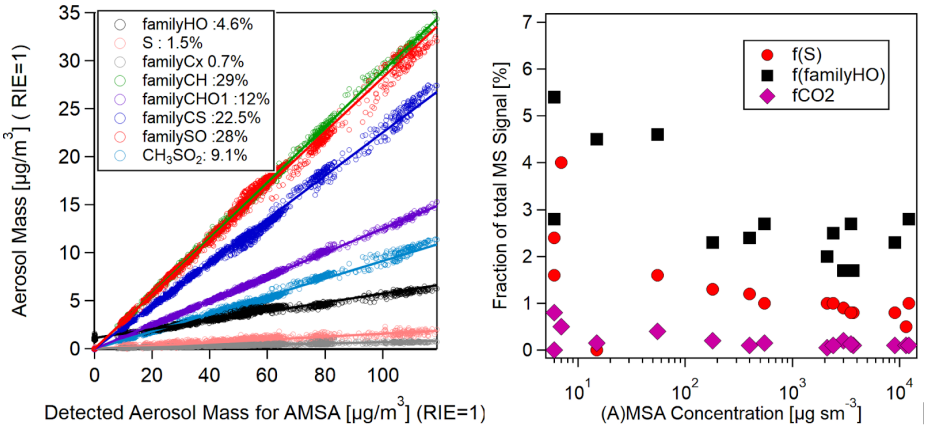

Figure S15. (left) Determination of the fractional ion contributions (summed up into chemical families) in the AMS (including water, sulfur and CO_2) of MSA for an AMSA calibration at intermediate concentrations ([MSA]~10-50 µg sm^{-3}, as determined by SMPS measurements). (right) Contributions of S^+, CO_2^+ and water ions to the total AMS signal of MSA for all the ATom calibrations (calibrations were done with both AMSA and MSA, but only MSA was quantified).

S5.3. Quantification of the Relative Ionization Efficiency of MSA (RIE_{MSA})

RIE_{MSA} was derived from two different approaches:

1. Relative to the ammonium *RIE* (RIE_{NH4}) after back-to-back calibrations with ammonium nitrate ("ammonium balance method") analogous to the most-commonly used method for the determination of sulfate and chloride *RIE* (Schroder et al., 2018). This assumes that, as in the case of sulfate, the analyzed particles are fully neutralized when introduced into the AMS. In the case of another ammonium salt of an organic acid, ammonium oxalate, some studies have suggested partial evaporation of ammonia prior to analysis (Jimenez et al., 2016). Thermodynamic calculations suggest that this is due to the $H(COOH)_2^+$ being a weak acid (pK_a=4.19, Lide 2008), leading to some formation of molecular oxalic acid and subsequent partitioning of NH_3 to the gas phase, but not of oxalic acid given its much lower vapor pressure. Given that MSA is a strong acid (pKa=-1.96 (Guthrie, 1978)), this is not expected for AMSA, and in fact no difference in these experiments was observed when the AMSA solution was saturated with NH_4OH (vs just neutralized). This method is independent of AMS transmission,

collection efficiency and possible evaporation of the semivolatile AMSA prior to AMS sampling.

2. Determining the value of of RIE_{MSA} that is needed for the AMS to match the aerosol mass calculated from simultaneous measurements by the SMPS/CPC ("mass closure method") (Willis et al., 2016; Huang et al., 2017). This requires generating a monodisperse aerosol with little to no doubly charged particles and knowledge of both the density and collection efficiency of AMSA. In addition, for a semivolatile species such as MSA (p_{vap}=6*10^{-4} Torr at 20^{o} C, Tang and Munkelwitz, 1991) there could be differences due to potential evaporation in the CPC and AMS lines, which would complicate the comparison. Both monodispersity and effective density (which was sometimes lower than the bulk density of 1.48 g cm^{-3}, Lide et al., 2008) were confirmed with particle time-of-flight measurements (PToF, de Carlo et al, 2004). Single particle measurements (described in detail below) confirmed that *CE* was close to 1 and that evaporation was a minor concern. Therefore a *CE* of 1 was used. Assuming negligible evaporation/wall deposition in the lines both methods should yield similar results.

Figure S16 shows data for 2 AMSA calibrations at low concentrations taken one year apart where the RIE_{MSA} for both methods agreed within 5% and the corresponding PToF measurements. We hence report RIE_{MSA} = 1.70 ± 0.08 based on the more accurate ammonium balance method, while using the difference with the mass closure method as a conservative uncertainty estimate. This RIE_{MSA} was used for the all four ATom deployments, given the small change (<5%) in the other RIEs of the instrument over these campaigns.

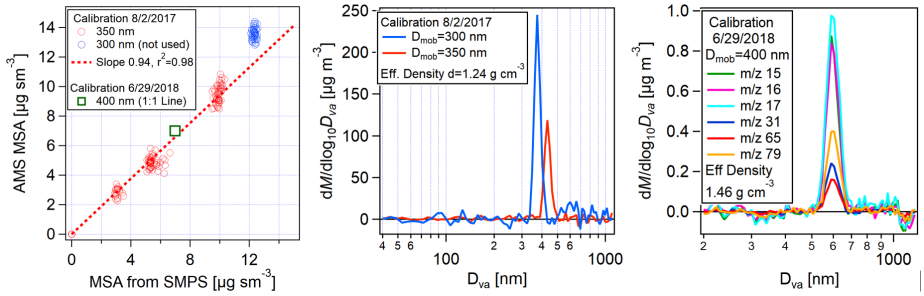

Figure S16. (left) Regression of the AMS response for MSA with the calculated SPMS mass of the test aerosol for two different calibrations of the CU AMS instrument using $NH_4SO_3CH_3$ (AMSA) taken one year apart. AMS response was calculated using f(CH_3SO_2) from the calibration and an RIE_{MSA} derived from the ion balance (1.7 on 8/2/2017, 1.72 on 6/29/2018); the SPMS mass was calculated using the density determined from the D_{va}/D_{geo} ratio for each calibration (DeCarlo et al., 2004). (middle) Particle time-of-flight size distribution of the test aerosol for the 8/2/2017 calibration, used to determine the density and confirm monodispersity. (right) AMS PToF-mode size distribution for the 6/29/2018 calibration, showing the same m/z ions that were used in the analysis of the single particle experiments (Figure S19).

S5.4. Robustness of the MSA Mass Spectral Pattern in the AMS

Zorn et al. (2008) reported that the fragmentation pattern of MSA was highly dependent on vaporizer temperature. Special care was taken during ATom to keep the vaporizer temperature constant at ~600^{o}C by keeping the vaporizer current constant and periodically calibrating the instrument response with $NaNO_3$ (Hu et al., 2017). The MSA fragmentation pattern at low concentrations (comparable and larger than ambient concentrations) was observed to be very stable over the course of the four ATom deployments.

However, significant changes in $f(CH_3SO_2)$ were observed when higher calibration particle concentrations were used (Figure S17a). Figure S17b shows the variability in time of the main ion families that contribute to the MSA signal for a typical AMSA calibration at higher concentrations. While NH_4 shows an very fast and stable response, for MSA a fraction of the signal shows a slower time response after each background cycle (which some ion groups showing this trend stronger than others; this will be discussed in more detail in Section S5.7). The rate of equilibration is concentration dependent, hence at higher concentrations not only do the relative ion ratios change, but also the overall signal recorded by the AMS, resulting in larger apparent values of RIE_{MSA} at higher concentrations. This effect only appears to be important at very high concentrations of 100s to 1000s of μg m^{-3}, but we document it here since calibrations are often performed at such higher concentrations. Based on these results, we recommend calibrating at concentrations similar to ambient levels.

It is important to note that the magnitude of this effect is very dependent on the acquisition cycle of the AMS: For the CU-AMS, which operates in "fast mode" (6 s closed, 46 s open, Schroder et al., 2018), the time available for MSA reaching some of sort of equilibrium in the ionizer is substantially longer than in the standard AMS acquisition sequence (4 s closed, 6 s open). Hence RIE_{MSA} taken at similar concentrations in the standard AMS acquisition mode may be lower than the values that we reported above. However, it is also possible that the slower response if more important in the CU AMS instrument, as the presence of a cryopump surface cooled to 90 K around the ionizer region will lower the equilibrium temperature of the ionizer, compared to standard AMS instruments. Since at least some of the slow response may be due to particles or gases deposited on the ionizer surfaces, this lower temperature could play a role in the observed slow response.

We are unaware of previous reports on this concentration dependent change in fragmentation pattern, although most of them calibrated over a small range of concentrations (Willis et al., 2016, Huang et al., 2017). It is worth noting that Huang et al. (2015) reports a value of 0.10±0.02 for $f(CH_3SO_2)$, and their error bar does suggest variability on a similar scale as we found for unspecified reasons.

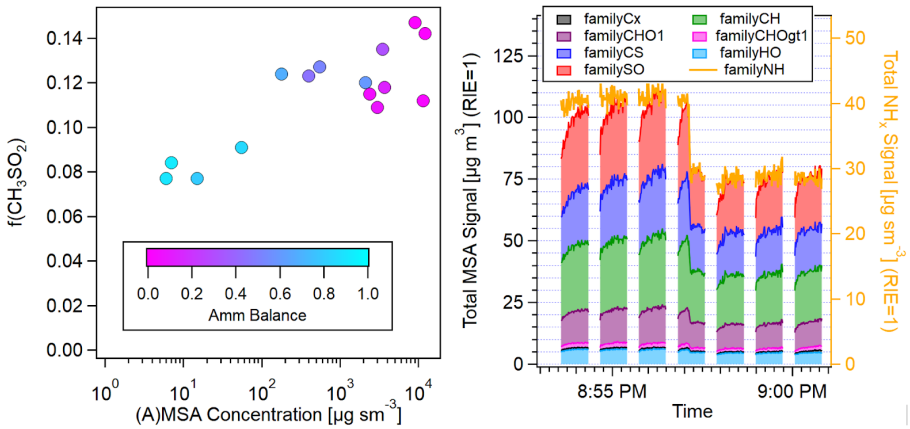

Figure S17. (left) Summary of all the marker ratios found in ATom calibrations as a function of MSA concentration, both using AMSA (excluding ammonium) and MSA. (right) Timeseries of the total ion signal (classified into AMS families) of MSA and NH_4 (both at RIE of 1) for a an AMSA calibration with 50 µg sm-3 of MSA, showing that for each acquisition cycle for some subset of the ions (mostly SO_x and CS) there is an equilibration time which depends on concentration and that is not observed for NH_4. This results in a time-dependent response that is especially pronounced at higher concentrations and hence affects both $f(CH_3SO_2)$ and RIE_{MSA} (relative to RIE_{NH4}).

Since all the calibration with acidic MSA in our study were done at high concentrations, this could result in a potential uncertainty in the AMS fragmentation pattern of MSA (vs AMSA) and a potential bias in quantifying MSA in some of the highly acidic environments found in ATom. In order to further address this potential source of uncertainty for the ambient data, the data from the ATom-1 deployment was analyzed by positive matrix factorization (PMF) (Paatero 1994, Ulbrich et al., 2009) to extract a (calibration independent) MSA mass spectral profile. This was done by combining the organic and sulfate ions from the full mission at 1 min resolution (for improved fitting accuracy and detection limits, see Schroder et al., 2018) and performing PMF analysis with the PMF Evaluation Panel (PET) v3.01 (Ulbrich et al., 2009). Best results were achieved after downweighting the SO_x ions by 10x to make their weight in the weighted residual comparable to those of the larger organic ions. Figure S18a and b compares the spectra of the MSA factor obtained with the MS Spectra from the low concentration AMSA calibrations, showing excellent agreement for all ions except CH_3^+ (which is less specific than most other ions in the spectrum, since it can arise from a myriad of other OA species). Importantly, $f(CH_3SO_2)$ in both cases is nearly identical (7.9% for the PMF factor vs 7.8% for the calibrations), confirming the validity of the low-concentration calibrations and also their applicability for ATom-1 (where no in-field calibrations for MSA were conducted).

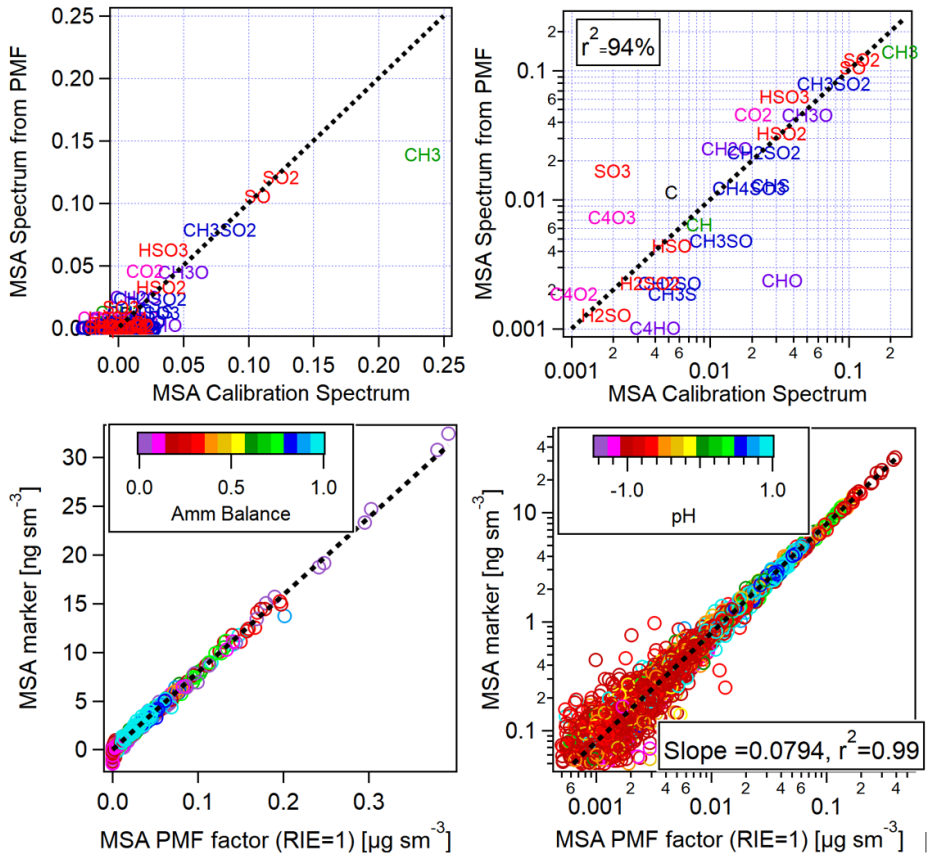

Figure S18. (top) Comparison of the MSA Factor extracted from PMF analysis of the full sulfate+OA dataset during ATom-1 with the calibration spectrum of $NH_4SO_3CH_3$ (AMSA) taken at low concentrations, (a) on a linear scale and (b) on a logarithmic scale . (bottom) Scatter plot of the total signal for the $CH_3SO_2^+$ ion for the ATom-1 campaign vs. the MSA PMF Factor concentration (c) on a linear scale and (d) on a logarithmic scale as a function of acidity. The very highly correlated behavior independent of acidity suggests that for ambient data f(CH_3SO_2) does not significantly change as a function of acidity.

However, the mass spectrum of the PMF Factor is a campaign average that is primarily weighted towards the often not-so-acidic marine boundary layer passes where the factor concentration was highest. To examine if MSA found under acidic conditions (mostly in the free troposphere) could have a different fragmentation pattern, it is instructive to look at the correlation of the $CH_3SO_2^+$ ion with the PMF factor. If pure MSA had a different *f*(CH_3SO_2) than AMSA, this would lead to a deviation from the 7.9% slope line prescribed by PMF. However, despite the very high acidities that were

sometimes encountered while sampling MSA (pH<0), no significant deviation from linear behavior is observed over several orders of magnitude (Figure S18c and d). We hence conclude that there is no evidence for $f(CH_3SO_2)$ being a function of MSA acidity, and that even if the relative fractions of other ions were to change slightly as a function of acidity, quantification of MSA based on Eq. S1 should not be affected.

Hence, with a value of $f(CH_3SO_2)$ of 0.08±0.003 (average of low concentration calibrations and PMF factor), the combined inverse scaling factor of MSA relative to the CH_3SO_2 ion for ATom is 0.136±0.011, i.e. a combined multiplicative factor of 7.35 to translate $[CH_3SO_2^+]$ (in nitrate-equivalent concentration units; Jimenez et al., 2003) to [MSA] per Eq. S1 (referred in the following as the scaling factor, $S(CH_3SO_2)$).

$$S(CH_3SO_2) = \frac{1}{RIE(MSA) * f(CH_3SO_2)} \quad (Eq.S2)$$

S5.5 Comparison with previous studies

Table S4 summarizes all the studies where to the best of our knowledge both the marker fraction and the RIE for total MSA signal have been reported. It should be noted that only Willis et al. (2016) and Huang et al. (2017) directly measured RIE_{MSA}. In both cases, the mass closure method was used with reportedly pure, acidic MSA (although some neutralization was observed prior to analysis). While the linearity of their calibrations strongly suggests that doubly charged particles were not sampled, as noted above the shorter acquisition sequence might have resulted in a smaller RIE_{MSA} depending on the fraction of slower response in their instruments. In addition, evaporation and neutralization would still be a concern that could possibly lead to a potentially reduced RIE_{MSA}. Phinney et al. (2006) used RIE_{SO4}, while Schmale et al. (2013) used RIE_{OA} (consistent with their determination of MSA by PMF of OA, which also likely explains the low value of $f(CH_3SO_2)$). Both Huang et al. (2015) and Zorn et al (2008) used an averaged RIE of OA and sulfate (in Zorn's case an arithmetic average, in Huang's case a mass-weighted one).

While all reported values for RIE_{MSA} are lower than the one determined in this work, part of this difference may be due to instrument-to-instrument variability. It is worth noting that RIE_{SO4} in the CU AMS (determined by in-situ calibrations) is often significantly higher than the default RIE_{SO4} used by the other groups (1.5-1.7 vs 1.15-1.2) (Canagaratna et al., 2007), which might be due to a higher general sensitivity in this instrument for larger ions as well as the longer acquisition cycle compared to a regular AMS. However, this may not imply that RIE_{MSA} and RIE_{SO4} should be comparable for a given AMS. Sulfate mass in the AMS (based on the default fragmentation table, Allan et al., 2004) includes a large contribution of water (31%) and sulfur (7%) ions, significantly larger than what was found in this study for MSA (5% total).

Given the high variability in the determinations of $f(CH_3SO_2)$ it would be hence preferable to compare the scaling factor $S(CH_3SO_2)$ used to actually relate CH_3SO_2 to MSA (Table S4), but given that, as already discussed, most studies did not directly measure RIE_{MSA}, the variability of this parameter is also quite large. The fact that even in the cases where both RIE_{MSA} and $f(CH_3SO_2)$ were determined (Willis et al., 2016; Huang et al., 2017 and this work) the variability is $S(CH_3SO_2)$ is over a factor of 3 emphasizes

the instrumental variability and the need for careful calibrations of both RIE_{MSA} and $f(CH_3SO_2)$ in studies where MSA from AMS data is reported.

Table S4: RIE_{MSA}, as well as the relative abundance of the marker ion $f(CH_3SO_2)$ in previously reported calibrations of AMS response to MSA. Also listed is the effective scaling factor that results from these two quantities, $S(CH_3SO_2)$.

$f(CH_3SO_2)$, %	RIE_{MSA}	$S(CH_3SO_2)$	Reference
6.9	1.15	12.6	Phinney et al, 2006 (Q-AMS)
9	1.3	8.6	Zorn et al, 2008
4	1.4	17.9	Schmale et al, 2013 (PMF)
9.7	1.3	8	Huang et al, 2015
12.4	1.33	6.1	Willis et al, 2016
4	1.27	19.7	Huang et al, 2017
7.9	1.70 ± 0.08	7.4	This work

S5.6 Details of the Single Particle Calibrations, including CE of pure MSA

Previous AMS studies on MSA have often assumed that due to acidity and phase, MSA should have a collection efficiency (CE, Middlebrook et al, 2012) of 1 (i.e. that pure particles do not bounce off the vaporizer), but this has not been confirmed previously. It is also not clear if the same applies for the semivolatile, yet non-acidic and solid at room temperature AMSA. Hence the CE of AMSA was determined using the single particle method (Canagaratna et al, 2007) using the Event Trigger acquisition mode of the AMS DAQ software.

Both monodisperse 400 nm ammonium nitrate (AN in the following, Aldrich, >99%) and AMSA particles were introduced into the AMS and detected by triggering on *m/z* 30 and 46 (NO^+ and NO_2^+) for AN and *m/z* 15 and 79 for AMSA (CH_3^++NH^+ and $CH_3SO_2^+$) (Figure S19). For the fast evaporating AN, we found that the AMS detected 89% of the particles compared to a collocated CPC, consistent with the inlet transmission close to 100% efficient observed for this instrument (Schroder et al, 2018). For the AMSA particles that have a similar effective density (1.48 g cm^{-3} for AMSA vs 1.42 g cm^{-3} for AN) and hence should be transmitted at the same rate, we found a ratio of AMS single particle detection to CPC of 93%, hence confirming that for AMSA, CE~1.

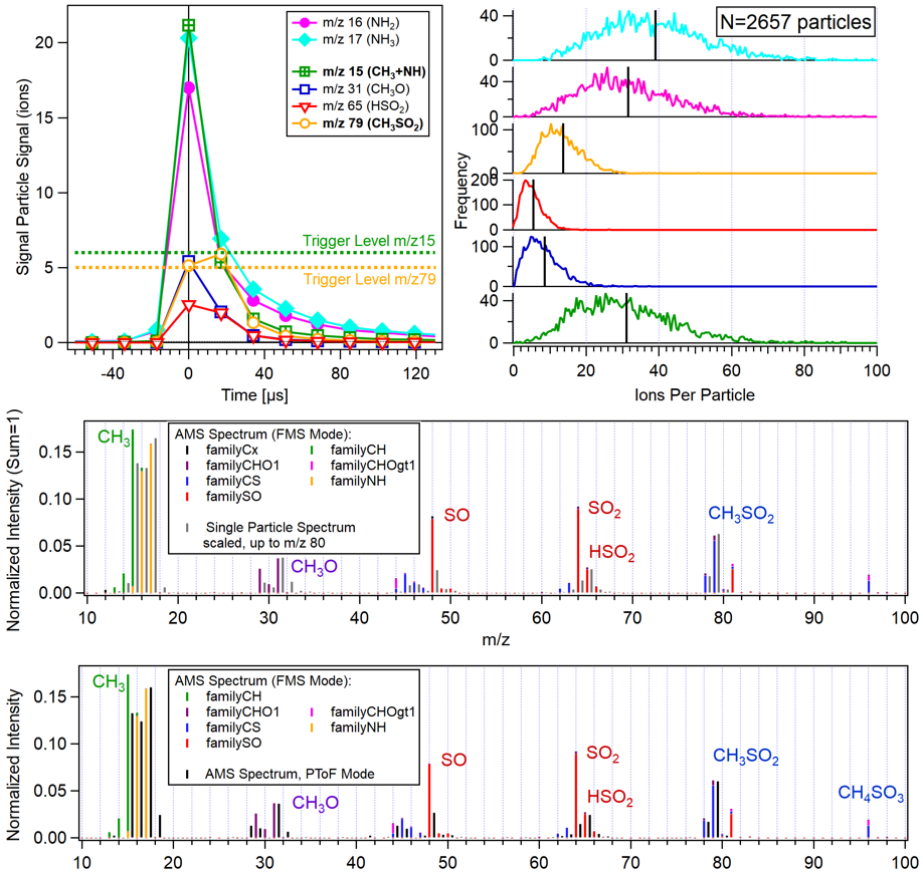

Figure S19. (top left) Average timetraces of the single particle signals at several mass to charge ratios for both the cation (NH_4) and anion (CH_3SO_3) recorded for 400 nm $NH_4CH_3SO_3$ particles being sampled into the AMS in ET mode. To trigger the single particle acquisition, either of the UMR m/z in bold (m/z 15 and 79) had to cross the prescribe threshold (dotted lines). (Right) Histograms of the total ions per particle recorded for each UMR m/z mass (2657 valid events). Black lines show the average values used in the IE calculations. (middle) Comparison of the immediate vaporization MS observed in the single particle experiments with the calibration spectrum taken in regular acquisition mode (FMS). (bottom) Comparison of the immediate vaporization MS observed in PToF mode with the calibration spectrum taken in FMS mode.

Despite the fast vaporization and detection of (nearly) every single particle, the MS spectrum recorded in single particle mode (Figure S19, 200 µs integration time) and ePToF mode (14 ms integration time) show significant differences when compared to the regular (ambient) MS mode (FMS, 1 s integration time, Kimmel et al, 2011). Most of the

SO_x^+ ions (and CH_3^+) have lower relative intensities at the shorter integration times, suggesting that these are released on longer timescales from the vaporizer. This different response times and hence, equilibration times for different components of the spectrum are likely also responsible for the spectral changes observed when varying the concentration of MSA over large ranges (Figure S16). For ambient data acquired during the ATom mission, this is clearly not a concern, as shown by the PMF analysis, but this effect could impact laboratory studies involving MSA and AMS detection via the marker method.

S5.7 ATom Data status

As detailed in the headers of the currently posted data (Wofsy et al., 2018), currently some fraction of the MSA mass is attributed to sulfate and some to OA. While these errors are typically small, future revisions will incorporate a correction to those species based on the quantification of MSA detailed above.

References

Allan, J. D., Delia, A. E., Coe, H., Bower, K. N., Alfarra, M. R. R., Jimenez, J. L., Middlebrook, A. M., Drewnick, F., Onasch, T. B., Canagaratna, M. R., Jayne, J. T. and Worsnop, D. R.: A generalised method for the extraction of chemically resolved mass spectra from Aerodyne aerosol mass spectrometer data, J. Aerosol Sci., 35(7), 909–922, doi:10.1016/j.jaerosci.2004.02.007, 2004.

Canagaratna, M. R., Jayne, J. T. J. T., Jimenez, J. L., Allan, J. D., Alfarra, M. R., Zhang, Q. Q., Onasch, T. B., Drewnick, F., Coe, H., Middlebrook, A. M., Delia, A., Williams, L. R., Trimborn, A. M., Northway, M. J., DeCarlo, P. F., Kolb, C. E., Davidovits, P. and Worsnop, D. R.: Chemical and microphysical characterization of ambient aerosols with the Aerodyne Aerosol Mass Spectrometer, Mass Spectrom. Rev., 26(2), 185–222, doi:10.1002/mas, 2007

Peter F. DeCarlo, Jay G. Slowik, Douglas R. Worsnop, Paul Davidovits & Jose L. Jimenez (2004) Particle Morphology and Density Characterization by Combined Mobility and Aerodynamic Diameter Measurements. Part 1: Theory, Aerosol Science and Technology, 38:12, 1185-1205, DOI: 10.1080/027868290903907

Guthrie, J.P.:Hydrolysis of esters of oxy acids: pKa values for strong acids; Brønsted relationship for attack of water at methyl; free energies of hydrolysis of esters of oxy acids; and a linear relationship between free energy of hydrolysis and pKa holding over a range of 20 pK units, Can. J. Chem., 56:2342-2354, 1978

Hu, W., Campuzano-Jost, P., Day, D. A., Croteau, P., Canagaratna, M. R., Jayne, J. T., Worsnop, D. R. and Jimenez, J. L.: Evaluation of the new capture vapourizer for aerosol mass spectrometers (AMS) through laboratory studies of inorganic species, Atmos. Meas. Tech., 10(6), 2897–2921, doi:10.5194/amt-10-2897-2017, 2017.

Huang, D. D., Li, Y. J., Lee, B.P and Chan, C. K.: Analysis of Organic Sulfur Compounds in Atmospheric Aerosols at the HKUST Supersite in Hong Kong Using HR-ToF-AMS. Environ. Sci. Tech. 49 (6), 3672-3679 2015

Huang, S., Poulain, L., van Pinxteren, D., van Pinxteren, M., Wu, Z., Herrmann, H. and Wiedensohler, A.: Latitudinal and Seasonal Distribution of Particulate MSA over the Atlantic using a Validated Quantification Method with HR-ToF-AMS, Environ. Sci. Technol., 51(1), 418–426, doi:10.1021/acs.est.6b03186, 2017.

Jimenez, J. L., Canagaratna, M. R., Drewnick, F., Allan, J. D., Alfarra, M. R., Middlebrook, A. M., Slowik, J. G., Zhang, Q., Coe, H., Jayne, J. T., Worsnop, D. R., Rami Alfarra, M., Middlebrook, A. M., Slowik, J. G., Zhang, Q., Coe, H., Jayne, J. T. and Worsnop, D. R.: Comment on "The effects of molecular weight and thermal decomposition on the sensitivity of a thermal desorption aerosol mass spectrometer," Aerosol Sci. Technol., 50(9), i–xv, doi:10.1080/02786826.2016.1205728, 2016.

Kimmel, J. R., Farmer, D. K., Cubison, M. J., Sueper, D., Tanner, C., Nemitz, E., Worsnop, D. R., Gonin, M. and Jimenez, J. L.: Real-time aerosol mass spectrometry with millisecond resolution, Int. J. Mass Spectrom., 303(1), 15–26, doi:10.1016/j.ijms.2010.12.004, 2011.

Lide, D.R. CRC Handbook of Chemistry and Physics 88TH Edition 2007-2008. CRC Press, Taylor & Francis, Boca Raton, FL 2007, p. 3-326

Middlebrook, A. M., Bahreini, R., Jimenez, J. L. and Canagaratna, M. R.: Evaluation of Composition-Dependent Collection Efficiencies for the Aerodyne Aerosol Mass Spectrometer using Field Data, Aerosol Sci. Technol., 46(3), 258–271, doi:10.1080/02786826.2011.620041, 2012.

Paatero, P. and Tapper, U.: Positive Matrix Factorization - A Nonnegative Factor Model With Optimal Utilization of Error-Estimates of Data Values, Environmetrics, 5(2), 111–126, 1994.

Phinney, L., Richard Leaitch, W., Lohmann, U., Boudries, H., Worsnop, D. R., Jayne, J. T., Toom-Sauntry, D., Wadleigh, M., Sharma, S., Shantz, N., Leaitch, W. R., Lohmann, U., Boudries, H., Worsnop, D. R., Jayne, J. T., Toom-Sauntry, D., Wadleigh, M., Sharma, S., Shantz, N., Richard Leaitch, W., Lohmann, U., Boudries, H., Worsnop, D. R., Jayne, J. T., Toom-Sauntry, D., Wadleigh, M., Sharma, S., Shantz, N., Leaitch, W. R., Lohmann, U., Boudries, H., Worsnop, D. R., Jayne, J. T., Toom-Sauntry, D., Wadleigh, M., Sharma, S. and Shantz, N.: Characterization of the aerosol over the sub-arctic north east Pacific Ocean, Deep. Res. II-Topical Stud. Oceanogr., 53(20–22), 2410–2433, doi:10.1016/j.dsr2.2006.05.044|ISSN 0967-0645, 2006.
Schmale, J., Schneider, J., Nemitz, E., Tang, Y. S., Dragosits, U., Blackall, T. D., Trathan, P. N., Phillips, G. J., Sutton, M. and Braban, C. F.: Sub-Antarctic marine aerosol: dominant contributions from biogenic sources, Atmos. Chem. Phys., 13(17), 8669–8694, doi:10.5194/acp-13-8669-2013, 2013.

Schroder, J. C., Campuzano-Jost, P., Day, D. A., Shah, V., Larson, K., Sommers, J. M., Sullivan, A. P. Campos, T. Reeves, J. M. Hills, A., Hornbrook, R. S., Blake, N. J.,

Scheuer, E., Guo, H., Fibiger, D. L. McDuffie, E. E., Hayes, P. L., Weber, R. J., Dibb, J. E. Apel, E. C., Jaeglé, L. Brown, S. S. Thornton, J. A. and Jimenez, J. L. Sources and secondary production of organic aerosols in the northeastern United States during WINTER. Journal of Geophysical Research: Atmospheres, 123, 7771–7796. 2018

Tang, I. N. and Munkelwitz, H. R.: Determination of Vapor Pressure from Droplet Evaporation Kinetics, Journal of Colloid and Interface Science, 141, (1), 1991

Ulbrich, I. M., Canagaratna, M. R., Zhang, Q., Worsnop, D. R. and Jimenez, J. L.: Interpretation of organic components from Positive Matrix Factorization of aerosol mass spectrometric data, Atmos. Chem. Phys., 9(9), 2891–2918, doi:10.5194/acp-9-2891-2009, 2009.

Willis, M. D., Burkart, J., Thomas, J. L., Köllner, F., Schneider, J., Bozem, H., Hoor, P. M., Aliabadi, A. A., Schulz, H., Herber, A. B., Leaitch, W. R. and Abbatt, J. P. D.: Growth of nucleation mode particles in the summertime Arctic: a case study, Atmos. Chem. Phys., 16(12), 7663–7679, doi:10.5194/acp-16-7663-2016, 2016.

Wofsy, S.C., S. Afshar, H.M. Allen, E. Apel, E.C. Asher, B. Barletta, J. Bent, H. Bian, B.C. Biggs, D.R. Blake, N. Blake, I. Bourgeois, C.A. Brock, W.H. Brune, J.W. Budney, T.P. Bui, A. Butler, P. Campuzano-Jost, C.S. Chang, M. Chin, R. Commane, G. Correa, J.D. Crounse, P. D. Cullis, B.C. Daube, D.A. Day, J.M. Dean-Day, J.E. Dibb, J.P. DiGangi, G.S. Diskin, M. Dollner, J.W. Elkins, F. Erdesz, A.M. Fiore, C.M. Flynn, K. Froyd, D.W. Gesler, S.R. Hall, T.F. Hanisco, R.A. Hannun, A.J. Hills, E.J. Hintsa, A. Hoffman, R.S. Hornbrook, L.G. Huey, S. Hughes, J.L. Jimenez, B.J. Johnson, J.M. Katich, R. Keeling, M.J. Kim, A. Kupc, L.R. Lait, J.-F. Lamarque, J. Liu, K. McKain, R.J. Mclaughlin, S. Meinardi, D.O. Miller, S.A. Montzka, F.L. Moore, E.J. Morgan, D.M. Murphy, L.T. Murray, B.A. Nault, J.A. Neuman, P.A. Newman, J.M. Nicely, X. Pan, W. Paplawsky, J. Peischl, M.J. Prather, D.J. Price, E. Ray, J.M. Reeves, M. Richardson, A.W. Rollins, K.H. Rosenlof, T.B. Ryerson, E. Scheuer, G.P. Schill, J.C. Schroder, J.P. Schwarz, J.M. St.Clair, S.D. Steenrod, B.B. Stephens, S.A. Strode, C. Sweeney, D. Tanner, A.P. Teng, A.B. Thames, C.R. Thompson, K. Ullmann, P.R. Veres, N. Vieznor, N.L. Wagner, A. Watt, R. Weber, B. Weinzierl, P. Wennberg, C.J. Williamson, J.C. Wilson, G.M. Wolfe, C.T. Woods, and L.H. Zeng. 2018. ATom: Merged Atmospheric Chemistry, Trace Gases, and Aerosols. ORNL DAAC, Oak Ridge, Tennessee, USA. https://doi.org/10.3334/ORNLDAAC/1581

Zorn, S. R., Drewnick, F., Schott, M., Hoffmann, T. and Borrmann, S.: Characterization of the South Atlantic marine boundary layer aerosol using an aerodyne aerosol mass spectrometer, Atmos. Chem. Phys., 8(16), 4711–4728, doi:10.5194/acp-8-4711-2008, 2008.